CATACLYSMIC VARIABLES:

THEIR X-RAY TIMING AND SPECTRAL CHARACTERISTICS

ANIRBAN DUTTA

THESIS SUBMITTED FOR THE DEGREE OF

DOCTOR OF PHILOSOPHY

THESIS SUPERVISOR:

PROF. VIKRAM RANA

RAMAN RESEARCH INSTITUTE
BENGALURU 560080, KARNATAKA, INDIA

JAWAHARLAL NEHRU UNIVERSITY
NEW DELHI 110067, DELHI, INDIA

Submitted: January, 2023

Declaration

I, *Anirban Dutta* (Enrolment Number: RRI/18/001), declare that the work reported in this thesis titled '*Cataclysmic Variables: Their X-ray Timing And Spectral Characteristics*', is entirely original. This thesis is composed independently by me at *Raman Research Institute (RRI)* under the supervision of *Prof. Vikram Rana* and is the result of my own work unless otherwise stated. I further declare that the subject matter presented in this thesis has not previously formed the basis for the award of any degree, diploma, membership, associateship, fellowship or any other similar title of any university or institution. I also declare, this thesis has been checked through the plagiarism software Drillbit.

_____   _____

Signature of Supervisor   Signature of Candidate

Prof. Vikram Rana   **Anirban Dutta**

Professor, RRI   Research Fellow, RRI

Astronomy & Astrophysics Group

Raman Research Institute (RRI)

Bengaluru 560080, Karnataka IN

Date:

Place:

Certificate

This is to certify that the work contained in the thesis titled '***Cataclysmic Variables: Their X-ray Timing And Spectral Characteristics***', submitted by *Anirban Dutta* (Enrolment Number: RRI/18/001) to the Jawaharlal Nehru University for the award of the degree of **Doctor of Philosophy (Ph.D.)** in Physical Sciences, is the bonafide record of orginal research work carried out by the candidate from July 2018 — January 2024, under my guidance and supervision at Raman Research Institute (RRI), Bengaluru, India. The results embodied in the thesis have not been submitted to any other University or Institute for the award of any degree or diploma.

_____   _____

Signature of Director   Signature of Supervisor

Prof. Tarun Souradeep   **Prof. Vikram Rana**

Director & Professor, RRI   Professor, RRI

Astronomy & Astrophysics Group

Raman Research Institute (RRI)

Bengaluru 560080, Karnataka IN

Date:

Place:

Acknowledgements

I express my acknowledgement:

— To my supervisor, for the academic and professional mentoring during my doctoral studies and research.

— To my parents, for all the guidance and support in my life.

— To my collaborators, for the engaging and insightful discussions.

— To the faculty members of my institute, for providing the vibrant academic atmosphere, and the other staff members, for offering excellent research facilities, including the library, computer, administrative, and estate sections.

— To my friends and colleagues, corridor-apart or separated by oceans, intersected my timeline briefly or extensively, for all the academic, professional, philosophical, and personal exchanges that enriched me through the peaks and valleys of this phase in my journey.

— To the Universe, for making me a part of it and letting me wonder about it!

Contents

4 Study of complex absorption and reflection in a unique intermediate polar Paloma   **47**

5 A broadband X-ray study of the dwarf nova SS Cyg during quiescence and outburst   **71**

6 X-ray properties of asynchronous polars V1432 Aql and BY Cam   **91**

Introduction

The Cataclysmic Variables (CVs) are semi-detached accreting binary systems where mass transfer takes place from a donor, typically a late type main sequence star which is filling its Roche lobe, to an accretor, a white dwarf(WD) (Hellier C., 2001, Cataclysmic Variable Stars: How and Why They Vary, Springer Praxis; Warner B., 1995, Cataclysmic Variable Stars, Cambridge Univ. Press). Depending on the strength of the magnetic field of the white dwarf, we classify them in magnetic ($\sim 10^5 - 10^8$G) and non-magnetic CVs ($\lesssim 10^5$G). The accreting material directly follows the magnetic field lines from Lagrangian point and fall on to WD poles for the WD with strongest ($\sim 10^6 - 10^8$G) magnetic fields, the polars. In case of Intermediate polars (IPs), with relatively weaker magnetic field ($\sim 10^5 - 10^6$G) of WD, generally a partial accretion disk is first formed around WD and at the final stage of accretion, the material follows the magnetic field lines. Polars generally show perfect synchronicity between the orbital period of the binary system and the spin period of the WD, whereas for IPs, generally the asynchronosity is much higher ($\gtrsim 90\%$). For non-magentic CVs, the accretion will occur via the accretion disk. The process of accretion is a powerful source of energy production in CVs, emitting radiation ranging from Infrared to X-rays. Study of X-ray emissions from CVs, mainly originating from post-shock region of accretion column over WD pole or the boundary layer between WD and accretion disc (Mukai K., 2017, PASP, 129, 976) unravel interesting accretion and geometric properties of CVs. In our research we used data obtained from the multiple X-ray observatories to find out exciting features of CVs like size and mass of the WD, orbital geometry, the system periods, nature of the accretion process, structure of the accretion disc and accretion column. We have studied the X-ray temporal and spectral properties of the sources to interpret different physical phenomena and construct a comprehensive picture about the accretion processes in these sources.

Study of the asynchronous polar CD Ind

CD Ind belongs to the rare class of magnetic CVs, called asynchronous polars in which the orbital period of the system is slightly asynchronous ($\sim 1-2\%$) with the spin period of the WD. We have studied this source using the simultaneous broadband X-ray data from XMM-Newton and NuSTAR. The spin-folded light curve in the soft 0.3–3.0 keV band shows a single broad hump-like structure superimposed with occasional narrow dips, indicating a single-pole accretion model with a complex intrinsic absorber. We did not notice strong modulation in the folded light curve above 3 keV revealing that emission from the corresponding zone of the post-shock region (PSR) remains in view throughout

the spin phase. We modelled the broad-band spectrum with a three-component absorbed plasma emission model and an absorbed isobaric cooling flow model, both of which fit the data well with similar statistical significance. The presence of a partial covering absorber is evident in the spectra with equivalent column density $7 \times 10^{22} cm^{-2}$ and a covering fraction of 25 per cent. Strong ionized oxygen Kα line emission is detected in the spectra. We notice spectral variability for almost one third duration of complete spin cycle, when there is a considerable increase in the column density of the overall absorber (from $1 \times 10^{20} cm^{-2}$ to $9 \times 10^{20} cm^{-2}$). We required at least three plasma temperatures to describe the multitemperature nature of the PSR. Using the braodband spectra, we directly measured the shock temperature of $43.3^{+3.8}_{-3.4}$ keV, corresponding to a white dwarf mass of $0.87^{+0.04}_{-0.03} M_\odot$. The iron K$\alpha$ line complex show strong He-like and weak neutral fluorescence lines. We could not unambiguously detect the presence of Compton reflection in the spectra, which is probably very small and signifies a tall shock height.

We also discuss results from a few other interesting CV sources like V1432 Aql, BY Cam and etc., and their timing and spectral properties by analysing their the X-ray data. Particularly for V1432 Aql and BY Cam which also fall under the rare category of asynchronous polars, we detected strong Compton reflection signature in their spectra, revealing the properties about the X-ray emission region.

Complex absorption and Compton reflection in intermediate polar Paloma

We present the broadband (0.3–40.0 keV) X-ray study of a unique intermediate polar Paloma using simultaneous data from XMM-Newton and NuSTAR observatories. The X-ray power spectra show strong modulations over orbital period compared to spin period. The orbit-folded light curves show a single broad hump-like structure with strong dips for soft to medium X-rays (0.3–10.0 keV). We noticed two energy-dependent dips in the orbit folded light curve arise as a result of a complex intrinsic absorber, strong enough to have an effect around 15 keV. The absorber could potentially be contributed from accretion curtain/accretion stream and absorbing material produced by stream-disk/stream–magnetosphere interactions. A significant variation of the absorber with orbital phase is present, with maximum absorption during almost 12% of the orbital cycle. The absorber requires more than one partial covering absorber component, specifying the necessity to use distribution of column densities for spectral modeling of the source. The isobaric cooling flow component is utilized to model the emission from the multitemperature post-shock region, giving a shock temperature of $31.7^{+3.3}_{-3.5}$ keV, which corresponds to a white dwarf mass of $0.74^{+0.04}_{-0.05} M_\odot$. We have used both the neutral absorber and warm absorber models, which statistically give a similarly good fit, but with different physical implications. Among the Fe Kα line complex, the neutral line is the weakest. We probed the Compton reflection and found a minimal statistical contribution

in the spectral fitting, suggesting the presence of weak reflection in Paloma.

Study of dwarf novae SS Cyg during quiescence and outburst

SS Cyg is one of the brightest dwarf novae, a type of non-magnetic CV, that undergoes outbursts every 40-50 days and lasts 10-12 days. The outburst is associated with thermal-viscous instability in the accretion disk, which changes the geometry and properties of the X-ray emitting boundary layer (BL). Using simultaneous broadband X-ray data (0.3-50 keV) from XMM-Newton and NuSTAR observatories, we discuss a comparative study on how the nature of the X-ray emitting plasma changes during the quiescent and outburst phases of SS Cyg. We notice significantly harder X-ray spectra during quiescence ($\sim$ 23keV) compared to outburst ($\sim$ 8keV) and copious soft X-ray emission in the form of blackbody (temperature $\sim$ 28eV) during outburst, which highlight the changes in the BL's opacity and mass accretion rate (nearly 30 times enhanced mass accretion during outburst). Our study conclusively confirms the presence of the strong reflection hump in the 10-30 keV range for both phases, which arises when X-ray photons hit colder material and undergo Compton scattering. We discuss the reflection parameters during the two phases and propose that the potential reflection sites include the white dwarf surface and the accretion disk. We also explore the effect of intrinsic absorbers near the source and possible additional contributors affecting photons in X-rays. We also measured a WD mass of $\sim 1.2 M_\odot$ from the broadband spectral modelling.

Summary and Future Prospects

We have analysed some CV sources belonging to different classifications, and studied their X-ray timing and spectral properties to understand the accretion physics in these systems. For CD Ind, we have found that this asynchronous polar system have a weak Compton reflection denoting tall shock height over the WD surface, and there are strong spectral variability during the spin cycle of the WD, signifying change in the strength of the overall absorber. In the unique intermediate polar Paloma, we have noticed a distinctive feature of much stronger orbital modulation compared to spin modulation, which is not common place in typical IPs. Presence of dense blob of material fixed in the orbital frame can be the reason behind this. We also confirm the presence of strong intrinsic absorber and weak Compton reflection in this source. As an extension, an inclusive broadband X-ray study using involving the remaining members of the rare class of asynchronous polar systems can give us the broad picture about the accretion physics in these rare systems, and in the context with other regular members of the magnetic CVs, i.e polars and IPs. The unique IP paloma gave indication that the warm ionised intrinsic absorber may be responsible for the soft X-ray features, like two other IPs NY Lup and V1223 Sgr studied in literature (Islam et. al., 2021, ApJ, 919, 2). To conclusively test that for Paloma, future high resolution spectroscopic study involving Chandra data will be useful.

Our study on SS Cyg portrayed a comparative picture of the accretion mechanism in this bright dwarf novae source during the quescence and outburst. We detected strong reflection amplitude during both the phases indicating the possible reflection sites as WD surface and accretion disk. By constraining the blackbody emission during the outburst, we calculated the scale height of the optically thick boundary layer. We measured a significantly high mass accretion rates and softer spectra during the outburst than the quiescence, revealing the change in accretion properties during the two phases. In future, securing the simultaneous broadband X-ray observation during the quiescence and outburst for a sample of other dwarf nova sources, a future study can give us a comprehensive picture of the location of the emitting plasma and possible reflection sites for these type of objects. Extension of broadband X-ray study involving simultaneous observation with soft X-ray telescopes (like XMM-Newton, Swift, Chnadra) and hard X-ray telescope (like NuSTAR) for other CV sources can be a routine exercise to obtain a thorough description of the accretion process for these systems. Future X-ray missions like XRISM with higher resolving power will also be helpful in revealing new interesting properties of the CVs.

_____   _____

Signature of Supervisor   Signature of Candidate

Prof. Vikram Rana   **Anirban Dutta**

Professor, RRI   Research Fellow, RRI

Astronomy & Astrophysics Group

Raman Research Institute (RRI)

Bengaluru 560080, Karnataka IN

List of Publications

Publications included in the thesis:

1. Dutta & Rana (2022a) *"A broadband X-ray study of the asynchronous polar: CD Ind"* by **Anirban Dutta**, Vikram Rana, *MNRAS, Volume 511, Issue 4, April 2022, Pages 4981–4990*

2. Dutta & Rana (2022b) *"Study of complex absorption and reflection in a unique intermediate polar Paloma"* by **Anirban Dutta**, Vikram Rana, *ApJ, Volume 940, Number 2, December 1, 2022, Article 100*

3. Dutta et al. (2023) *"A broadband X-ray study of the dwarf nova SS Cyg during quiescence and outburst"* by **Anirban Dutta**, Vikram Rana, *ApJ, Volume 957, Number 1, November 1, 2023, Article 33*

_____   _____

Signature of Supervisor   Signature of Candidate

Prof. Vikram Rana   **Anirban Dutta**

Professor, RRI   Research Fellow, RRI

Astronomy & Astrophysics Group

Raman Research Institute (RRI)

Bengaluru 560080, Karnataka IN

Date:

Place:

List of Figures

List of Tables

Introduction to the thesis

1.1 Cataclysmic Variable - A brief background

Stars in the night skies have always amazed the astronomers throughout the human civilizations. While the twinkling beauties have been the most common sight to the observers, occasional brightening and dimming for certain periods have caught the interest of the careful eyes. The extravagant show of brightening of some stars, as if they are newly born (*novae stella*), were observed for millennia by civilizations - both oriental and occidental (Clark & Stephenson, 1977). One such event seen frequently by the naked eye or early telescopes was the novae, where the magnitude of a star increased by several thousand times. In modern astronomy, the Nova Oph in 1848 was the first object to be publicly observed since 1670 and recorded by Hind (1848). More systemic studies on these objects revealed them to be a subclass of a particular type of stars, which were termed as cataclysmic variables (CVs). Historically, CVs were observed photometrically, and with the progress of astronomical data collection, it becomes evident that they are accreting binary systems which change their brightness aperiodically or periodically over a time scale of several seconds to several months due to certain factors involving their accretion geometry and accretion physics.

The first CV to be detected in X-rays is the dwarf nova SS Cyg by rocket experiments (Rappaport et al., 1974). The UHURU satellite made the discovery of the CVs - EX Hya (Warner, 1976) and the AM Her (Forman et al., 1978). More CVs started getting detected in the X-ray range with the introduction of more X-ray satellites like HEAO-1, EXOSAT, and Einestein (reviews of Cordova & Mason (1983); Córdova (1995)). A large number of CVs were detected (Verbunt et al., 1997) in the later ROSAT X-ay All-Sky survey. The numbers keep increasing with more recent X-ray surveys like the INTEGRAL survey, XMM-Newton survey, Chandra survey, and Swift XRT surveys.

1.2 Overview of accretion process in CVs

The accretion in the CV is driven by the Roche lobe overflow mechanism. Roche lobes are the regions within the equipotential surface that pass through the inner Lagrangian point (L_1) of the two masses in a binary system. In other words, the Roche lobe is the region surrounding a mass in a binary system where material in orbit is gravitationally bound to that particular mass. A diagram of the equipotential surfaces and different Lagrangian points are shown in the Figure. 1.1. Now, these masses can be in a detached, semi-detached, or contact configuration. For the detached configuration, two masses are
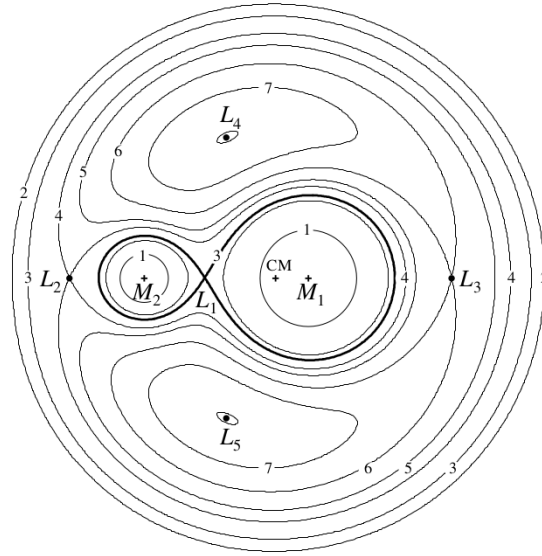
Figure 1.1: The sections in the orbital plane of the Roche equipotentials of a binary system with M_1 and M_2 ($q = M_1/M_2 = 0.25$)are shown with the lines marked with increasing numbers (for increasing value of the Roche potential). Different Lagrangian points are shown with L. The bold curve marks the equipotential surface passing through the L_1 point and denotes the Roche lobe of the mass M_1 and M_2. The center of mass (CM) of the binary is also marked. Figure is taken from Frank et al. (2002)

separate, each within their own Roche lobe. For the contact configuration, the two masses are in contact with each other through the L_1 point and form a common envelope. The CVs fall under the semi-detached configuration where one mass (the secondary, a late type main sequence star) fills up its Roche lobe, and the other mass (the primary, WD) is inside its Roche lobe and accreting materials from the former through the L_1 point.

The Roche geometry is specified by the binary separation (a) and the mass ratio ($q = M_2/M_1$, where primary mass is M_1, and that of secondary is M_2). The mass ratio is generally $\lesssim 1$ for the CVs. A schematic diagram for the Roche lobe geometry of the binary system is shown in Figure. 1.2. The commonly used formulas used for Roche geometry are given below (Warner, 1995; Hellier, 2001; Frank et al., 2002),

The binary separation a:

$$a = (\frac{G(M_1 + M_2)P_\Omega^2}{4\pi^2})^{1/3} \tag{1.1}$$

The distance of the primary from the L_1 point:

$$R_1 = a(0.2 - 0.227 \log q); \text{for} 0.1 < q < 10 \tag{1.2}$$

The distance of the secondary from the L_1 point:
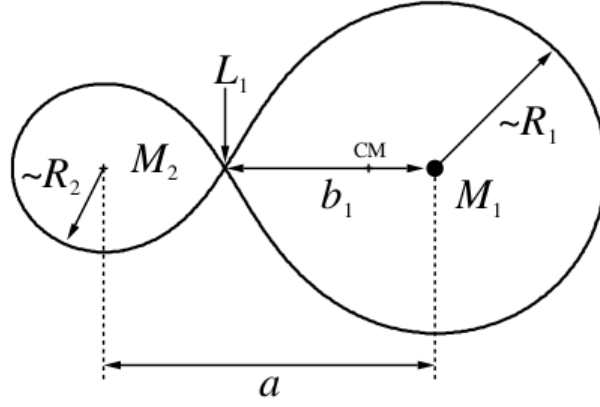
Figure 1.2: A schematic diagram of the Roche lobe geometry of a binary system (Frank et al., 2002)

$$R_2 = \frac{a 0.49 q^{2/3}}{0.6 q^{2/3} + \ln(1 + q^{1/3})}; for all q \tag{1.3}$$

The radius R_2 can be roughly treated as the radius of the secondary star, as it fills its Roche lobe. Now, as the stream of material passes through the L_1 point, it carries the angular momentum equal to that of the binary system at the L_1 point. These materials now follow a trajectory (unless the magnetic field of WD is strong enough to exert its influence) around the WD determined by the injection velocity and WD mass, as shown in Figure. 1.3, and sweeps past the closest approach to the WD and ultimately settles down to a circular orbit. The radius of the circular orbit where the angular momentum is equal to that of the binary at L_1 point, called the circularization radius, r_{circ}, and the radius of the closest approach of the initial ballistic stream to the WD, called as the minimization radius r_{min}, are formulated as:

$$r_{circ} = a(0.2 - 0.227 \log q)^4 (1 + q) \tag{1.4}$$

and,

$$r_{min} = a 0.049 q^{-0.464} \tag{1.5}$$

Gradually this ring of material spreads out in a thin disc via the angular momentum transport through the disk (Shakura & Sunyaev, 1973). Owing to the viscosity in the disc, the material rotating with smaller radii, thereby at a higher speed, encounters friction with the adjacent annuli of material at larger radii, rotating at a slightly lower speed, thus losing (radiating) energy. Due to this, the material at smaller radii must move to a bit smaller radii, and to conserve the angular momentum of the accreting material, some material should move to a bit larger radii, thus forming the disk. The outer edge of the disk is limited by the tidal interaction of the material with the secondary. The inner edge of the disk gets closer to the WD surface and forms a boundary layer (BL) before finally
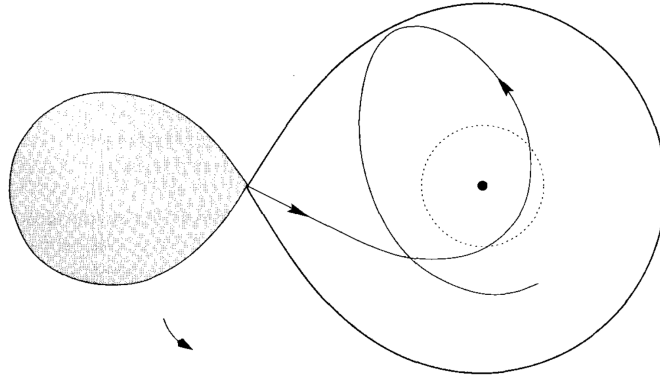
Figure 1.3: Illustrating the path of the stream emerging from the secondary filling its lobe (left side lobe). The primary WD is situated at the center within its Roche lobe (right side lobe). The stream intersects with itself, eventually creating a ring at the circularization radius marked by the dotted line. This trajectory is from the perspective of an observer orbiting with the binary system (rotating frame). One should envision the entire diagram rotating while the stream follows its path. Hellier (2001)

getting accreted by the WD. The disk gets replenished by the constant injection of mass from the secondary to the disc. Regarding the inner edge of the disc, in the presence of strong magnetic field of WD, the situation is a bit different. In this case, the magnetic field lines of the WD disrupt the disk at the magnetospheric radius (r_{mag}), where the ram pressure of the material equals the magnetic pressure (Figure. 1.4). It is given as:

$$r_{\mathrm{mag}} = 6.9 \times 10^{-2} M_1^{1/7} R_{\mathrm{WD}}^{-2/7} L^{-2/7} \mu^{4/7} \ cm \tag{1.6}$$

where $L = \frac{GM_1\dot{M}}{R_{\mathrm{WD}}}$ is the accretion luminosity and $\dot{M}$ is the mass accretion rate by the WD.

Now, for a CV binary to continue the steady, long-lived mass transfer, the size of the mass donating secondary and its Roche lobe should be adjusted so that the secondary always fills up its Roche lobe. The condition is governed by the following expression (Frank et al., 2002):

$$\frac{\dot{R_2}}{R_2} = 2\frac{\dot{J}}{J} + 2\frac{-\dot{M_2}}{M_2}(\frac{5}{6} - q) \tag{1.7}$$

Here $\dot{M_2}$ is negative (as secondary is losing mass); therefore $-\dot{M_2}$ is positive. For a sustained stable mass-transfer, we require the Roche lobe radius of the secondary to decrease, i.e $\dot{R_2}$ is negative), which is satisfied by $q < 5/6$ and $\dot{J} < 0$, i.e. the total angular momentum (J) of the binary is decreasing. There are two ways the decrease of angular momentum can happen: (*i*) via magnetic braking (MB), where the stellar wind material from the secondary is thrown away following the secondary's magnetic field lines, thereby decreasing the angular momentum of the binary system, and, (*ii*) via gravitational radiation (GR) where the rotation of two closeby gravitating body generates
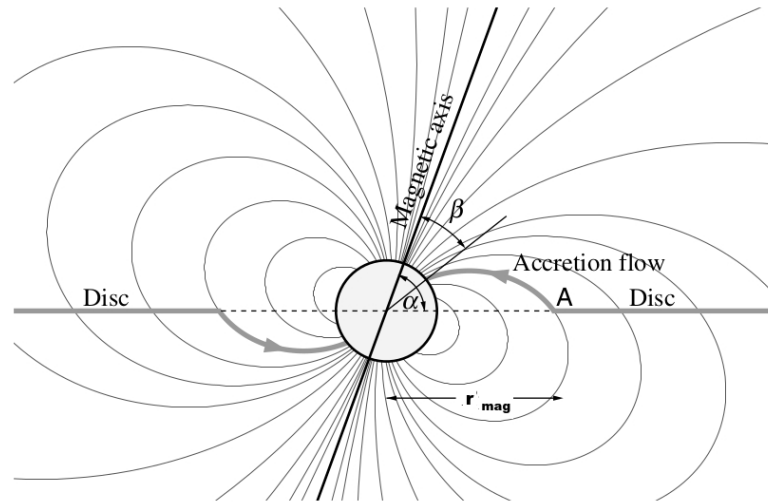
Figure 1.4: Diagram showing the materials from the inner edge of the disk being channelled to the WD poles via the magnetic field lines, from the magnetospheric radius (r_{mag}). Frank et al. (2002)

a gravitational wave, thereby losing energy and angular momentum, causing them slowly spiralling inward. While the gravitational radiation is believed to work for all CVs (Kraft et al., 1962), the additional effect, the magnetic braking, is the dominant process for systems with $P_\Omega > 3$hr (Knigge et al., 2011). A number distribution of the systems with orbital periods is shown in Figure. 1.5. There is apparently a period window $P_\Omega \sim 2 - 3$hr, called a period gap, with very few systems. The hypothesis is that during that period, the binary is in detached configuration. MB process becomes less effective somewhere below $P_\Omega \sim 3$hr, temporarily halting the sustained mass transfer from the secondary as the secondary detaches from the Roche lobe, thereby stopping the accretion. The mass transfer starts again with the secondary correcting its radius (in a thermal i.e. Kelvin-Helmholtz timescale of the secondary $\sim 10^8$yr) according to the new Roche lobe size, and the binary separation shrinks with the GR process kicking in (Webbink & Wickramasinghe, 2002; Hellier, 2001). Therefore, there is an apparent lack of systems in the period gap. However, this standard picture is altered in the presence of a strong magnetic field, which may create accreting systems in the period gap, owing to the coupling of the field to the secondary and influencing this picture of evolution.

1.3   Cataclysmic Variable - Classifications

The accreting binary systems of the CVs consist of a white dwarf (WD) star, also described as primary in the binary context, which accretes the materials from a late-type main sequence star, or the secondary, via the Roche lobe overflow mechanism. Depending on the strength of the magnetic field of the WD, the CVs are classified into two groups: magnetic cataclysmic variables (mCVs) and non-magnetic cataclysmic variables (nmCVs).
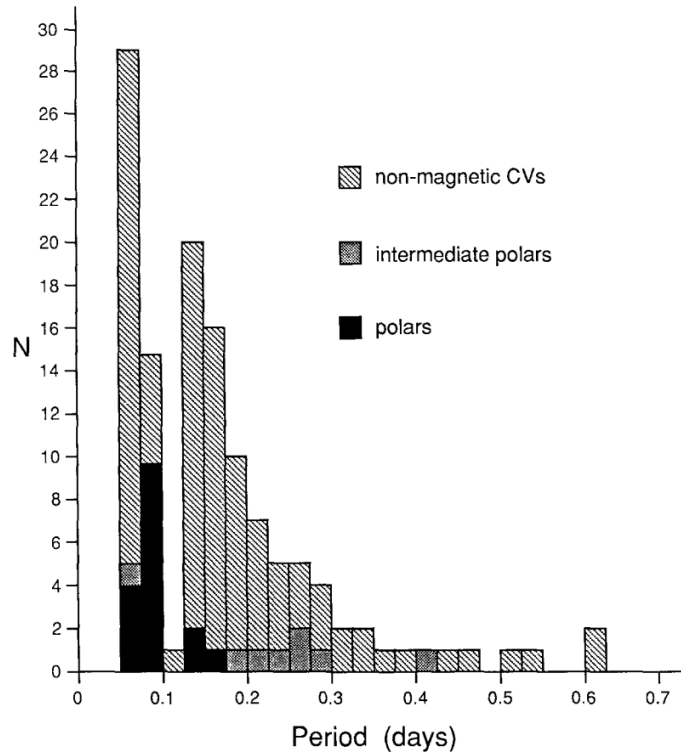
Figure 1.5: Distribution of the number of the CVs with the orbital periods. Cropper (1990)

As the name indicates, the mCVs have a strong magnetic field of the WD($> 10^5$G), whereas the WD in nmCVs have weaker ($< 10^5$G) magnetic fields. The strength of the magnetic field is a dominant factor in determining the accretion process and the geometry of these systems.

1.3.1 Types of Magnetic Cataclysmic Variables

The accretion in the mCV is governed by the magnetic field lines, owing to the strong magnetic fields. The strongest field ($\sim 10^7 - 10^8$G) systems are termed as Polar, and the systems with comparably lower magnetic field strengths ($\sim 10^5 - 10^7$G) of the WD are Intermediate polar (IP). In the case of Polars, the magnetic field lines are strong enough to exert the influence at the L_1 point (Figure. 1.6) of the binary, giving rise to a direct transfer of the material from the L_1 point to the WD poles via magnetic field lines. The strong magnetic field of the WD in the polars produces cyclotron emission in optical bands, which is strongly polarized (as strong as $\sim 50\%$), hence the nomenclature. One important temporal property of the polars is the synchronism of the binary period (P_Ω) and the WD spin period (P_ω). This is caused by the strong magnetic field lines of the WD, which get intertwined with the magnetic field lines of the secondary star, causing the magnetic locking. This results in the scenario where the same face of WD always looks at the secondary throughout all the orbital cycles. However, there exist exceptions in few systems (V1432 Aql, CD Ind, BY Cam, V1500 Cyg, IGR J19552+0044, 1RXS J083842.1-282723, SDSS J084617.11+245344.1) - the asynchronous polars (APs), which have a very
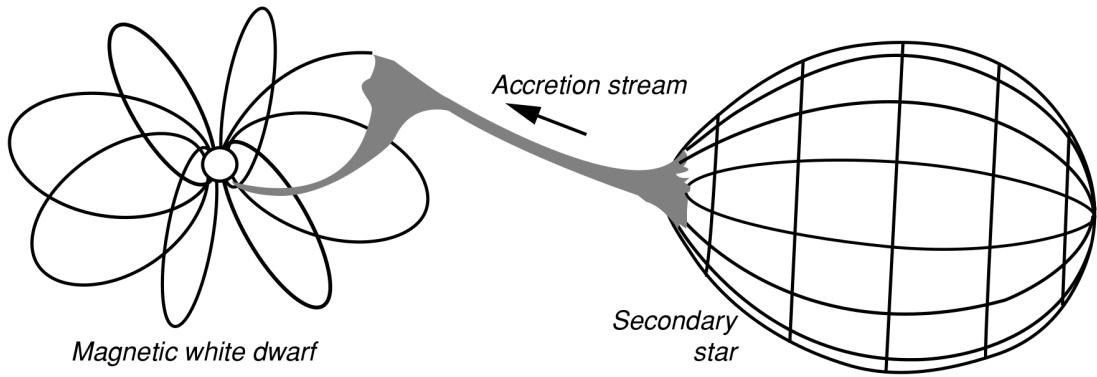
Figure 1.6: Schematic view of a polar. Seward & Charles (2010)

slight difference between the WD spin period and the binary orbital periods ($(P_\Omega - P_\omega)/P_\Omega \lesssim 2\%$), and in the process of acheiving the synchronosity with the gradual change in the spin period. There is no consensus regarding the reasons for this asynchronicity. While for one source V1500 Cyg, there are detection of nova shells around it (Honda et al., 1975; Stockman et al., 1988; Schmidt et al., 1995), implying nova eruption be a reason for the synchronicity, the presence of nova shells remains undetected for other APs (Pagnotta & Zurek, 2016). Also, amount of the nova recurrence times would be very frequent (~ 5000yr) if we consider the number of the APs that we detect compared to the number of the observed polars (Warner, 2002; Mukai, 2017). Therefore, there should be other channels for this asynchronism.

For the IPs, the comparatively weaker magnetic field of the WD allows the material to form a partial accretion disk around the WD; however, it disrupts the disk at the magnetospheric radius and channels it through the field lines to the WD poles at the final phase of the accretion (Figure. 1.7).
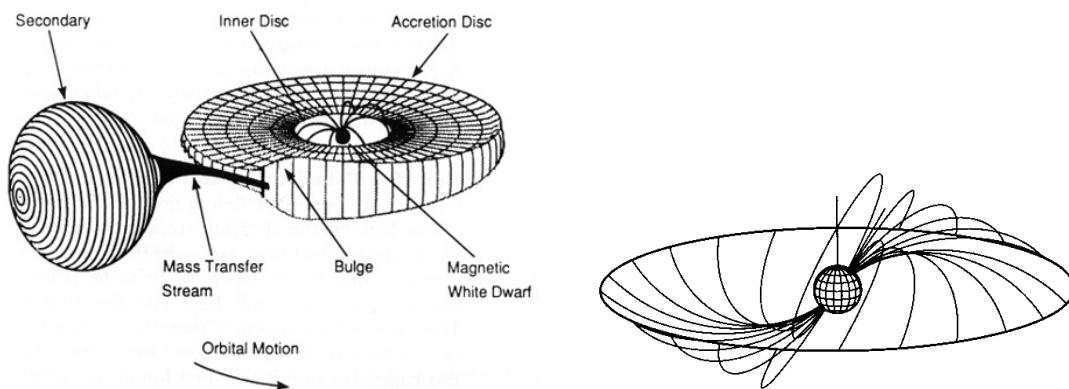
Figure 1.7: The schematic figure of an IP on the left. The right figure shows the zoomed version of the accretion curtain formed near WD, as the material follows the magnetic field lines from the inner edge of the partial accretion disk towards the magnetic pole of the WD. Hellier (2001)
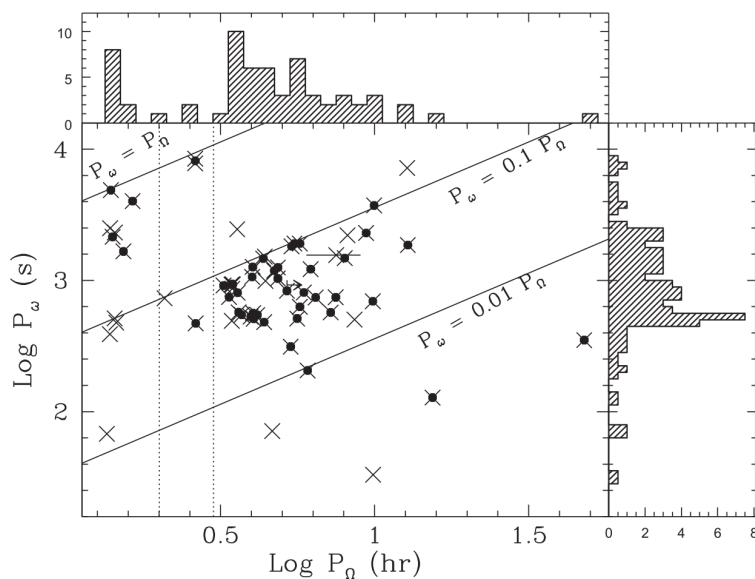
Figure 1.8: Distribution of the observed IPs in the $P_\omega - P_\Omega$ plane. The cross marks and cross with circles both denote the observed IP population. The vertical dashed line denotes the period gap. de Martino et al. (2020)

While polars have perfect synchronicity owing to the magnetic locking between the WD and the secondary, the IPs have a mismatch between spin and orbital periods of the order of $P_\omega/P_\Omega \sim 0.01 - 0.1$ due to lack of the magnetic locking. A figure is shown in Figure. 1.8 presenting the distribution of the observed IPs in $P_\omega - P_\Omega$ plane.

The configuration of the partial accretion disk in IP depends on certain key binary parameters - the magnetospheric radius (r_{mag}, where the ram pressure of the incoming stream balances the magnetic pressure), the circularization radius (r_{circ}, the radius for which the angular momentum of the material in a Keplerian orbit is equal to the angular momentum of the material leaving the L_1 point), and the minimization radius (r_{min}, the radius of minimum approach of the free-falling accretion stream). Usually, in IPs $r_{mag} < r_{min}$, which leads to the formation of a partial accretion disk until its inner edge encounters the r_{mag}. After that, the material follows the magnetic field lines by forming the accretion curtain and falls on the WD poles. For some systems, $r_{mag} > r_{circ}$, there will not be the formation of the partial disc, and the accretion will be fed by the accretion stream only. There are certain cases (e.g. FO Aqr, EX Hya during outburst) where disk overflow happens occasionally, and the accretion stream flows over the disk to finally be channelled by the magnetic field lines of the WD, giving rise to both stream-fed and disc-fed accretion (Hellier, 1993; Mukai et al., 1994).

There are few peculiar IPs (Paloma, Schwarz et al. (2007); Joshi et al. (2016); Dutta & Rana (2022b), SWIFT J0503.7-2819, Rawat et al. (2022)), which have much less asynchronicity ($\sim 10 - 20\%$) compared to the usual IPs ($\sim 90\%$). Paloma resides in the period gap; the SWIFT J0503.7-2819 resides below it. These systems might be transitional objects
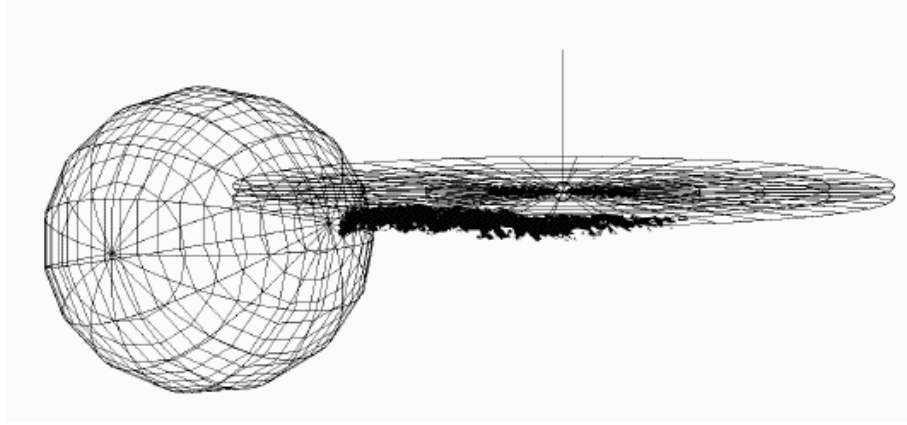
Figure 1.9: A schematic figure of a nmCV, showing material coming from the secondary star, forms a complete accretion disk around the WD. Hellier (2001)

that are thought to be evolving towards a polar from an IP (Norton et al., 2004; Schwarz et al., 2007). The probability is that these systems are observed at an interesting phase of the mCV evolution. The binary separation gradually decreases as the binary systems lose the angular momenta via magnetic breaking and gravitational radiation. The systems evolve from a larger orbital period to a smaller orbital period, crossing the period gap.

In this context, in the Figure. 1.5, the polars occupy the left side of the distribution ($P_\Omega < 2$hr) with GR dominated binary angular momentum loss. The majority of the IPs occupy the right side of the distribution ($P_\Omega > 3$hr), with MB being the process for binary angular momentum loss; however, they are also present on the left side (below the period gap, systems like EX Hya, HT Cam, V1025 Cen, V598 Peg etc.). Now, the standard picture is, with a shrinking orbit, the magnetic field lines of WD and the secondary can interlock if the magnetic field of the WD is high enough (comparable to the strength of the WD in polars 10^7G), and can evolve into polars below the period gap. Whereas, the IP systems with low magnetic field strength of WD will not achieve synchronism due to lack of magnetic locking, even below the period gap, and still remain as IPs (Norton et al., 2004; Hellier, 2001). However, the evolution of IPs, or in general mCVs, is still a developing field, and the discovery of more systems in the period gap will potentially shed light on this topic.

1.3.2   Types of Non-Magnetic Cataclysmic Variables

In the absence of the strong magnetic fields of the WD ($< 10^5$G), the accretion takes place via a fully formed accretion disk in the nmCVs (Figure. 1.9). The accreting material rotates in a Keplerian disk in the binary plane in these systems. Near the WD, an intermediate layer forms between the WD surface and the inner edge of the disc called the boundary layer (BL). The major sub-classifications of these types of systems are done based on the outburst phenomenon of the disc, caused by thermo-viscous instability (Osaki, 1974). The material injected to the disk from the secondary exceeds the mass
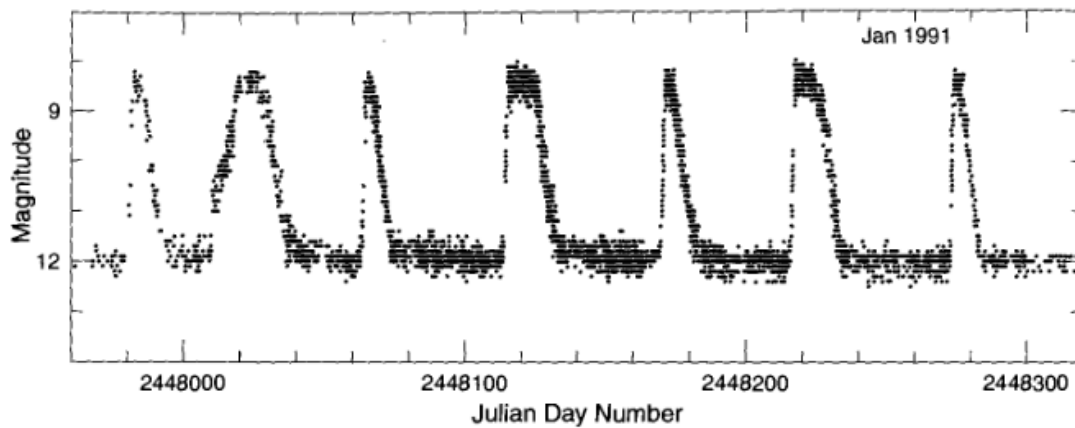
Figure 1.10: A 1-year long optical lightcurve of the DN source SS Cyg, showing regular outbursts. Hellier (2001)

accretion rate by the WD from the disk, causing a gradual accumulation of material in the disc. After a certain critical surface density is reached, a chain reaction kicks in, rapidly increasing temperature, viscosity, ionization, and opacity, and a heating wave sets in. This leads the disk to the outburst and enhanced mass accretion by the WD. Two important subtypes of the nmCVs are the Dwarf Nova (DN) and the Nova-likes(NL). For the DN, the disk periodically goes into the outburst and then comes back to the quiescence phase once the disk density goes below a certain critical density after the enhanced mass accretion by the WD stops (Figure. 1.10).

For the NL, the disk remains permanently in the outburst. In this case, the disk always maintains the critical density according to the mass injected into the disk from the secondary. There are two variants of the usual theme of DN and NL systems: the Z Cam type systems and the SU Uma type systems. In the Z Cam type systems, the disk remains in a standstill, a borderline between DN and NL, and are characterized by outburst activity inter-spaced with periods of NL steadiness, which is caused by small change in mass injection rate to the disk leading to a change of state. In the SU UMa type systems, super outbursts take place, which are slightly brighter than the regular outbursts, and the super outbursts are triggered by the normal outbursts.

There are two other important types of CV systems - Classical Nova (CN) and Recurrent Nova (RN). While the variability of these systems happens owing to the nova eruption, which is not a property related to the magnetic field of the systems, therefore, these systems are usually placed under the category of nmCVs. But the reader should remember that, in both these systems, there is no outburst in the disc, and the presence of a fully formed disk is also not mandatory since the mCVs can equally undergo nova eruption during their lifetimes (eg. V1500 Cyg, V697 Sco, etc.). In a nova eruption, the continuous accumulation of the material, which is rich in hydrogen, on the WD surface starts raising the temperature of the surface. When the temperature reaches several mil-

lion kelvin, it triggers the C-N-O cycle, where hydrogen fuses into helium. This is a thermal runaway reaction, expanding the surface of the WD quickly against the immense gravity and subsequently exploding the outer shell violently (Starrfield et al., 1972; Prialnik & Kovetz, 1995; Chomiuk et al., 2021). While this explosion ejects outer layer mass of roughly $\sim 10^{-4} \, M_\odot$ at a speed of several thousands of kilometers per second and producing roughly a million times the solar luminosity, the WD itself does not explode like a supernova. For a CN, the recurrence time is expected to be somewhere around a few tens of thousands of years to a few million years, depending on the mass accretion rate of WD, and expected to undergo several nova eruptions during the binary lifetime of the CV ($\sim 10^8 - 10^{11}$ yr); however we can only get the chance of seeing such events (along with the available historical records of modern astronomy) from any particular CN system only once. The galactic nova eruption rate is expected to be $20 - 70 \, \text{yr}^{-1}$, while detection rate is $\sim 5 - 15 \, \text{yr}^{-1}$ (Shafter, 2017). The RNs are the systems with much higher mass accretion rates, causing multiple nova eruptions to be detected from the same system after some time duration, generally several years or decades. While a conventional CV system can be a RN (like T Pyx, Chomiuk et al. (2014)), the symbiotic star systems (like RS Oph, Page et al. (2022)), where the primary is an accreting WD, but the secondary is a red giant instead of a late type main sequence star, thereby accretion via stellar wind from secondary takes place instead of Roch lobe overflow) can also become RN.

1.4 X-ray properties of CVs

The focus of this thesis is the X-ray properties of the CVs. While CVs have been abundantly observed in optical and around (IR-optical-UV) wavebands, the X-ray features unveil several unique properties of the CV. The IR-optical-UV emission arises from the accretion disk ($T \sim 3000 - 30000$K, outer edge to inner edge), the bright spot (where the stream hits the disc, $T \lesssim 10000$K), the secondary star ($T \sim 3000 - 5000$K, generally spectral type ranging from G8 to M6), the WD ($T \sim 10000 - 50000$K). In the case of Polars, polarised cyclotron lines appear in the optical band.

The X-ray emission in the CVs comes from solely the final stage of the accretion process. Generation of photons in the X-ray range with energies $\sim$ a few hundreds of eV to few tens of keV requires an immensely powerful process. This is possible by forming supersonic shocks in the vicinity of the WD, as the accreting material encounters the WD atmosphere and finally settles on it. The temporal and spectral properties of the emission and absorption features in X-rays provide unique clues about the geometry and properties of the CVs. We have discussed this in detail for different types of CVs in the following subsections.

1.4.1 X-rays from Magnetic CVs

In the mCVs, the material follows the magnetic field lines at the final stage of the accretion. The material, arriving at a supersonic velocity above the pole(s) of the WD,
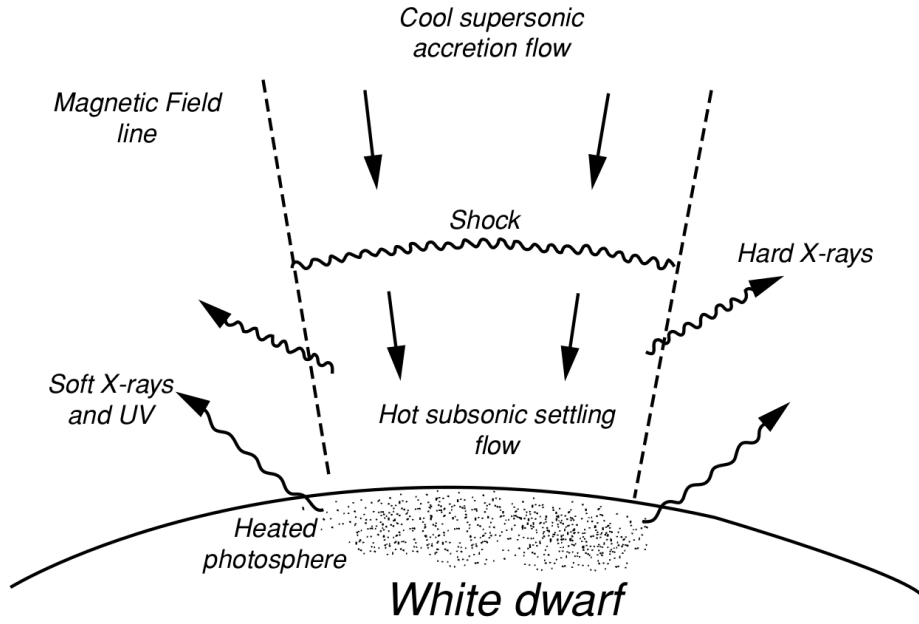
Figure 1.11: A schematic figure of the accretion column over the magnetic poles of the WD. Seward & Charles (2010)

creates a strong shock with the WD atmosphere. A schematic diagram of the X-ray emitting region in mCVs is shown in Figure. 1.11. Post the shock front; the material travels at velocity $\sim (1/4)v_{ff}$, where v_{ff} is the free-fall velocity of the material above the shock front. The difference in the kinetic energy is converted into the thermal energy and generates the hard X-rays ($\sim$ few keV) above the poles of the WD. The shock temperature T_s is given as (Aizu, 1973),

$$KT_s = \frac{3}{8} \frac{GM_{\mathrm{WD}}\mu m_p}{R_{\mathrm{WD}}} \tag{1.8}$$

Here, G is the gravitational constant, M_{WD} is the WD mass (=M_1 as the notations used in previous sections), μ is the mean molecular weight of the plasma (assumed to be 0.615), m_p is the proton mass, R_{WD} is the WD radius.

In the post-shock region (PSR), the material or the plasma is fully ionised and gradually slows and cools down. Thermal Bremsstrahlung is the dominant cooling process of the plasma (Lamb & Masters, 1979) and gives rise to the multitemperature plasma as it cools. The plasma density gradually increases, and the temperature and velocity gradually decrease towards the bottom. In the lower temperatures ($KT \lesssim 1$keV), the line cooling via ionized emission lines also becomes important Gehrels & Williams (1993). In the Aizu model of the PSR, the resulting shock height of the plasma is such that the total Bremsstrahlung cooling time of the shocked plasma is equal to the time required for the plasma to settle down on the WD surface.

The X-rays emitted from the PSR interact with the intrinsic absorber like the accretion

stream or accretion curtain in the source, and any intervening medium, like the interstellar medium (ISM), while reaching the observer. A part of the X-rays can get Compton reflected by the WD surface and produce an excess (hump-like feature) in the spectrum over 10 keV, where Compton scattering is the dominating process (George & Fabian, 1991). In addition, a part of the emitted X-rays will undergo photoelectric absorption, giving rise to fluorescence emissions, most notably an iron fluorescence line at 6.4 keV. It is believed that the strength of the iron fluorescence line is correlated to the Compton reflection, as both physical processes can take place in a similar region of the WD surface. The contribution to the Fe 6.4 keV line comes from both the WD surface as well as intrinsic absorber in the mCVs (Ezuka & Ishida, 1999)

Now, particularly for **polars** among mCVs, in addition to the above physical processes in X-rays, there is generally a prominent soft X-ray blackbody ($\sim$ few tens of eV) component in the spectra (Lamb & Masters, 1979). This component most likely appears by blobby accretion, where blobs of accreting plasma, unaffected by the accretion shock, can be plunged deep into the WD photosphere, liberating kinetic energy and heating up the polar region, thereby producing blackbody emission (Kuijpers & Pringle, 1982). The modulation in X-ray lightcurves over a complete binary cycle of polar is mostly due to the self-occultation of the part or complete X-ray emitting polar region by the WD itself due to inclination between spin and magnetic axis, along with absorption due to X-rays passing through the accretion stream. X-ray Eclipse, due to to occultation of the X-ray emitting region by the secondary, can also be present for polars. In this context, note that eclipse can occur for other mCVs (IPs, APs) as well as nmCVs (DNs, NLs).

In the IPs, the X-ray spectra are generally harder compared to the polars. Consequently shock heights are larger in the IPs, as the Bremsstrahlung cooling time of the shocked plasma is more. The mass accretion rates, the accretion footprint (King & Shaviv, 1984), and the complex intrinsic absorber are generally higher in IPs than polars. In the case of the IPs with partial accretion disk, accretion curtain is formed between the WD poles and the inner edge of the partial accretion disk, and material is channelled through the curtain to fall on the polar region. The X-ray modulations in the lightcurves of IPs are seen over orbital and spin cycles. While orbital variations (Parker et al., 2005) are mostly attributed to the disk systems by the absorbing material fixed at binary phase, like material present at the outer edge of the disk or stream-disk interaction region, with a suitable geometry along the line of sight, it can also arise in the absence of the disk due to the variation of the accretion on the opposite WD poles. The spin modulations (Norton et al., 1996) are caused by the absorbers present in the pre-shock flow, e.g. the accretion curtain (with disk) or the accretion stream (without disk). Also, the self-occultation of the X-ray emitting polar regions by the WD can contribute to the spin modulations. For the stream-fed IPs, devoid of disks, another prominent periodic modulations arise in the lightcurves over the beat frequency (beat between spin and orbit, $\omega - O\omega$) and at the harmonic $2\omega - \Omega$ (Wynn &

King, 1992). This happens because the dominant accretion on a pole flips over a beat cycle when the accretion is stream-fed. However, the X-ray modulation signatures of the IPs in the power spectra can be complex with contributions at spin, orbit, and beat frequencies along with the sidebands and harmonics, depending on the complex modulating factors (disk-overflow, asymmetry in geometry, energy-dependent photoelectric absorption etc) (Norton et al., 1996).

In the case of APs, there is modulation over the beat cycle since the relative orientation of the WD and the secondary changes over a beat cycle, giving rise to pole-switching (single pole accretion, e.g. CD Ind), or change of dominant pole of accretion (double pole accretion, e.g. V1432 Aql). The spectra are generally harder in the AP samples detected so far and limited in number.

1.4.2   X-rays from Non-magnetic CVs

The shock formation in the BL is the primary site of the generation of hard X-rays in the nmCVs like DNs and NLs, where disk instability causes regular modulations of the fluxes over a timescale, ranging from weeks to months. DN accretion theory suggests the presence of BL between the inner edges of the disk and the WD surface. The properties and location of the BL and its emission are sensitive to the mass accretion rate. During the quiescence, a strong shock is formed in the BL due to the velocity mismatch of the inner edge of the disk, rotating at Keplerian velocity, and the BL, rotating much slower, comparable to the WD spinning velocity. This results in kinetic energy being transferred into thermal energy in the form of X-rays. The kinetic energy of the material in the BL is equal to half of the gravitational potential energy of the WD. By relating the thermal energy of the accreting material with the gravitational potential energy of the WD, the shock temperature can be expressed as,

$$KT_s = \frac{3}{16} \frac{GM_{\text{WD}}\mu m_p}{R_{\text{WD}}} \tag{1.9}$$

where the symbols carry same meaning as that of the Eqn. 1.8.

The hot (10^8K) gas in the optically thin BL cools down by thermal Bremsstrahlung emission, mostly in hard X-rays. As the matter cools down before settling onto the WD surface, the X-ray continuum is characterized by multi-temperature components. Moreover, a part of this hard X-ray undergoes photoelectric absorption by the WD surface and/or accretion disk and emits neutral iron K_α emission at 6.4 keV. Another part gets reflected by the WD surface and/or accretion disk via Compton reflection (George & Fabian, 1991; Matt et al., 1991). The reflection hump is produced mainly by the Compton scattering of hard X-ray photons to energies around 10–30 keV, as also seen in mCVs.

Now, during the enhanced mass accretion rate of the outburst in DNs, the BL becomes optically thick to its own radiation, approaching a blackbody condition, and radiates mostly in very soft X-rays with a temperature 10^5K (Pringle & Savonije, 1979; Narayan
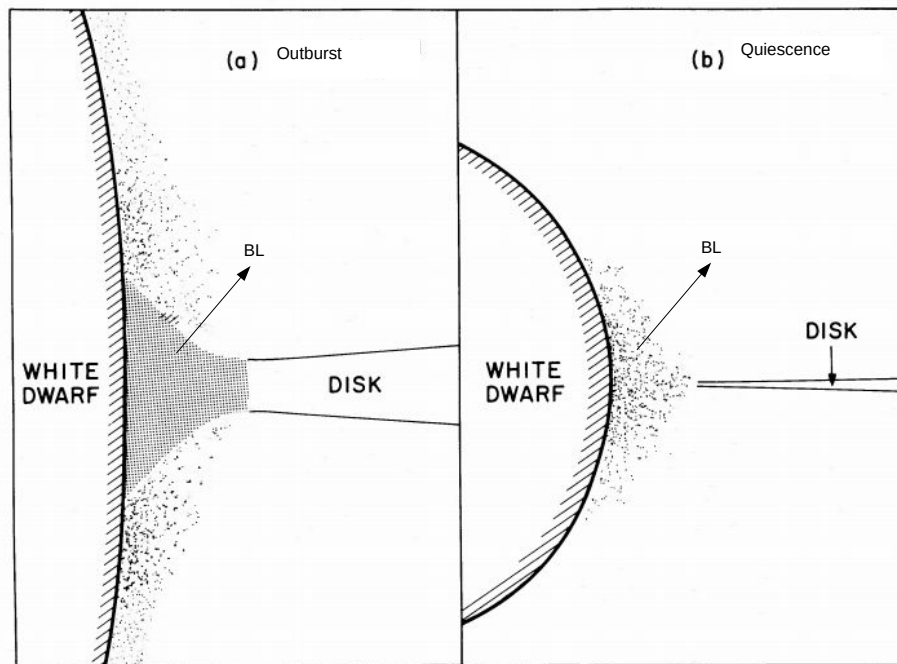
Figure 1.12: A schematic diagram showing the accretion in DN during quiescence and outburst. The BL is optically thin during quiescence and optically thick during outburst. Patterson & Raymond (1985a)

& Popham, 1993; Popham & Narayan, 1995). This has been tested with multiple broadband observations (Ricketts et al., 1979; Jones & Watson, 1992; Wheatley et al., 2003). A schematic diagram of the X-ray emitting BL in nmCVs is shown in Figure. 1.12. Even though the outburst phase produces mostly soft X-rays, there is clear detection of hard X-rays with temperatures up to a few keVs. One possible explanation for these residual hard X-rays is due to the vertical density gradients in the accretion disk, where a fraction of optically thin accreting materials emit hard X-rays (Patterson & Raymond, 1985a,b). Another popular line of thought by Ishida et al. (2009) and Wheatley & Mauche (2005) suggests that hard X-rays arise from the optically thin corona formed over the disk.

The X-ray spectral features of the NLs are similar to the DNs in outbursts due to the similarities of the disk instability properties of both.

Now, for the eruptive transient CV systems - the nova subclasses CN and RN, the X-ray generation occurs from thermonuclear runaway reaction (TNR) and from shock formation by the expanded ejecta. When TNR is achieved, it leads to an explosion accompanied by the ejection of the accreted material. As the ejecta becomes optically thin with time, the residual nuclear burning on the WD surface is exposed, and it is identified as a supersoft X-ray source (SSS) (Krautter, 2008; Henze et al., 2014), peaking in soft X-ray with a hard X-ray tail. These SSS can last in the sky from days to months (Gordon et al., 2021). Apart from that, thermal hard X-rays are also produced in nova eruptions due to shock waves

compressing and heating the plasma to X-ray temperatures (Sokoloski et al., 2006; Bode et al., 2006; Sokolovsky et al., 2022). Shock X-ray emission is a universal feature of all the novas (CN and RN) (Mukai et al., 2008), irrespective of whether they are embedded in a dense wind from the giant secondary, as seen in the symbiotic star systems (as mentioned earlier, they can also cause nova), or not embedded, as seen in the CVs. For the embedded systems (for eg. RS Oph, Page et al. (2022), V745 Sco, Page et al. (2015)), the ejecta creates the shock with the existing common enveloping dense wind. For the non-embedded systems, presumably, the shock is formed between an initial slow-moving ejecta with a subsequent fast-moving ejecta (e.g. V382 Vel, Mukai & Ishida (2001), T Pyx, Chomiuk et al. (2014)).

1.5   Thesis Outline

In the next chapter (Chapter 2), we discussed different X-ray observatories and the general data reduction and analysis techniques. In chapter 3, we have delved into the broadband X-ray properties of the AP source CD Ind. In chapter 4, the broadband X-ray properties of the unique IP source Paloma have been covered. In Chapter 5, we have compared the broadband X-ray properties of the DN source SS Cyg during its quiescence and outburst. In chapter 6, we have described the X-ray properties of two more AP sources, V1432 Aql and BY Cam. In chapter 7, we have summarized the results from the thesis and discussed the future scopes of our work.

X-ray observatories and data analysis

2.1 X-ray observatories

Observing the CVs in the X-ray band provides unique clues in knowing the system properties. It is possible with a range of X-ray telescopes currently active and operated by space agencies globally. The important point for X-ray observation from any astrophysical sources is that Earth's atmosphere is opaque to the incoming X-rays . The only way to observe X-rays of astrophysical origin is to go beyond Earth's atmosphere. Multiple space-based X-ray observatories, which are currently active, are regularly employed to study the CV sources. The Chandra (Weisskopf et al., 2002) observatory carries high-resolution spectroscopic instrument HETG (0.4-10.0 keV), which is used for observing the line emissions from CVs, abundant in the CV spectra, and study them in great detail. The high-resolution imaging instrument (ACIS) is useful for precisely locating the crowded galactic centre region, which is home to significant number of CV sources. The NICER observatory (Gendreau et al., 2016) is generally employed to monitor long-term variation of the CV sources in 0.3-12.0 keV. Particular to this thesis work, the observations from XMM-Newton, NuSTAR, Swift and Suzaku observatories are extensively used to study the specific CV sources and have been discussed in the following sections.

2.1.1 XMM-Newton

The X-ray Multi-Mirror Mission (XMM-Newton, Jansen et al. (2001)) satellite (Figure 2.1) consists of three X-ray instruments - European Photon Imaging Camera (EPIC), Reflection Grating Spectrometer (RGS, den Herder et al. (2001)), and the Optical Monitor (OM, Mason et al. (2001)). The EPIC instrument, having imaging capabilities, contains three detectors - PN (Strüder et al., 2001) and two similar MOS (Turner et al., 2001) detectors. PN detector is placed behind one telescope, receiving X-ray photons with PN-CCD arrays. The EPIC-MOS detectors are two in number and utilize other telescopes to receive X-ray photons using Metal Oxide Semiconductor CCD arrays. These three EPIC detectors (one PN, two MOS) have been used to observe the source in 0.3-10.0 keV energy band. EPIC has a field-of-view (FOV) of 30 arcmin, with spectral resolution of $E/\Delta E \sim 20 - 50$ (~ 120eV at 6 keV), and angular resolution of ~ 6arcsec full-width-half-maxima (FWHM), and ~ 15arcsec half power diameter (HPD). The temporal resolution of EPIC varies (7 μs-73ms for PN, 1.75ms-2.6s for MOS) depending on which mode the observation is taken, according to the specific requirement of that particular observation. The two telescopes, working for MOS1 and MOS2, are also equipped with two grating spectrometers, RGS1
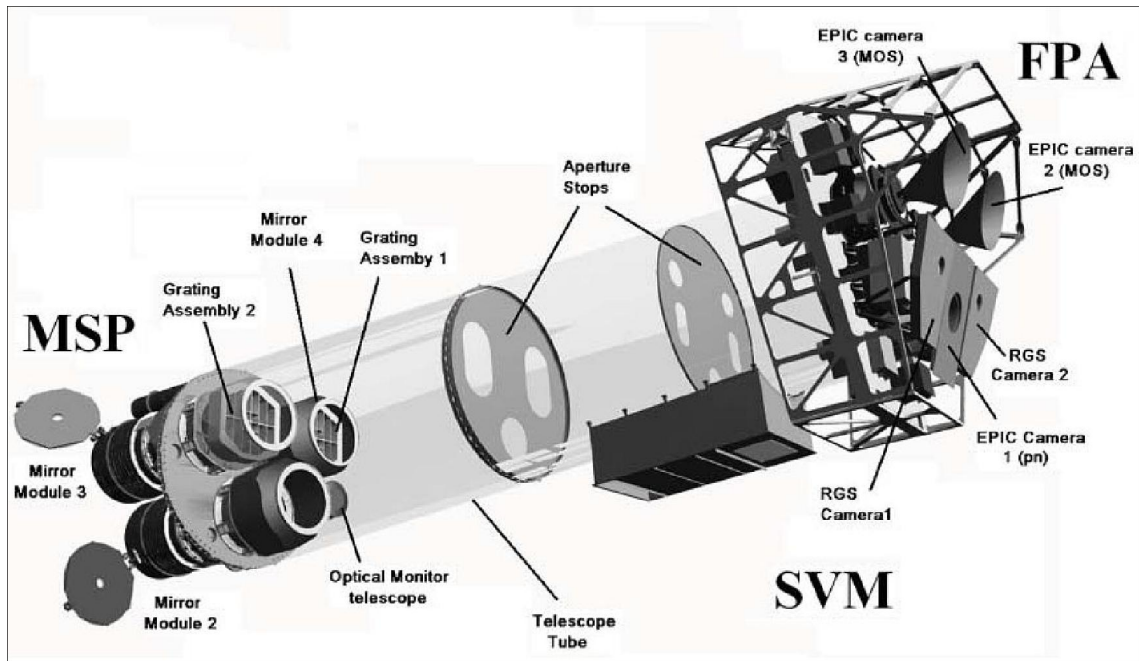
Figure 2.1: A schematic diagram of the XMM-Newton observatory.

and RGS2, which are part of the non-imaging RGS instrument. Nearly half of the X-ray flux received by those two telescopes is sent to MOS detectors, whereas the RGS uses the other half. The spectra from the grating spectroscope, which can resolve (spectral resolution $E/\Delta E \sim 200 - 800$) emission and absorption lines in 0.35-2.5 keV band (5-38 Å), comprising the important K_α transition from ionised C, N, O, Ne, Mg, Si elements as well as Fe L-Shell emission lines. The OM instrument is used to observe in the bandpass 180-600 nm.

The XMM-Newton data is reduced using the Science Analysis System (SAS) software (Gabriel et al., 2004). The calibration files are used from the Current Calibration Files (CCF) database, hosted by the XMM-Newton science operation ceter. The SAS tools `epproc` and `emproc` produce science products from PN and MOS data. `evselect` is used to clean the data from soft-proton background flaring and select specific criteria for extracting the lightcurves and spectra. In general, selection criteria like `PATTERN<=4` for PN to consider the single and double events and `PATTERN<=12` for MOS to consider single, double, triple and quadruple events are used. Standard filtering criteria `#XMMEA_EP` along with `FLAG==0` and `#XMMEA_EM` are used for PN and MOS data, respectively. The `epiclccorr` is used to obtain the background subtracted source lightcurves and to implement the corrections for vignetting, bad pixels, chip gaps, point-spread-function (PSF), and quantum efficiency. `barycen` is used to obtain the barycenter corrected lightcurves. `rmfgen` and `arfgen` are used to generate the response matrix files (RMF) and ancillary response files (ARF). `rgsproc` is used for extracting science products from RGS data. For this thesis work, we have not explicitly analysed OM data.
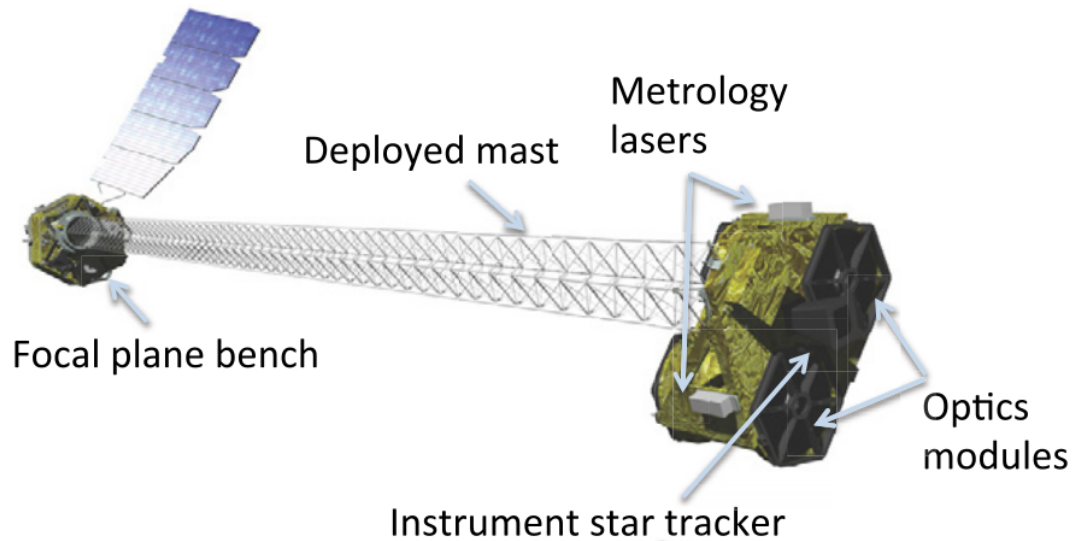
Figure 2.2: A schematic diagram of the NuSTAR observatory.

2.1.2 NuSTAR

The Nuclear Spectroscopic Telescope Array (NuSTAR, Harrison et al. (2013)) is an imaging-focusing telescope (Figure 2.2), consisting of two identical focal plane modules - FPMA and FPMB. This is the first imaging telescope capable of focusing hard X-rays (3.0-78.0 keV) with very high sensitivity. The two telescopes of NuSTAR follow the Wolter-I configuration, employing grazing incidence mirrors to bring the X-rays to their focus. Each telescope module is equipped with one detector module, which comprises 4 Cadmium Zinc Telluride (CZT) detectors. The NuSTAR data used in this thesis work are devoid of any pile-up issues thanks to using CZT detectors. NuSTAR has a spectral resolution of ~ 0.4keV at 10keV, angular resolution of ~ 58arcsec (HPD) and ~ 18arcsec FWH, temporal resolution of $\sim 2\mu$s.

We have used `nustardas` software, available as a part of `HEASOFT` (Nasa High Energy Astrophysics Science Archive Research Center (Heasarc), 2014) software package, along with NuSTAR calibration files for data reduction, calibration, screening and science-products extraction. The `nupipeline` tool is used to extract the cleaned event files from raw event files and `nuproducts` is used to extract final science data products. The default screening criteria for attitude, dead time, orbit and instrument parameters are used to obtain science data products, like the lightcurves, spectra and detector response files. For any specific details of data reduction, we have mentioned them in the relevant section of each chapter.

2.1.3 Swift-Neil Gehrels Observatory

The Swift - Neil Gehrels Observatory (Gehrels et al., 2004) is a multiwavelength mission (Figure 2.3) aimed at monitoring the sky in UV/optical, X-ray and Gamma-ray range. The observatory consists of the X-Ray Telescope (XRT, Burrows et al. (2005)), Burst Alert
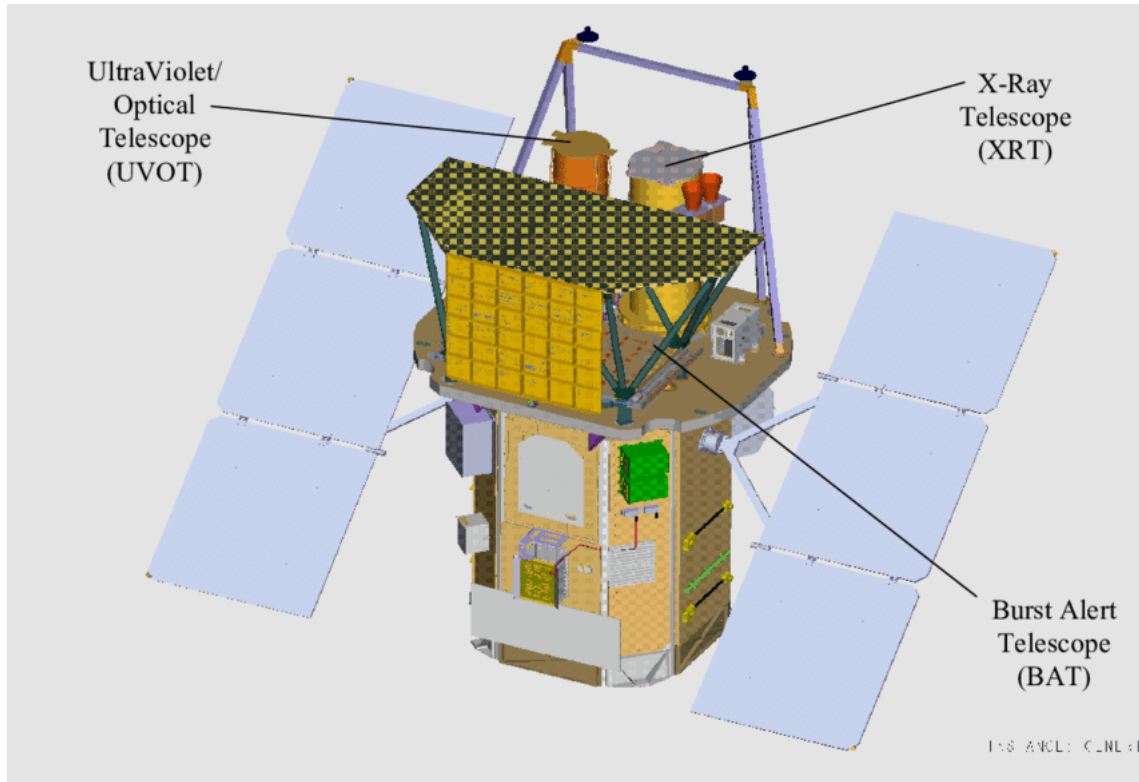
Figure 2.3: A schematic diagram of the Swift observatory.

Telescope (BAT, Barthelmy (2004)) and the Ultraviolet/Optical Telescope (UVOT, Roming et al. (2005)). The XRT is an imaging instrument capable of focusing X-rays in the energy range of 0.2-10 keV using a Wolter-I type telescope. This instrument has energy resolution of ∼ 140eV at 6keV, FOV ∼ 23.6 × 23.6arcmins^2, spatial resolution of ∼ 18arcsec HPD, ∼ 7arcsec FWHM , and temporal resolution ~0.14ms-2.5s (depending on the observation mode). The BAT instrument operates in 15-150 keV with a large FOV of 1.4 steradian and energy resolution of sim3.3 keV at 60 keV. It is primarily used for triggering alerts for high energy transient phenomenons, like GRBs. The UVOT instrument is similar to OM instrument of the XMM-Newton observatory, operating in a similar bandpass of 170-600nm.

To analyse the data from XRT, we have used `xrtpipeline` tool to extract the cleaned event files included in the `HEASOFT` software package. The `xselect` tool is then used to extract the image, lightcurves, and spectra files.The barycenter correction to the lightcurves are done using tool `barycorr`. The ARF files are generated using tool `xrtmkarf`, and the RMF files are available from the XRT calibration data. We have not used the BAT and UVOT data for this thesis work.

2.1.4   Suzaku

The Suzaku observatory (Mitsuda et al., 2007), which has recently been deactivated (in 2015), provided many extensive observations for CVs (Figure 2.4). This observatory
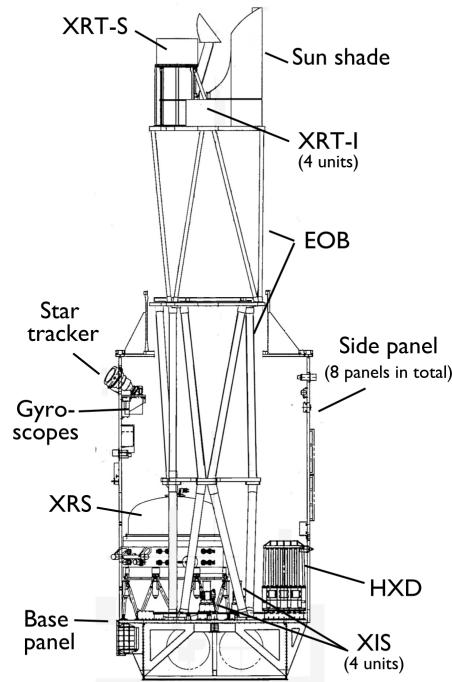
Figure 2.4: A schematic diagram of the Suzaku observatory (left).

has two main instruments on board: the X-ray Imaging Spectrometer (XIS, Serlemitsos et al. (2007); Koyama et al. (2007)), capable of focusing the X-rays in 0.2-12.0 keV using Wolter-I type X-ray telescope, and the Hard X-ray Detector (HXD, Takahashi et al. (2007)) which is a non-imaging instrument and operates in wide X-ray energy band 10-600 keV. Another calorimetric instrument (XRS, Kelley et al. (2007)) had an unfortunate fate and stopped working within weeks of the launch.

The XIS instrument has four detectors - XIS0, XIS1, XIS2 and XIS3. Among the four, XIS0, XIS2, and XIS3 employ front-illuminated CCDs, and XIS1 uses back-illuminated CCDs. The detector XIS2 stopped working after 2006. The operation energy range is 0.2-10.0 keV, with an energy resolution of ~ 130eV at ~ 6keV, effective area of $\sim 330 - 370\,\mathrm{cm}^2$ at 1.5 keV (and $\sim 110 - 160\,\mathrm{cm}^2$ at 8 keV), timing resolution of ~ 8s in normal mode, and a field of view of $\sim 17.8' \times 17.8'$. The HXD instrument comprises PIN diodes, operating in 10-70 keV, and Gadolinium oxyorthosilicate (GSO) scintillation counters, operating in 40-600 keV. The FWHM energy resolution of PIN and GSO are ~ 4keV and $\sim 7.6/\sqrt{E_{\mathrm{MeV}}}\%$ respectively. The effective area of the HXD instrument $\sim 160\,\mathrm{cm}^2$ at 20 keV and $\sim 260\,\mathrm{cm}^2$ at 100 keV.

For the analysis of the data from XIS, we utilized `aepipeline` tool to conduct data calibration and screening with default parameters on the raw data files and produced cleaned event files. Extracting light curves and spectra files was accomplished using the `xselect` tool. We generated instrument response files through the application of `xisrmfgen` and `xissimarfgen` tools. For the purpose of the thesis, we have not analysed HXD data.

While the data of a source from different instruments and observatories (XMM-Newton, NuSTAR, Swift, Suzaku), are analysed based on the above general techniques, specific details of the analysis from different instruments and observatories can somewhat vary depending on the source size, position on the chip, data mode, and count rate etc., which are covered in the corresponding chapters related to the sources.

2.2   Importance of Simultaneous Broadband Observation

To understand the accretion properties of CV sources, which are capable of producing X-rays in a few tens of eV to a few tens of keV, we need broadband coverage in the X-rays. However, no single observatory exists with an excellent sensitivity over this broad range for observing CVs. While few multiwavelength missions currently operating and having broadband X-ray coverage employing two instruments onboard, like Swift (XRT+BAT), Astrosat (SXT+LAXPC, Singh et al. (2014)) or lately inactive missions like Suzaku (XIS+HXD), the difficulties appear with the required sensitivity of the instruments for the CV observation, mostly in hard X-rays (beyond 10 keV). The issue with hard X-ray observation can now be solved with the operation of NuSTAR observatory (launched in 2013), which has an excellent effective area and sensitivity in the hard X-rays, suitable for the CV observation. Combining the observation from NuSTAR with observatories having good coverage in soft X-rays (like EPIC/XMM-Newton, XRT/Swift etc.) can provide a broadband X-ray coverage with excellent data quality for CV observation. In the Figure. effectivearea, we have compared the effective areas of different instruments (observatories), indicating the efficiency of the observations with energy. Nevertheless, one issue remains regarding the variability of CV sources. Cataclysmic sources are known for their variability, which can be periodic over a timescale of a few seconds to several days, or can have aperiodic variability. Observation taken with different observatories at different times can not be directly combined to obtain broadband coverage. To mitigate this issue, one direct way is to use the simultaneous observation employing two instruments covering the broadband range, giving the observer a broad X-ray window to investigate the accretion physics of the CV source. These observations are generally proposed by the observers beforehand so that they are performed simultaneously by two or more observatories. For this thesis work, we have used simultaneous broadband observations employing XMM-Newton+NuSTAR and Swift+NuSTAR, if available in the existing High Energy Astrophysics Science Archive Research Center (HEASARC) data archive [1], or from the data obtained as a part of proposed observation.

2.3   Data Analysis Techniques

This thesis has generally interpreted X-ray data with four types of analysis: imaging, timing, spectral, and polarisation. We have used the first three techniques to infer the data

---

[1] https://heasarc.gsfc.nasa.gov/docs/archive.html
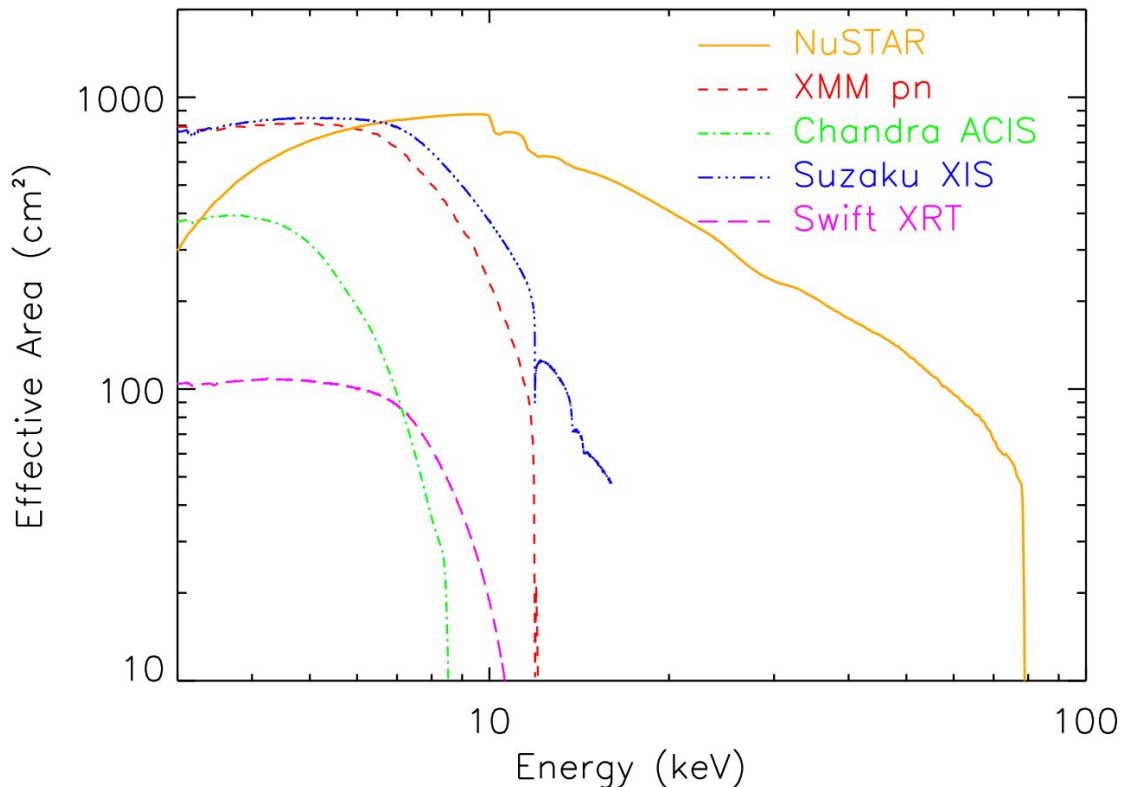
Figure 2.5: A comparison of the effective area from different observatories above 3 keV (left) (Harrison et al., 2013).

available to us. The first technique is the primary step for the analysis. We can localize the source to consider a source region suitable with the PSF of the imaging instrument and also select the background region. We have used tool DS9 (Joye & Mandel, 2003), for this purpose. The science products (lightcurves and spectra) are obtained for these regions using the tools. Specific details of the region's size and shape have been discussed in relevant sections of the subsequent chapters.

The primary focus of this thesis revolves around the timing and spectral analysis of the data obtained CV sources. We shall discuss a few aspects of these two techniques in the following subsections.

2.3.1   Timing Analysis Techniques

For the timing analysis, it is essential to obtain background-subtracted source lightcurves, for which we have generally used the `ftools` (Nasa High Energy Astrophysics Science Archive Research Center (Heasarc), 2014) task `lcmath` (other than for XMM-Newton data, where separate tools are already provided as part of SAS package, as mentioned in Sec. 2.1.1). For rebinning and plotting and some basic mathematical operations on the lightcurves (time vs count rate), we have used tool `lcurve`. The period search tool `efsearch` is used to search for periodic modulations in the lightcurves around a user-input guess period. The more elaborate method to investigate all the periodic signatures

in the lightcurve is extracting the frequency power spectra. The basic algorithm obtains the Fourier transform of the time series in the frequency domain. For a given sampling rate (Δt), the Nyquist frequency ($f_N = 1/2\Delta t$) governs the maximum frequency that can be detected in the power spectra. For certain frequency interval ($\Delta f \sim 1/4T$) considered, where T is the duration of the time series, the width of a period in the power spectra is $\sim P^2/\Delta f$. The astrophysical data often consist of in-between gaps. The Discrete Fourier Transform (DFT) technique is employed to execute the transformation from the time domain to the frequency domain. The classical DFT algorithm has a complexity of $\sim O(N^2)$, and is inefficient for large astrophysical data sets. While the Fast Fourier Transform (FFT) method (Cooley & Tukey, 1965) can be efficient (complexity $\sim O(N \log N)$) in handling large data sets with regular sampling, this method is inefficient in dealing with deal data with uneven sampling, a common nature of the astrophysical data. An advantageous algorithm to produce the frequency power spectra of large astrophysical data with gaps and irregular sampling is the Lomb and Scargle (L-S) algorithm (Lomb, 1976; Scargle, 1982), which utilises least-square fitting of the time-series data with sinusoidal of different frequencies and estimates the power associated. The computational complexity of the original L-S method, $O(NM)$, where N and M are the number of data points and the number of frequencies, is improved to $O(N \log M)$ by (Press & Rybicki, 1989). We have implemented this method using the `SCARGLE` task in `STARLINK` (Currie et al., 2014) software. We have also used the `CLEAN` algorithm (Roberts et al., 1987) to obtain the power spectra from the time series. The algorithm is useful of data with irregular gaps, a very common feature for the X-ray data with gaps due to SAA passage, earth occultation, or other issues. This algorithm deconvolves the effect of the window function from the DFT spectra and minimises the effect of spectral leakage arising from irregular data gaps. Two parameters are used in this algorithm - loop gain and the number of iterations. Typically, a value of 0.1 (Norton et al., 1992; Rana et al., 2004) is used for loop gain that removes a certain fraction (proportional to loop gain) of the window function with each iteration. The number of iterations is generally used between 100-10000, which decreases the noise present in the spectrum, with an accompanying cost of diminishing the power of actual peaks. We have finalised an optimal value of 1000 iterations for our periodogram after trying the other few orders (100 and 10000) of iterations.

2.3.2   Spectral Analysis Techniques

The primary tool for analyzing the X-ray spectra of the CVs is the X-ray spectral fitting package XSPEC (Arnaud, 1996). The photon counts ($C(I)$) that are captured by the instrument within the instrument channels (I) are expressed as follows:

$$C(I) = \int_0^\infty R(I, E)\, f(E)\, A(E)\, dE \tag{2.1}$$

where the spectrum ($f(E)$) denotes the photon flux density at energy E, and the

instrumental response $R(I, E)$ denotes the probability of observing photon with energy E in channel I, and $A(E)$ denotes the effective area of the instrument. Due to the non-invertible nature of the response matrix, finding $f(E)$ directly from $C(I)$ is not possible. Therefore, a model spectrum $f(E)$ is first chosen, and for each $f(E)$, the predicted count spectrum $C_p(I)$ from the model is compared with the observed spectrum $C(I)$, using a fit statistic. Typically, photon counts follow a Poisson distribution. The counts in several consecutive channels are binned together (typically 20-30 counts per bin) to make the distribution Gaussian by the principle of the central limit theorem. This exercise is useful because the widely used χ^2 statistic can be employed to obtain the best-fit results. The χ^2 fit statistic is defined as the following:

$$\chi^2 = \sum \frac{(C(I) - C_p(I))^2}{(\sigma(I))^2} \tag{2.2}$$

where $\sigma(I)$ is the error in channel I, the best fit is obtained by minimizing the χ^2 statistics. A reduced χ^2 (χ^2 divided by the degrees of freedom, ν) of 1 is a desirable fit statistic for a large value of ν. In cases where counts can not be rebinned to a Gaussian due to low count statistics, and we need to use the Poisson distribution, the Cash statistics (cstat; Cash (1979)) is used instead of χ^2. The error is estimated on each parameter by varying it in the range so that the χ^2 changes by 2.706 for 1 DOF, equivalent to the 90% confidence on that parameter.

The spectral models we have used in the thesis are part of the `xspec` software, and the models are described in the respective chapters as required.

A broadband X-ray study of the asynchronous polar: CD Ind

Abstract: *A simultaneous broadband analysis of X-ray data obtained with XMM-Newton and NuSTAR observatories for the asynchronous polar source CD Ind is presented. The spin folded lightcurve in soft 0.3-3.0 keV band shows single broad hump-like structure superimposed with occasional narrow dips, indicating a single-pole accretion model with a complex intrinsic absorber. Lack of strong modulation in folded lightcurve above 3 keV reveals that emission from corresponding zone of post-shock region (PSR) remains in view throughout the spin phase. The broadband spectrum is modelled with a three-component absorbed plasma emission model and absorbed isobaric cooling flow model, both of which fit the data well with similar statistical significance. Presence of partial covering absorber is evident in the spectra with equivalent column density $\sim 7 \times 10^{22}$ cm^{-2} and a covering fraction of $\sim 25\%$. Strong ionised oxygen K_α line emission is detected in the spectra. We notice spectral variability during spin phase 0.75-1.05, when there is a considerable increase in column density of overall absorber (from $\sim 1 \times 10^{20}$ cm^{-2} to $\sim 9 \times 10^{20}$ cm^{-2}). We required at least three plasma temperatures to describe the multi-temperature nature of the PSR. The shock temperature $\sim 43.3^{+3.8}_{-3.4}$ keV, represented by the upper temperature of the cooling flow model, implies a white dwarf mass of $\sim 0.87^{+0.04}_{-0.03}$ $M_\odot$. The iron K_α line complex shows a strong He-like and a weak neutral fluorescence line. We could not unambiguously detect the presence of Compton reflection in the spectra, which is probably very small and signifying a tall shock height.*

3.1   Introduction

Our target CD Ind (also known as EUVE J2115-586, RX J2115-5840) is one of the asynchronous polars (other notable few V1432 Aql, BY Cam and V1500 Cyg) which has been first identified as polars by Craig et al. (1996); Vennes et al. (1996) via spectroscopic studies and estimating the magnetic field strength. Schwope et al. (1997) updated the definition of CD Ind as an AP by intensive polarimetric study and signature of pole-switching was observed over a beat cycle. They also reported a magnetic field strength of 11 ± 2MG. Ramsay et al. (1999, 2000) stated that the acctreting material follows same set of field lines over the full beat cycle, i.e. the materials travel around the azimuth of WD to connect to those field lines over certain beat phases and argued about the complex magnetic field structure with non-dipolar field geometry of the WD, where one pole is sufficiently stronger than other. Ramsay et al. (2000) also performed X-ray analysis using RXTE PCA data, taken over several days of a beat cycle and found that the hard X-ray spectra in 4-15 keV produces similar spectral parameters for both the accreting poles, whichever is active for accretion at different beat phases. Involving a far ultraviolet spectroscopic study, Araujo-Betancor et al. (2005) reported a galactic column density of $1 \pm 0.5 \times 10^{19} \ cm^{-2}$ by measuring the absorption of a narrow interstellar Lyα line. Myers et al. (2017) revisited the source with extensive photometric campaign extended over a duration of 9 years and defined the spin and orbital periods along with the rate of change of spin period ($\dot{P}_\omega$). Later Littlefield et al. (2019) used continuous TESS photometric data of 28 days and redefined the Myer's identified period with $P_\Omega = 6720s$ and $P_\omega = 6648s$. They also claimed that $\dot{P}_\omega$ is half of what Myer's identified and updated the resynchronisation time scale ($\tau = |\frac{P_\omega - P\Omega}{\dot{P}_\omega}|$) to be 13000 years, making it one of the slowest achiever of synchronicity. Littlefield et al. (2019) reaffirmed that one accretion region is continuously visible during accretion over a spin phase, when the other pole undergoes self-eclipse and each pole accretes for nearly half of the beat cycle (~ 7.3 days). Using the TESS data, Hakala et al. (2019) studied the changes in accretion stream trajectory on to the two pole. The following year, also employing the TESS data, Mason et al. (2020) discussed the possible accretion scenario where four alternating and oppositely positioned accretion regions are present, with one accretion region being always in view. Sobolev et al. (2021) performed magnetohydrodynamic simulation of the flow structure under the assumption of shifted dipole configuration and predicted significant changes in flow structure depending on the pole-switching.

In this work, we present the study of the asynchronous polar source, CD Ind, for the first time, using the broadband X-ray data, obtained from XMM-Newton and NuSTAR telescope. We organise our paper as follows. In the next section (Sect. 3.2) we present the observations used and data reduction. Section 3.3 contains the results from the timing and spectral analysis of the source. In section 3.4 we discuss the results obtained from previous sections.

3.2   Observations and data reduction

CD Ind was observed simultaneously with XMM-Newton (Jansen et al., 2001) and NuSTAR telescopes (Harrison et al., 2013) as a part of our proposal to perform a detailed broadband X-ray spectral study of APs. The hard X-ray imaging telescope NuSTAR is capable of extending our understanding till 79 keV with high sensitivity. Simultaneous observation with XMM-Newton, having excellent energy resolution, empowers us to probe the soft energy part till 0.3 keV. So, the availability of simultaneous broadband data provides us the superior opportunity to characterise the spectrum by accounting the absorption in lower end as well as probing the reflection in upper end, thereby constraining the multi-temperature continuum from PSR. XMM-Newton telescope observed (Observation ID: 0870800101) the source for ∼ 36.8 ks on source time, starting at 2020-11-09 T12:32:16 and NuSTAR observed (Observation ID: 30601018002) for ∼ 56.5 ks, starting at 2020-11-09 T12:11:09. The high resolution reflection grating spectrometer, RGS (den Herder et al., 2001) on-board XMM, covering 0.35-2.5 keV energy band, can resolve the prominent emission lines present in the source.

3.2.1   NuSTAR

The two focusing imaging telescope modules of NuSTAR, namely FPMA and FPMB, can bring the hard X-rays (3.0-79.0 keV) to its focus and record with high sensitivity. We have selected a circular source region of 40 arcsec radius centering the source, and a circular source free region of 80 arcsec radius as the background from the same detector. We have used NuSTARDAS version 2.1.1 for data reduction. The latest calibration files are used (v20210701). `nupipeline` is used to obtain the cleaned event files using default screening criteria. The `nuproducts` command has been used to produce final science data products like lightcurve and spectrum files and necessary detector response files. We have performed the barycentric correction during product extraction. We have rebinned the NuSTAR spectra with minimum 25 counts in each bin using `grppha` to utilize the χ^2 minimization for spectral fitting.

3.2.2   XMM-Newton

XMM-Newton observation of the source was taken in large window mode using thin filter for both the PN (Strüder et al., 2001) and MOS detectors (Turner et al., 2001) of the European Photon Imaging Camera Instrument (EPIC). We have used XMMSAS v19.1.1 for the data reduction. The calibration files used, are obtained from SAS current calibration files repository, latest at the time of analysis [1]. We have followed the SAS analysis thread [2] for data reduction. We have used SAS tools `epproc` and `emproc` to produce calibrated event files. Our data are contaminated heavily by high background flair due to XMM-Newton's highly elongated eccentric orbit. The flaring is prominent during later part of

---

[1] https://www.cosmos.esa.int/web/xmm-newton/current-calibration-files
[2] https://www.cosmos.esa.int/web/xmm-newton/sas-threads

observation in PN and MOS data. To get rid of this flaring, we discarded the data using time selection criteria `TIME<721326500` in our good time interval (GTI). Unfortunately, this aggressive but essential filtering leaves us with only initial $\sim$ 11.2 ks and $\sim$ 13.1 ks of data from PN and MOS respectively. We have also checked for pile-up using `epatplot` tool but did not find any significant presence of it. The flaring free event files are then used for science products extraction with barycentric correction. We have chosen a circular source region with 25 arcsec radius centering the source, and a circular background region with 50 arcsec radius from the same CCD to extract our final lightcurve, spectrum and detector response files. The spectra have been rebinned with `spacegroup` tool to minimum 25 counts for using χ^2 statistic to test goodness of spectral fit.

For RGS data extraction we have used `rgsproc` tool. Though we found that RGS data are not contaminated to that hefty extent as that of EPIC, yet background flaring peaks are present, for which we have used rate selection criteria `RATE<=0.125` in the corresponding good time interval. We managed to get $\sim$ 30.9 ks of the exposure time for the spectra obtained from RGS detectors for our analysis. Spectra were rebinned with minimum 25 counts like before.

3.3 Data Analysis and Results

3.3.1 Timing Analysis

The data obtained from NuSTAR observation is $\sim$ 96 ks including the actual on-source time of $\sim$ 56.5 ks, gaps due to earth occultation and South Atlantic Anomaly (SAA) passage. These gaps result in difficulties to find the exact periods of the system with high precision and to distinguish between the spin ($6648s$) and orbital periods ($6720s$) which are closely spaced. However, given the total duration of NuSTAR data, we can get roughly $\sim$ 14 cycles to probe the timing properties of the system. On the other hand, flaring corrected EPIC data cover only $\lesssim$ 2 cycles. For spin and orbital period, we have followed Littlefield et al. (2019) who defined the periods based on nearly 28-days long continuous TESS data. The background subtracted cleaned lightcurves from both observatories have been plotted in the Figure 3.1.

We performed power spectral analysis on background subtracted PN and FPMA lightcurves that showed broad peaks at $6286 \pm 917s$ and $6545 \pm 111s$ respectively. These values agree with the literature values of rotational periods of the system, but our data could not resolve the spin and orbital periods.

Spin Folded Lightcurves

To fold the lightcurve based on the spin period, we have used the ephemeris $T(BJD) = 2458326.46492(17) + 0.0769522(11) \times E$ following Littlefield et al. (2019). They updated the derivative of spin period ($\dot{P} = +1.75 \times 10^{-10}$) from the value given by Myers et al. (2017) which was two times faster. The time when our observation was made (BJD=2459163.00774),
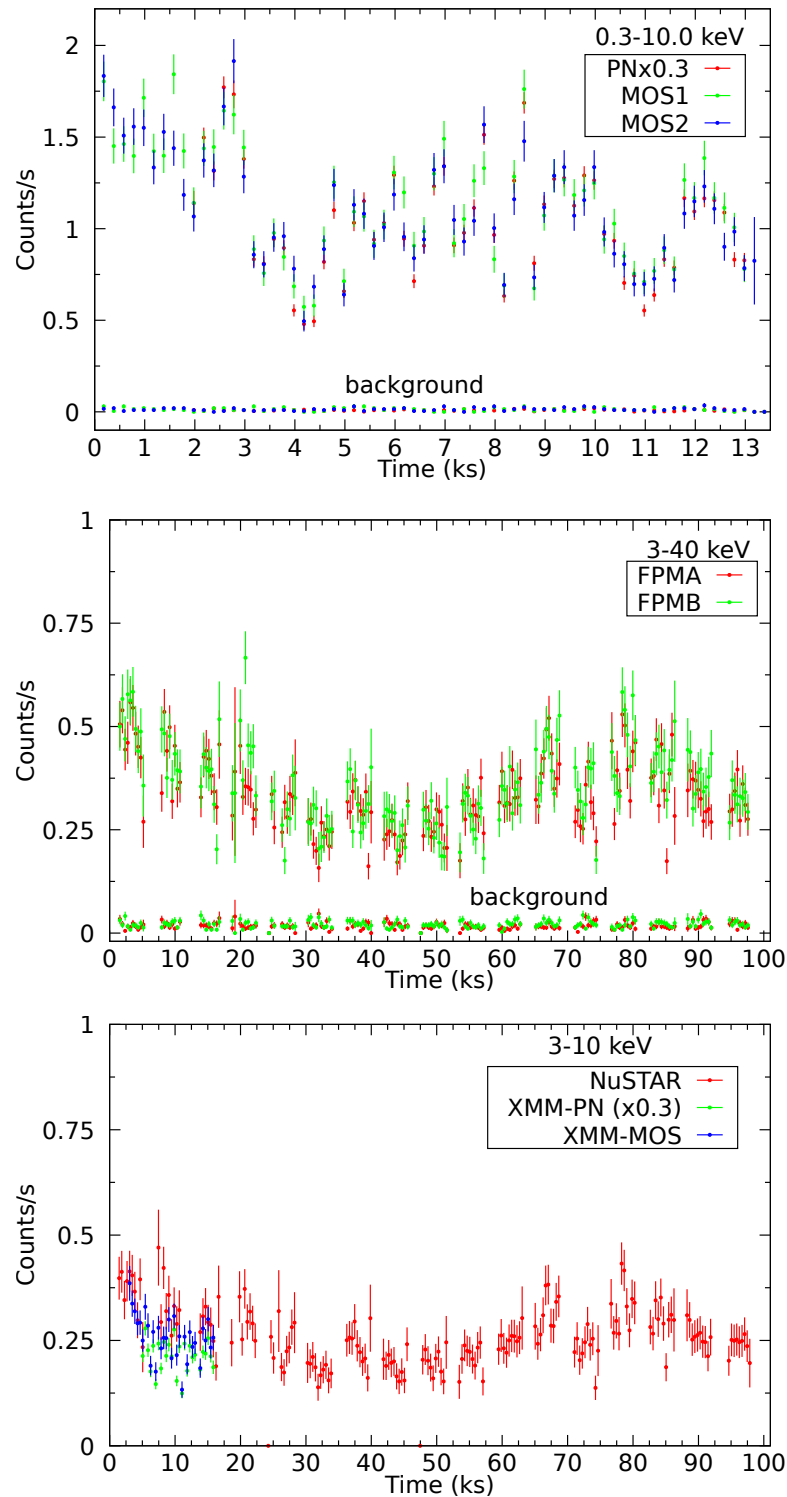
Figure 3.1: Background subtracted clean lightcurves from XMM-EPIC in 0.3-10.0 keV (top) and NuSTAR in 3-40 keV (middle) . Background lightcurves are also shown in those panels for reference. In the bottom panel, cleaned lightcurves are shown in the common 3-10 keV band where both telescopes have coverage. The lightcurves from both the modules of NuSTAR are co-added and averaged to improve statistics. Same is done for XMM-Newton EPIC-MOS. The start time is chosen to be NuSTAR observation start time. The PN counts/s is scaled by 0.3 in top and bottom panel for comparison. The bin size is 200s in top panel and 400s for middle and bottom panel.
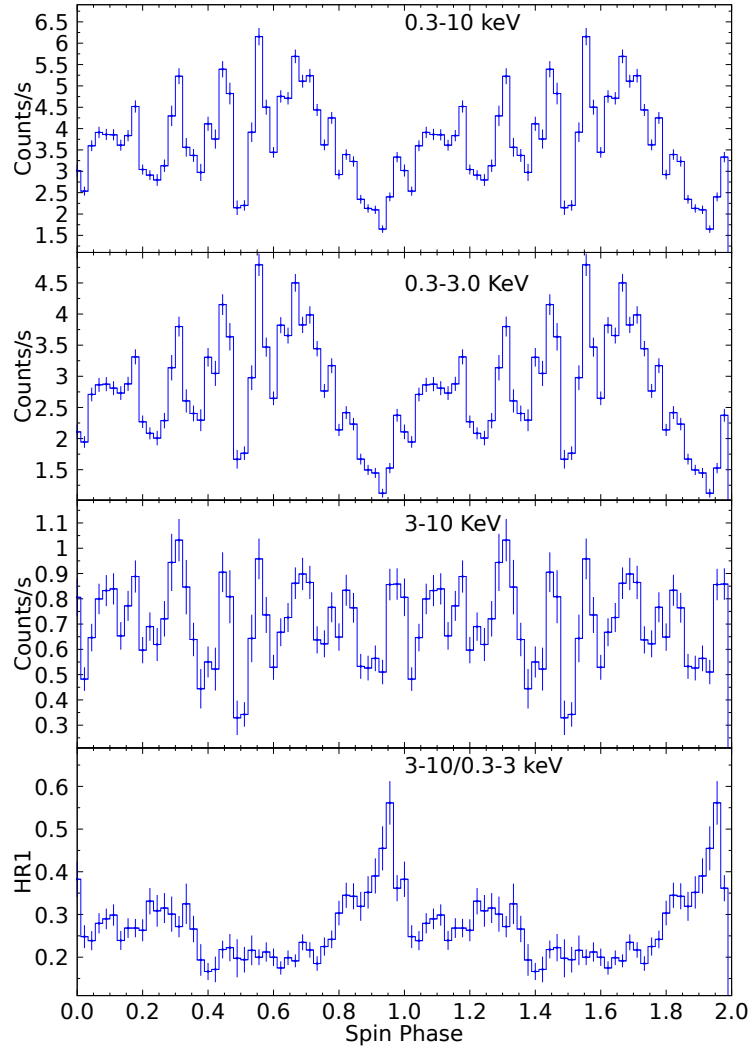
Figure 3.2: Spin folded lightcurves in different energy bands along with hardness ratio using XMM-EPIC PN data. Bin size in each panel is $\sim 150s$

the spin period has changed only by $\sim 0.0126s$ i.e $\sim 0.0002\%$ from the reported value in Littlefield et al. (2019).

We have shown the background subtracted spin folded XMM-Newton PN lightcurves in Fig. 3.2 for different energy bands (0.3-10 keV, 0.3-3.0 keV, 3.0-10.0 keV). The soft X-ray band (0.3-3.0 keV) exhibit a strong pulse fraction (PF) of modulation, $62 \pm 2\%$, using the definition $\text{PF} = (I_{max} - I_{min})/(I_{max} + I_{min})$ where I denotes the count rate. It shows a single broad hump like structure with occasional narrow dips in between. However, it is difficult to comment about all the dips individually due to the limitation of the data, which cover $\lesssim 2$ cycles. In 3-10 keV band of PN, the broad hump-like profile is not visible, and the count rate fluctuates around a mean value of 0.673 counts/s. The hardness ratio-1 plot ($HR1 = I_{3-10\,\text{keV}}/I_{0.3-3.0\,\text{keV}}$) in the bottom panel of Fig. 3.2 shows a strong peak in phase $0.75 - 1.05$, denoting a significant spectral variability during that phase.

Background subtracted spin folded NuSTAR lightcurves in different energy bands
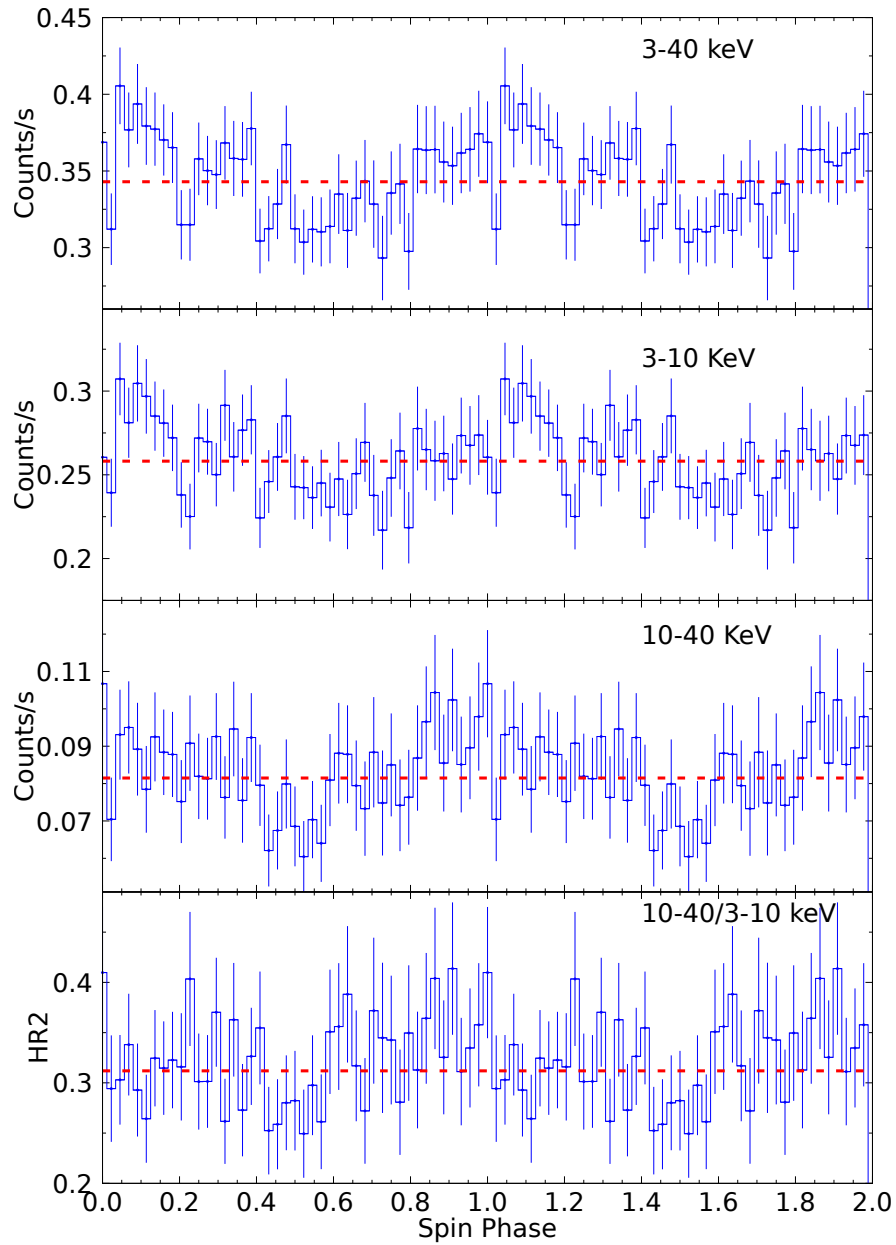
Figure 3.3: Spin folded lightcurves in different energy bands along with hardness ratio using co-added and averaged lightcurves from both the FPMA and FPMB modules of NuSTAR. Bin size in each panel is $\sim 150s$. The red dotted line represents mean counts rate by fitting a `constant` model

(3-40 keV, 3-10 keV, 10-40 keV) are plotted in Fig. 3.3. We have chosen 3-40 keV band from NuSTAR, since the background starts dominating beyond 40 keV. The folded lightcurve in 3-40 keV band in top panel of Figure 3.3 statistically represents a flattened profile with an average value ~ 0.343 counts/s. We observe a similar flattened profile with fluctuating count rates in both the constituent energy bands, 3-10 keV and 10-40 keV. For the profile in 3-10 keV and 10-40 keV band, a `constant` model can fit reasonably well with an amplitude of $\sim 0.258 \pm 0.004$ counts/s ($\chi^2_\nu(DOF) = 1.149(87)$) and 0.081 ± 0.002 counts/s ($\chi^2_\nu(DOF) = 0.873(87)$) respectively. Also, the hardness ratio-2 ($HR2 = I_{10-40\,keV}/I_{3.0-10.0\,keV}$) in the bottom panel of Figure 3.3, show a flat profile with an average value ~ 0.312, indicating there is no significant spectral variability above 3 keV over the full spin period.

The orbit folded lightcurves, using period 6720s (Littlefield et al., 2019), produce similar pattern in all energy bands as well as the hardness ratios, as observed in the spin folded lightcurves.

3.3.2 Spectral Analysis

We have used X-ray spectral fitting package, XSPEC (Arnaud, 1996) version 12.12.0, to analyse the spectra. The spectral models used in this paper are available in the package. The errors on the spectral parameter values are quoted with 90% confidence throughout the paper. Abundance table in our analysis was set after Wilms & McCray abundance table (Wilms et al., 2000) along with photoelectric absorption cross section defined after Verner et al. (1996)

Phenomenological fit to NuSTAR spectra

We have first utilised only the NuSTAR data for our phenomenological fit to get the idea about shock temperature and reflection amplitude. Both the FPMA and FPMB spectra (3.0-40.0 keV) were fitted simultaneously to improve the signal to noise ratio. The equivalent column density of galactic absorber (modelled after `tbabs`) was fixed at 10^{19} cm^{-2} (Araujo-Betancor et al., 2005) as NuSTAR data can not constrain it. Ionised plasma emission model `mekal` has been used for modelling the emission from the post-shock region. The switch parameter for the emission model was set at 2 to determine the spectrum based on updated line emission code `AtomDB v3.0.9` To incorporate the multi-temperature nature of the post-shock region of the accretion column, we have used two `mekal` components, where the upper temperature gives indication of the shock temperature. The iron line complex (neutral fluorescence at 6.4 keV, He-like at ~ 6.7keV and H-like at ~ 6.97keV) is not separately resolved by NuSTAR, and was modelled using a `gaussian` component. The combined model (including absorption, emission and gaussian) produced an upper temperature $30.7^{+19.7}_{-6.9}$ keV with a $\chi^2(DOF) = 411(459)$. Next we convolved the `reflect` model (Magdziarz & Zdziarski, 1995) with the emission components, to find out the effect of the Compton reflection which should manifest itself as an excess or hump in $\sim 10 - 30$ keV energy range. We have kept the parameters of

`reflect` other than reflection amplitude fixed at their default values (viewing angle set at $\mu = 0.45$, the abundance parameters were linked between reflection and emission component and were kept frozen at 1). The fit statistics didn't have any significant change ($\chi^2(DOF) = 409(458)$ i.e $\Delta\chi^2 \sim 2$ for 1 less DOF), indicating redundancy of `reflection` component in the fitting. However, NuSTAR-only fitting can not detect the lower temperature of the PSR, as well as presence of any extra absorber, which affects the soft X-rays, mostly below NuSTAR's coverage. So, we need to incorporate the simultaneous data obtained from XMM-Newton for a global description of the spectra.

Phenomenological fit to XMM-Newton spectra

To build up the description of the soft X-ray part of the spectrum, we have looked into the XMM-Newton EPIC (0.3-10.0 keV) and RGS (0.45-2.0 keV) data. Owing to good spectral resolution of the EPIC, we can distinguish the Fe K_α line complex. In order to quantify the contribution of those three lines, we have modelled them after three `gaussian` on top of a thermal `bremsstrahlung` continuum with fixed galactic absorption (10^{19} cm^{-2}) using 5.0-9.0 keV data. The resultant best fit parameters are quoted in Table 3.1 and corresponding spectral plot is shown in top panel of Fig. 3.4. The width (σ) of all the `gaussian` components are consistent with the EPIC resolution limit (~ 130 eV at 6.5 keV), hence fixed at zero, thus indicating that the lines are narrow. The line centers appear at expected energies within error bar. Fluorescent line is the weakest (equivalent width ~ 71 eV) whereas the He-like line is the strongest (equivalent width ~ 137 eV) among the three lines.

Next we have fitted the full EPIC spectra (PN, MOS1 and MOS2) in 0.3-10.0 keV to estimate the lower temperature and absorption parameters. A simple model like an absorbed single temperature ionised plasma emission (`mekal`) model with gaussian component for narrow 6.4 keV line produced a mediocre fit with $\chi^2(DOF) = 549(401)$ and a plasma temperature of $24.4^{+2.6}_{-2.4}$ keV. But the fit has issues like extremely low value of column density of the absorber ($\sim 10^{10}$ cm^{-2}) unbounded at lower limit and with upper limit reaching $\sim 2 \times 10^{19}$ cm^{-2} (close to the galactic n_H value of 10^{19} cm^{-2}), and the excess around 0.6 keV and 1 keV indicating line emissions like oxygen and iron-L shell from low temperature plasma. Fixing the n_H to 10^{19} cm^{-2} and adding one more plasma emission component resulted in a somewhat improved fit statistic ($\chi^2(DOF) = 527(400)$) with low temperature coming around $0.17^{+0.02}_{-0.03}$ keV representing an optically thin cold plasma. In order to evaluate the column density of any absorber present at the source, we included an photoelectric absorber model `phabs`, with $n_{H,tb}$ of galactic absorber `tbabs` fixed at 10^{19} cm^{-2} and found a better fit-stat ($\chi^2(DOF) = 518(399)$) with $n_{H,ph} = 1.18^{+0.69}_{-0.67} \times 10^{20}$ cm^{-2}. Guided by the presence of multiple narrow dips in our spin folded lightcurve, which possibly indicating presence of inhomogeneos absorber, we applied an extra partial covering absorber model, implemented by `partcov*phabs` on top of the overall absorption. This readily improved the fit to a significant amount

Table 3.1: Probing Fe-K$_\alpha$ lines (5.0-9.0 keV EPIC data)

Parameter	Unit	Value
$n_H^{\dagger\,a}$	$10^{19}\ cm^{-2}$	1_{fr}
$T_C^{\dagger\,b}$	keV	$32.8^{+67.8}_{-14.5}$
$N_C^{\dagger\,c}$	10^{-3}	$2.24^{+0.29}_{-0.08}$
$\text{LineE}_{\text{Neutral}}^{\dagger\,d}$	keV	$6.43^{+0.04}_{-0.03}$
$\sigma_{\text{Neutral}}^{\dagger\,e}$	eV	0_{fr}
$\text{eqw}_{\text{Neutral}}^{\dagger\,f}$	eV	71^{+37}_{-30}
$N_{\text{Neutral}}^{\dagger\,g}$	10^{-5}	$0.90^{+0.32}_{-0.32}$
$\text{LineE}_{\text{He-like}}^{\dagger\,d}$	keV	$6.70^{+0.02}_{-0.02}$
$\sigma_{\text{He-like}}^{\dagger\,e}$	eV	0_{fr}
$\text{eqw}_{\text{He-like}}^{\dagger\,f}$	eV	137^{+46}_{-43}
$N_{\text{He-like}}^{\dagger\,g}$	10^{-5}	$1.67^{+0.38}_{-0.37}$
$\text{LineE}_{\text{H-like}}^{\dagger\,d}$	keV	$6.97^{+0.04}_{-0.03}$
$\sigma_{\text{H-like}}^{\dagger\,e}$	eV	0_{fr}
$\text{eqw}_{\text{H-like}}^{\dagger\,f}$	eV	83^{+46}_{-33}
$N_{\text{H-like}}^{\dagger\,g}$	10^{-5}	$0.93^{+0.35}_{-0.35}$
$\chi^2(DOF)$		81.40(89)
χ^2_ν		0.9146

† a ISM column density

† b : Bremsstrahlung continuum temperature

† c : Normalisation of bremsstrahlung continuum

† d, e, f, g : Line energy, σ, equivalent width, and normalisation (in terms of photons cm^{-2} s^{-1}) of the corresponding Gaussian component respectively

* fr denotes the parameter is fixed.
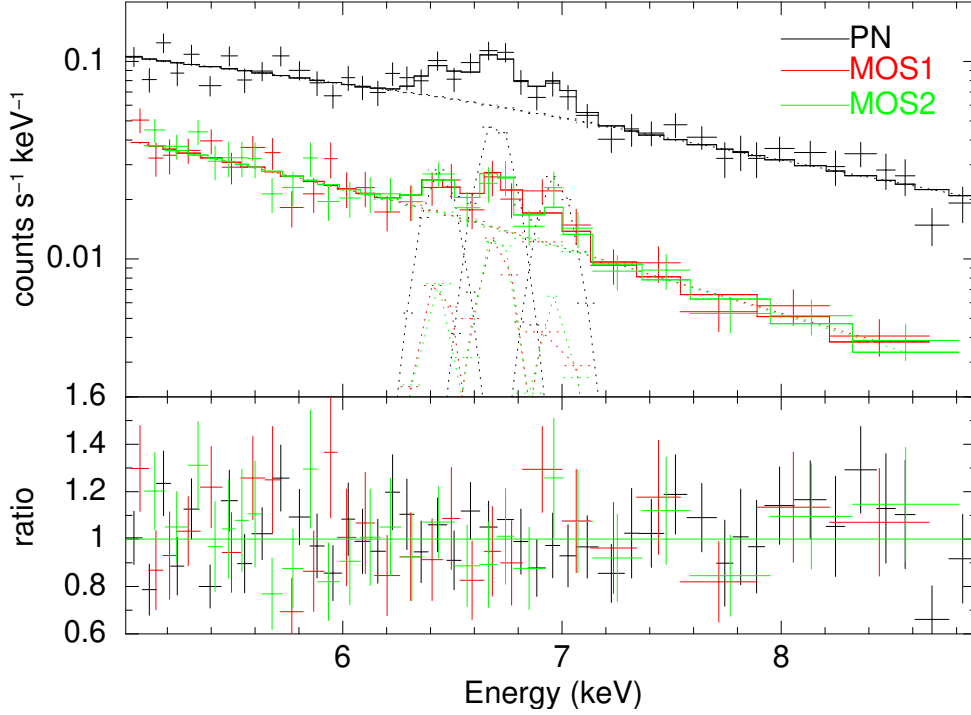
Figure 3.4: Modelling the iron K_α line complex using an absorbed bremsstrahlung continuum along with three gaussian component in 5-9 keV. The top panel shows the spectrum, and the bottom panel shows ratio (data/model) plot.

($\chi^2(DOF)$ = 464(397) i.e $\Delta\chi^2$ = 52 for 2 less DOF) with a column density of partial absorber, $n_{H,pcf}$ = $10.7^{+3.6}_{-2.5} \times 10^{22}$ cm^{-2} and a covering fraction of $0.27^{+0.07}_{-0.05}$. However, the model now define the lower energy part better, with the high temperature plasma emission component detecting a smaller value $10.5^{+3.6}_{-2.5}$ keV. The model underestimates the observed data in harder X-ray (beyond 7 keV), resulting in excess in residual. This motivated us to add one more plasma emission model, which produced an improved fit-staistic of $\chi^2(DOF)$ = 429(394) with maximum temperature of $36.2^{+32.9}_{-13.1}$ keV. F-test probability corresponding to the third `mekal` component is 8.75×10^{-7}, signifying its necessity. Though this temperature is not very well constrained due to absence of extended hard X-ray data for XMM Newton EPIC, yet clearly accounts for the excess residual beyond 7 keV, and is in agreement with the upper temperature we obtain from NuSTAR-only fit.

We have also looked into the grating spectrometer data, RGS in 0.45-2.0 keV band. We have used an absorbed thermal bremsstrahlung continuum model for fitting the data, with column density of absorber as a free quantity. The upper limit of the continuum temperature became unbounded, so kept fixed at fit value 4.95 keV. We see clear line emissions at ~ 0.57 keV and 0.65 keV, corresponding to the ionised oxygen K_α emission lines (O VII and O VIII respectively) in the spectra. We added two gaussian components to model those emission features. This produced a fit statistic of $\chi^2(DOF)$ = 161(163). The corresponding best fit parameter values are listed in Table 3.2 with the best fit spectrum
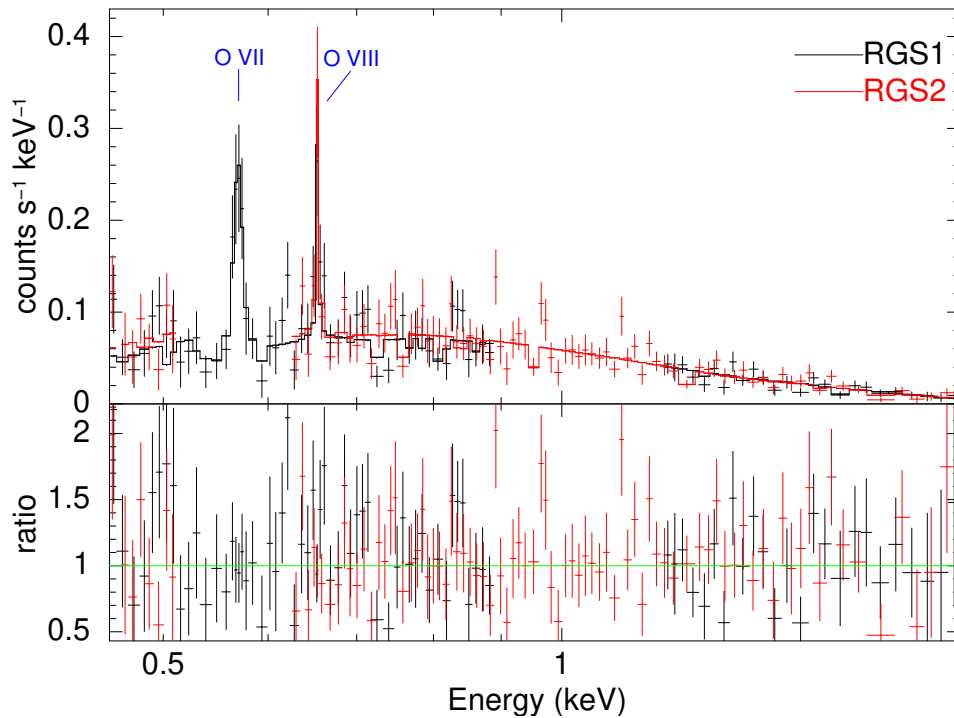
Figure 3.5: Modelling the ionised oxygen lines (O VII and O VIII) using an absorbed bremsstrahlung continuum along with two gaussian component in 0.45-2.0 keV. The top panel shows the spectrum, and the bottom panel shows ratio (data/model) plot.

plot in Fig 3.5. We noticed that the O VIII line is narrow, for which the width (σ) parameter couldn't be constrained and reaching value lower than instrument resolution, so we fixed it to 0. The width (σ) of O VII line was allowed to vary, however its best fit value reached almost the instrument resolution limit. The O VII line is composed of fine atomic transition lines (resonance, intercombination and forbidden lines), which are not resolved in the RGS spectra. The clear appearance of ionised oxygen K_α lines agrees with the presence of strong excess around 0.5-0.7 keV in EPIC spectra. Each of the gaussian components improve the fit w.r.t absorbed continuum by $\Delta\chi^2 \sim 31$ for 2 less DOF, indicating strong statistical significance of the two lines. The grating spectra doesn't show presence of other such strong lines, so modelling them using gaussian components are not statistically significant.

This phenomenological fit of XMM-Newton EPIC data now guides us to construct the final model in the next subsection for broadband spectral analysis of simultaneous data, obtained from both the observatories.

Broadband spectra fitting using XMM-Newton EPIC and NuSTAR

We have used the absorbed multi-temperature hot plasma emission model, as developed during phenomenological fits, for modelling the broadband data in 0.3-40.0 keV range. We used model `cons*tbabs*phabs*(partcov*phabs)* (mekal+mekal+mekal+gauss)` (model M1) to fit the broadband data, producing a resultant fit statistic $\chi^2(DOF) =$

Table 3.2: Best fit parameters from fitting oxygen K$_\alpha$ lines (0.45-2.0 keV RGS data)

Parameter	Unit	Value
$n_H^{\dagger\,a}$	$10^{20}\ cm^{-2}$	$4.68^{+1.97}_{-1.89}$
$T_C^{\dagger\,b}$	keV	4.95_{fr}
$N_C^{\dagger\,c}$	10^{-3}	$1.44^{+0.12}_{-0.12}$
LineE$^{\dagger\,d}_{\text{He-like}}$	keV	$0.569^{+0.002}_{-0.002}$
$\sigma^{\dagger\,e}_{\text{He-like}}$	eV	$3.9^{+1.7}_{-1.3}$
eqw$^{\dagger\,f}_{\text{He-like}}$	eV	42^{+15}_{-15}
$N^{\dagger\,g}_{\text{He-like}}$	10^{-5}	$10.28^{+4.39}_{-3.56}$
LineE$^{\dagger\,d}_{\text{H-like}}$	keV	$0.654^{+0.008}_{-0.001}$
$\sigma^{\dagger\,e}_{\text{H-like}}$	eV	0_{fr}
eqw$^{\dagger\,f}_{\text{H-like}}$	eV	17^{+5}_{-5}
$N^{\dagger\,g}_{\text{H-like}}$	10^{-5}	$3.51^{+1.34}_{-1.09}$
$\chi^2(DOF)$		161(163)
χ^2_ν		0.9877

† a : Overall column density

† b,c : Temperature and normalisation of bremsstrahlung continuum

† d,e,f,g : Line energy, σ, equivalent width, and normalisation (in terms of photons cm^{-2} s^{-1}) of the corresponding gaussian component respectively

* fr denotes the parameter is fixed.
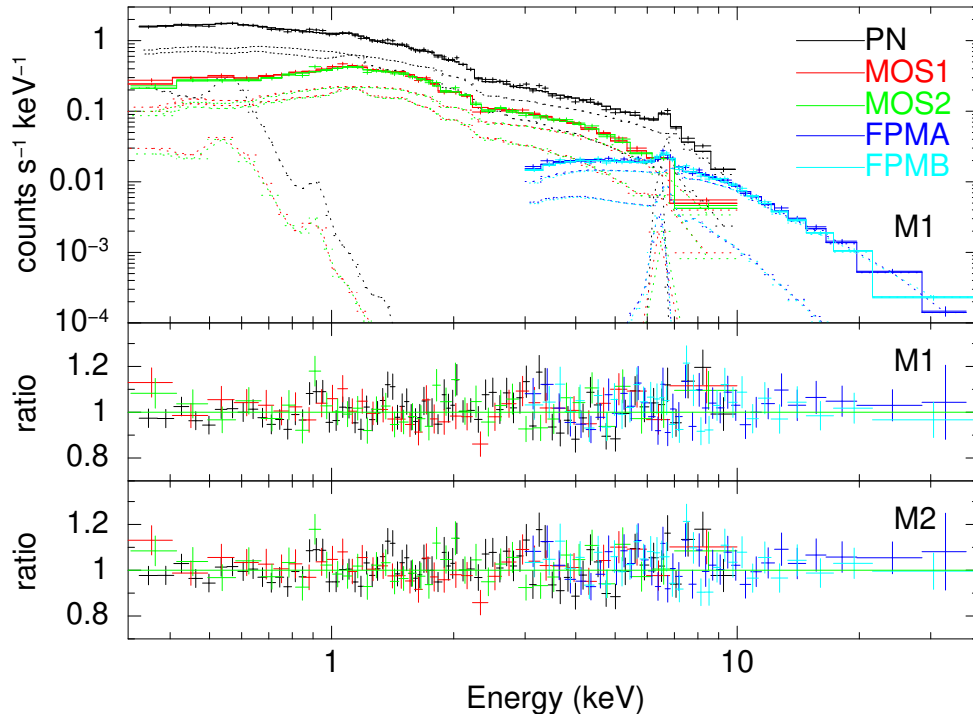
Figure 3.6: Best fit broadband spectra in 0.3-40 keV with model M1 is shown in top panel. The ratio (data/model) plot for spectral fitting with model M1 and M2 is shown in middle and bottom panel respectively

.

839(857). The best fit parameters are quoted in Table 3.3 with the spectra shown in Figure 3.6. The fit can describe spectra perfectly by incorporating a total and a partial covering absorber, signifying complex absorption and with clearly detected atleast three plasma temperatures. Best-fit parameters agree with phenomenological fits, but with better error constraints.

We have also tried adding one more plasma emission component (mekal), resulting in a marginal improvement of fit statistic ($\chi^2(DOF)$ = 835(855)). The corresponding F-statistic probability is 0.094. So, we didn't find a strong incentive to keep this extra fourth component.

At this stage our spectral modelling of broadband data constrains plasma emission parameters as well as column density parameters of absorption components. Next, in order to check the effect of Compton reflection, we have convolved the reflect model with the plasma emission components using the broadband data. The abundance parameters in mekal and reflect were linked and kept free. Similar to NuSTAR-only fit, there is no improvement to fit statistics with negligibly small reflection amplitude ($\sim 10^{-5}$).

To check the robustness of the parameters obtained from our simple yet effective three temperature plasma emission model (M1), we have also modelled our spectra using isobaric cooling flow model for ionised plasma, mkcflow (Mushotzky & Szymkowiak, 1988; Mukai et al., 2003). This model considers multi temperature nature of spectra by

using the emissivity function as inverse of bolometric luminosity. The redshift parameter of `mkcflow` was kept fixed at 5.53×10^{-8} according to the GAIA DR3 distance of 237 ± 4pc (Gaia Collaboration et al., 2021). The switch parameter was set at 2. We have used model `cons*tbabs*phabs*(partcov*phabs)* (mkcflow+mekal+gauss)` (model M2) for the broadband fit ($\chi^2(DOF) = 839(858)$) and best-fit parameters are quoted in Table 3.3 with ratio plot in Fig. 3.6. We noticed the absorption parameter values agree with model M1, thus independent of choice of the model. We required the extra optically thin plasma emission component to consider the excess around 0.6 keV. Fixing low temperature of cooling flow component at 0.0808 keV could not consider the excess around 0.6 keV and actually gave poorer fit statistic. So, we kept the lower temperature parameter of cooling flow component free, which detects some mean temperature near the base of the PSR where matter cools rapidly. The upper temperature is $43.3^{+3.8}_{-3.4}$ keV, which is relatively higher than model M1 ($26.3^{+5.3}_{-3.4}$ keV). Nevertheless, the fit statistics for both M1 and M2 models agree well. At this point, we included Compton reflection to test the necessity of it in our fit with M2 model, and observed similar findings as that of M1, signifying that reflection is not demanded by present data.

Phase-resolved spectroscopy

The HR1 (bottom panel of Fig. 3.2) shows excess during the spin phase $\sim 0.75 - 1.05$ indicating spectral variation. However, HR2 (bottom panel of Figure 3.3) doesn't indicate any such strong variation during the entire spin phase. The spin phase-resolved spectra in Figure 3.7, noticeably exhibit that the lower energy part of the spectra (below ~ 3 keV) is more absorbed during the phase 0.75-1.05 compared to phase 0.05-0.75, thereby explaining the excess in HR1 plot. To evaluate the spectral parameters, we have considered the broadband phase-resolved spectra in 0.3-40.0 keV range, and fit with the same models as phase-averaged spectra. The obtained best fit parameters are tabulated in the Table 3.3. Using the spectral model M1, the equivalent column density of overall photoelectric absorber comes out to be $8.78^{+2.96}_{-3.45} \times 10^{20}$ cm^{-2} during phase 0.75-1.05, much higher than $1.23^{+0.69}_{-0.68} \times 10^{20}$ cm^{-2} during phase 0.05-0.75. The best fit values of equivalent column density of partial covering absorber and covering fraction for the phase 0.05-0.75 are $11.2^{+4.7}_{-3.2} \times 10^{22}$ cm^{-2} and $0.23^{+0.05}_{-0.03}$ respectively. The same parameters for the phase 0.75-1.05 have values $5.3^{+2.9}_{-2.0} \times 10^{22}$ cm^{-2} and 0.33 ± 0.07 respectively. The above mentioned two parameters have slightly different best fit values but with overlapping error bars. Similar parameter values are obtained with model M2. The temperature of cold plasma emission component has an upper limit of ~ 0.1 keV in phase 0.75-1.05, but the lower limit is unconstrained (reaching the minimum temperature ~ 0.0808 keV, allowed by the model). This temperature could be mimicking the temperature near the bottom of the PSR. The upper temperature was getting poorly constrained in the phase 0.75-1.05, because of the reduced count statistics of NuSTAR data in that phase. So, we kept that temperature fixed at the corresponding value of best fit temperature obtained from phase-averaged spectra.

Table 3.3: Best-fit parameters obtained from fitting simultaneous broadband (0.3–40.0 keV) data

| Parameters | Unit | Spin-Phase-Averaged Spectra | | Spin-Phase-Resolved Spectra during Phase | | | |
| | | M1 | M2 | 0.05–0.75 | | 0.75–1.05 | |
				M1	M2	M1	M2
$n_{\mathrm{H,tb}}$	$\times10^{19}\ cm^{-2}$	1.0_{fr}	1.0_{fr}	1.0_{fr}	1.0_{fr}	1.0_{fr}	1.0_{fr}
$n_{\mathrm{H,ph}}$	$\times10^{20}\ cm^{-2}$	$1.84^{+0.99}_{-0.70}$	$1.80^{+0.84}_{-0.69}$	$1.23^{+0.69}_{-0.68}$	$1.37^{+0.60}_{-0.63}$	$8.78^{+2.96}_{-3.45}$	$9.74^{+2.61}_{-2.97}$
$n_{\mathrm{H,pcf}}$	$\times10^{22}\ cm^{-2}$	$7.44^{+2.39}_{-1.76}$	$6.84^{+2.21}_{-1.68}$	$11.22^{+4.72}_{-3.22}$	$9.60^{+3.95}_{-3.55}$	$5.26^{+2.95}_{-2.01}$	$6.68^{+3.48}_{-2.37}$
cvr frac		$0.25^{+0.04}_{-0.04}$	$0.26^{+0.04}_{-0.05}$	$0.23^{+0.05}_{-0.03}$	$0.26^{+0.03}_{-0.05}$	$0.33^{+0.07}_{-0.07}$	$0.32^{+0.06}_{-0.09}$
T_1	keV	$0.15^{+0.03}_{-0.04}$	$0.15^{+0.03}_{-0.04}$	$0.17^{+0.02}_{-0.03}$	$0.17^{+0.03}_{-0.05}$	<0.10	<0.10
T_2	keV	$4.9^{+1.1}_{-1.2}$	$1.9^{+0.6}_{-0.5}$	$4.4^{+1.4}_{-0.9}$	$1.5^{+0.6}_{-0.5}$	$4.0^{+1.1}_{-0.9}$	$2.3^{+2.9}_{-0.9}$
T_3	keV	$26.2^{+5.3}_{-3.4}$	$43.3^{+3.8}_{-3.4}$	$22.2^{+5.3}_{-3.1}$	$39.4^{+5.1}_{-3.3}$	26.2_{fr}	43.3_{fr}
Z	$Z_\odot$	$1.14^{+0.22}_{-0.19}$	$1.11^{+0.02}_{-0.02}$	$1.08^{+0.26}_{-0.20}$	$0.98^{+0.19}_{-0.19}$	$1.03^{+0.43}_{-0.35}$	$0.82^{+0.33}_{-0.29}$
LineE	keV	$6.43^{+0.03}_{-0.03}$	$6.44^{+0.03}_{-0.03}$	$6.44^{+0.03}_{-0.08}$	$6.44^{+0.05}_{-0.04}$	$6.46^{+0.07}_{-0.06}$	$6.48^{+0.08}_{-0.06}$
σ	eV	0_{fr}	0_{fr}	0_{fr}	0_{fr}	0_{fr}	0_{fr}
N_L	$\times10^{-5}$	$0.95^{+0.29}_{-0.25}$	$1.04^{+0.26}_{-0.22}$	$0.85^{+0.30}_{-0.34}$	$0.88^{+0.32}_{-0.28}$	$1.19^{+0.51}_{-0.52}$	$1.18^{+0.50}_{-0.50}$
χ^2(DOF)		839(857)	839(858)	694(752)	688(753)	429(427)	438(428)
χ^2_ν		0.9790	0.9778	0.9229	0.9137	1.005	1.023

Model **M1**: constant*tbabs*phabs*(partcov*phabs) *(mekal+mekal+mekal+gauss)
Model **M2**: constant*tbabs*phabs*(partcov*phabs) *(mkcflow+mekal+gauss)
For model **M1**: T_1, T_2, T_3 denotes temperature of the three plasma emission components (mekal)
For model **M2**: T_1 denotes temperature of single temperature plasma emission mekal component; T_2, T_3 denotes upper and lower temperature of cooling flow component mkcflow
$n_{\mathrm{H,tb}}$, $n_{\mathrm{H,ph}}$, $n_{\mathrm{H,pcf}}$ denotes equivalent column density of the ISM, overall absorber and the partial covering absorber respectively. "cvr frac" stands for the covering fraction of the partial covering absorber.
Z denotes the overall abundance
LineE, σ, N_L represents line energy, σ and normalisation (in terms of photons $cm^{-2}\ s^{-1}$) of the gaussian component for neutral Fe Kα line.
fr denotes the parameter is fixed.
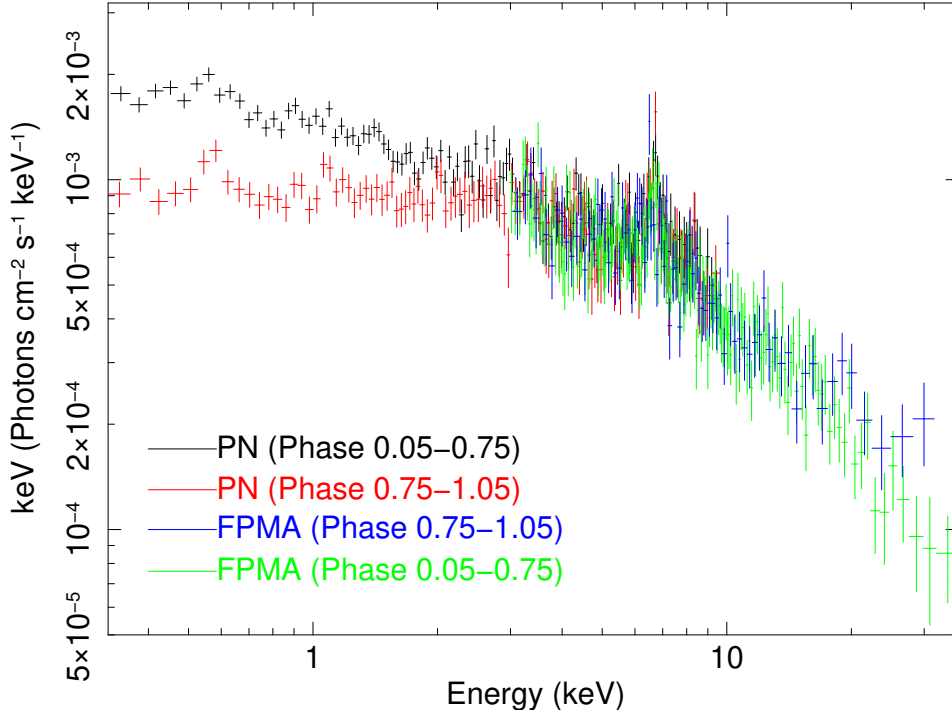
Figure 3.7: Comparison of phase-resolved spectra in 0.05-0.75 and 0.75-1.05 spin phase. An increased absorption below 3 keV is prominent for spin phase 0.75-1.05.

3.4 Discussion

We have carried out the broadband X-ray timing and spectral analysis of the asynchronous polar CD Ind. The implication of the timing and spectral results are discussed in this section.

3.4.1 Spin modulations in folded lightcurves

The spin folded lightcurve in 0.3-3.0 keV band (Fig 3.2) shows strong pulse profile with a single broad hump with multiple narrow dips and a pulse fraction of $62 \pm 2\%$. The single broad hump picture nicely fits into the earlier reporting of one pole accretion at any specific beat phase (Littlefield et al., 2019; Myers et al., 2017; Ramsay et al., 2000). The dips represent the scenario where the X-ray emission passes through the inhomogeneous and complex accretion stream, undergoing photoelectric absorption. The minima at phase ~ 0.94 can be envisaged as when the corresponding emitting region is moving away from the line of sight and the emission is reaching us after passing through the intrinsic absorber. The broad hump like structure is missing in 3.0-10.0 keV band of PN, but the features of absorption dips are present (Fig 3.2). It indicates the corresponding X-ray emitting region of the PSR remains visible during the entire spin cycle, but still passes through the inhomogeneous accretion stream. Also, the spin folded NuSTAR lightcurve in the 3.0-10.0 keV band, as well as 10-40 keV band (Fig 3.3) lack strong modulation. The lack of strong modulation in hard X-rays suggests corresponding zones of the PSR remain

in the view throughout the spin phase. This scenario is representative of a tall PSR and a small angle between spin axis and magnetic axis (eg. ~ 10°, Ramsay et al. (2000)).

3.4.2 Multi-temperature nature of the accretion column

Our spectral analysis of the spin-average broadband spectra reveals the multi-temperature nature of the post-shock plasma. It is represented by three plasma temperatures in our spectral modelling. The upper temperature is close to the shock temperature. The lower temperature, coming from the optically thin cold plasma, indicates the scenario near the bottom of the PSR. The middle-temperature plasma designates the cumulative contribution from remaining temperature zones of the PSR. It is to be mentioned that in Aizu model, PSR consists of multiple temperature zones with gradually decreasing temperature with most of cooling occurring near bottom of the PSR (Fig. 2 of Mukai (2017)), and there is no distinct division among them. Our three-component plasma emission model is a simple yet useful picture to represent the PSR, with averaged contribution of plasma emissivity from different zones. A more extensive approach to represent the multi-temperature nature of PSR is by cooling flow models (Mukai et al., 2003). However, the lower temperature of cooling flow model in our fit does not necessarily indicate the lowest temperature at bottom of the PSR and possibly detects some mean value of temperature near the base of the PSR where the plasma is rapidly cooling. The requirement of an additional optically thin plasma to incorporate the excess due to emission features present in soft X-ray is also evident in cooling flow model.

The importance of having highly sensitive spectral data in hard X-rays is to measure the shock temperature accurately, thereby constraining the mass of the WD. The upper temperature of the cooling flow model represents the shock temperature more accurately than the three-component plasma emission model. This is because, cooling flow model considers the temperature gradient of the PSR using multiple grid points according to emissivity function of the emitting plasma, whereas the three-component plasma emission model represents the whole PSR using three plasma temperatures. Thus the upper temperature for three component plasma emission model is more likely to be an average value of temperature profile from the region below the shock. Using the relation between the shock temperature, mass and radius of the WD (Mukai, 2017), and incorporating the WD mass-radius relation (Nauenberg, 1972), we quote a mass value $M_{WD} = 0.87^{+0.04}_{-0.03} M_{\odot}$ for a shock temperature of $43.3^{+3.8}_{-3.4}$ keV (obtained from model M2, see Table 3.3). The corresponding radius is $R_{WD} = 6.42^{+0.27}_{-0.28} \times 10^8$ cm (~ 0.009 $R_{\odot}$). Ramsay et al. (2000) measured a WD mass of $M_{WD} = 0.79^{+0.12}_{-0.11} M_{\odot}$ using RXTE PCA spectra in 4-15 keV. Our measured mass, obtained using broadband spectra, matches with them, but with better error constraint.

The line of sight orbital velocity of the WD comes out to be ~ 90 km/s, calculated using the following parameters: the mass of WD (obtained in this work ~ 0.87$M_{\odot}$), mass of M6V secondary (Littlefield et al. (2019), typical mass ~ 0.21$M_{\odot}$), binary period ~ 6720

s (Littlefield et al., 2019), and inclination angle of $\sim 65°$ (Mason et al., 2020).

We obtain an unabsorbed bolometric (0.3-40.0 keV) flux of $22.2^{+0.4}_{-0.4} \times 10^{-12}$ erg cm^{-2} s^{-1} of which $\sim 64\%$ is contributed from 0.3-10.0 keV band and the remaining is from 10-40 keV band. The corresponding luminosity from the source is $L = 1.49^{+0.08}_{-0.07} \times 10^{32}$ erg s^{-1} (using $L = 4\pi F d^2$ where d is the distance to the source $\sim 237 \pm 4$ pc (Gaia Collaboration et al., 2021)).

The relation between accretion luminosity (L_{acc}), mass, radius and mass accretion rate of the WD (M_{WD}, R_{WD} and $\dot{M}$ respectively) is given by (Frank et al., 2002),

$$L_{acc} = \frac{GM_{WD}\dot{M}}{R_{WD}}$$

Assuming accretion luminosity is mostly emitted in X-rays, we calculate a mass accretion rate of $\dot{M} \sim 8.24 \times 10^{14}$ g s^{-1} $\sim 1.30 \times 10^{-11}$ $M_\odot$ yr^{-1} using our obtained values of mass, radius and luminosity.

3.4.3 Iron and Oxygen K$_\alpha$ line emissions

The asynchronous polar CD Ind showed strong Fe K$_\alpha$ line emission, and XMM-Newton could resolve the three lines i.e. fluorescence, He-like and H-like lines. The line diagnostic shows that all the three Fe K$_\alpha$ lines in CD Ind have central energies at their expected positions within 90% confidence level, and the lines are narrow, which is expected from the radial velocity of the emitting pole of the WD. The intensity and equivalent width of the He-like Fe line are the strongest among the three lines. On the other hand, the neutral Fe K$_\alpha$ line is weakest among all, carrying an equivalent width of 71^{+37}_{-30} eV.

According to Ezuka & Ishida (1999), the observed equivalent width of the neutral Fe-line could be a sum of contribution from various components, like absorbing material and the cold surface of the WD. However, within the current limitation of the data, it is not possible to distinguish between these contributions, therefore we observe a total equivalent width. The Compton reflection is also originated from the similar region of the WD when the hard X-ray emission hits cold material at surface (van Teeseling et al., 1996). Our data could not unambiguously detect the presence of reflection, which might be very small in the spectra. If the shock height is very large, the emitted hard X-rays can subtend only a very small solid angle to the WD surface, thereby producing a negligible reflection.

In addition to the Fe K$_\alpha$ line in EPIC spectra, the RGS grating spectra show presence of strong ionised oxygen K$_\alpha$ lines, appearing with equivalent width of 42 ± 15 eV (O VII) and 17 ± 5 eV (O VIII). These lines come from the cooler bottom region of the PSR. Presence of these lines with such strength indicates that the bottom temperature of the PSR is low enough to produce them. This fits with our prediction about tall shock height in CD Ind, so that the PSR gets sufficient time to cool down while reaching WD photosphere.

Previous study of CD Ind from XMM-Newton also reported presence of a strong Ni K_α line at 7.4 keV (Joshi & Pandey, 2019). However, we did not find any such emission feature in our XMM-Newton data.

3.4.4   Excess absorption during spin phase 0.75-1.05

Our phase-resolved spectroscopy of CD Ind clearly identified the increased absorption in the soft X-rays below 3 keV during 0.75-1.05 spin phase as indicated by the HR1 of spin folded lightcurves. The column density of overall photoelectric absorption, which affects the low energy part increased by almost an order of magnitude. The partial covering absorber, however, did not change significantly. Due to more absorption, the absorbed flux value obtained in 0.3-3.0 keV band during phase 0.75-1.05 ($3.89^{+0.15}_{-0.18} \times 10^{-12}$ erg cm^{-2} s^{-1}) is less than the flux in same band during phase 0.05-0.75 ($5.50^{+0.06}_{-0.09} \times 10^{-12}$ erg cm^{-2} s^{-1}). The absorbed flux values in 3-40 keV band during both phases remained similar.

Study of complex absorption and reflection in a unique intermediate polar Paloma

Abstract: *We present the broadband (0.3-40.0 keV) X-ray analysis of a unique intermediate polar Paloma using simultaneous data from XMM-Newton and NuSTAR observatories. The X-ray power spectra show strong modulations over orbital period compared to spin period. The orbit folded lightcurves show single broad hump like structure with strong dips for soft to medium X-rays (0.3-10.0 keV). The energy dependent dips at $\phi \sim 0.16$ and 0.5 arise due to complex intrinsic absorber, strong enough to have effect well around 15 keV. The absorber could potentially be contributed from accretion curtain/ accretion stream and absorbing material produced by stream-disc/stream-magnetosphere interactions. We notice significant variation of the absorber with orbital phase, with maximum absorption during orbital phase 0.1-0.22. The absorber requires more than one partial covering absorber component, specifying the necessity to use distribution of column densities for spectral modelling of the source. Isobaric cooling flow component is utilized to model the emission from the multi-temperature post-shock region, giving shock temperature of $31.7^{+3.3}_{-3.5}$keV, which corresponds to white dwarf mass of $0.74^{+0.04}_{-0.05}$ $M_\odot$. We have used both the neutral absorber and the warm absorber models, which statistically give similarly good fit, but with different physical implications. Among the Fe K_α line complex, the neutral line is the weakest. We probed the Compton reflection, and found minimal statistical contribution in the spectral fitting, suggesting presence of weak reflection in Paloma.*

4.1 Introduction

The source Paloma (RX J0524+42, 1RXS J052430.2+424449) is a special IP in which the asynchronism is much less (~ 14%) compared to other IPs (typically ~ 90%). Schwarz et al. (2007) has studied the source using optical photometry on multiple nights, extended over a duration of several years and ROSAT X-ray observation. They detected three strong periodic signatures in the optical lightcurve and commented about two possible values of the spin period. Recently, Littlefield et al. (2022) specified one of the two values of Schwarz et al. (2007) for the spin period of the WD using nearly a month long TESS observation. This source was studied by Joshi et al. (2016) in the soft to medium X-rays (0.3-10 keV) using XMM-Newton. Their spectral modelling hinted at the presence of strong reflection amplitude. Paloma is yet to receive its proper classification among mCVs. Here we should note that rate of change of spin period ($\dot{P}$) is not yet determined for Paloma. Given the asynchronosity which is much lower than conventional IPs and slightly higher than traditional asynchronous polars (APs) (~ $1 - 2\%$ eg. V1432 Aql, CD Ind, BY Cam, V1500 CYg) for which $\dot{P}$ is measured, it is hard to distinctly classify Paloma as IP or AP. Schwarz et al. (2007); Joshi et al. (2016) described Paloma as IP whereas Littlefield et al. (2022) considered it as AP.

Using the broadband X-ray data, simultaneously obtained from XMM-Newton and NuSTAR, we tried to give an overall description of the spectral properties of the system, along with the temporal behavior of the system extending all the way up to 40 keV. The strong reflection amplitude should manifest a reflection hump in the 10-30 keV which we could not unambiguously detect in the NuSTAR spectra. We argued for an alternative picture to the strong reflection hypothesis, using a complicated absorber model for the source. We also probed for X-ray periodicity in the power spectra. In the following section we describe the reduction of the obtained data. In Sec. 4.3, we present our results based on the timing and the spectral analysis of the broadband X-ray data. In the next section (Sec. 4.4) we discuss our results.

4.2 Observation and Data reduction

Paloma was observed simultaneously by the XMM-Newton (Jansen et al., 2001) and NuSTAR (Harrison et al., 2013) observatories. XMM-Newton can observe the source in 0.3-10.0 keV band with good spectral resolution whereas NuSTAR is capable of imaging the source in 3.0-78.0 keV band with high sensitivity in the hard X-rays. Thereby simultaneous observation by these two observatories provides us broadband data in 0.3-78.0 keV. This enables us to probe the properties of the source in the soft X-rays like constraining the absorption parameters as well as detecting the shock temperature and Compton reflection in the hard X-rays.

NuSTAR observed (Obs ID 30601019002) the source on UTC 2021-03-02 01:10:08. The focal plane modules (FPMA and FPMB) recorded the source for an exposure time of ~

47ks. We have selected a source region using a circle of radius 40 arcsec and a background region of radius 80 arcsec in the same detector as that of the source. We used NUPIPELINE to extract the cleaned events files with default screening criteria and then NUPRODUCTS to obtain the final science products like lightcurves and the spectra along with detector response files. We performed barycenter correction while deriving the science products. The timebin size of the extracted lightcurves are chosen to be 1s. We have grouped the spectra for a minimum counts of 25 per bin to use χ^2 statistics to test goodness-of-fit.

The XMM-Newton observation (Obs ID 0870800201) was taken on UTC 2021-03-02 01:06:28 for a duration of $\sim$ 33ks. The observation was carried in full window mode using medium filter for both of the PN (Strüder et al., 2001) and MOS Turner et al. (2001) cameras of European Photon Imaging Camera (EPIC) instruments. We have selected a circular source region of radius 25 arcsec and a circular background region of radius 50 arcsec in the same detector as that of the source. We used XMMSAS v19.1.0 (Gabriel et al., 2004) for data reduction and extraction of the lightcurves and the spectra following the SAS analysis thread [1]. The calibration files are used from the current calibration file (CCF) repository [2] of XMM-Newton, latest during the analysis. The XMM data is contaminated with background flaring in the initial part of the observation, so we discarded first few ks of data which neatly eliminate the flaring part and leaves us with nearly $\sim$ 29ks of continuous data from all the EPIC cameras. Using SAS tool EPATPLOT, we have also checked for pile up in the data, and did not find any significant contribution of it. The products have been barycenter corrected. We chose the 1s binning for the extracted lightcurves. The SAS tool SPECGROUP is used to group the data with minimum counts per bin at least 25 for using the χ^2 statistics. The oversample parameter is set at 3 so that minimum group width is not less than 1/3rd of the FWHM of the instrument resolution at that energy.

We have also extracted the spectrum from reflection grating spectrometer (RGS) on board XMM-NEWTON. We have used RGSPROC tool and eliminated the background flaring to obtain the grating spectra. The spectra are also grouped to 25 minimum counts per bin to use χ^2 statistics.

4.3 Data Analysis and Results

4.3.1 Timing Analysis

We have the continuous data from XMM-Newton for $\sim$ 29ks and a total duration of $\sim$ 96 ks data from NuSTAR including the gaps due to earth occultation and South Atlantic Anomaly (SAA). The duration of XMM-Newton and NuSTAR observation give us the opportunity to study the timing properties of the source for $\sim$ 3 cycles and 10 cycles respectively. We have shown the background subtracted lightcurves from XMM-Newton

---

[1]https://www.cosmos.esa.int/web/xmm-newton/sas-threads
[2]https://www.cosmos.esa.int/web/xmm-newton/current-calibration-files

and NuSTAR in the top and middle panels of Fig. 4.1. In the bottom panel of Fig 4.1, the lightcurves in the 3-10 keV band from both the observatories are overplotted. In this section, we have calculated the power spectra for the source, and subsequently folded the lightcurves based on the orbital period of the system. We have presented the results from NuSTAR-FPMA and XMM Newton EPIC-PN in the following subsections; as the results from FPMB for NuSTAR and MOS1 & MOS2 for XMM Newton EPIC are also similar.

Power Spectra

We have implemented two methods to search for the periods - Lomb-Scargle method (Lomb, 1976; Scargle, 1982) and the CLEAN algorithm (Roberts et al., 1987). The first one is widely used to find the frequencies present in a unevenly sampled time series. The later one uses the algorithm to deconvolve the effect of window function from the discrete Fourier transform (DFT) spectra and thereby minimise the effect of spectral leakage. This method has been used efficiently for other IP sources with unevenly sampled data (Norton et al., 1992, 1997).

In the NuSTAR-FPMA power spectra using Lomb-Scargle method (top panel of Fig. 4.2), we can clearly identify the peak at orbital frequency Ω, corresponding to a period value 9384 ± 229s, present in all the energy bands (3-40 keV, 3-10 keV, and 10-40 keV). We notice that the peaks are stronger in 3-10 keV band compared to 10-40 keV band. This period is also identified by Schwarz et al. (2007) at ∼ 9430.35s in their optical photometric campaign and Thorstensen et al. (2017) at ∼ 9434.88s using radial velocity spectroscopy. We see the spin frequency peak ω, corresponding to a period value 8365 ± 181s, immediately next to the orbital frequency in the Lomb-Scargle power spectra. This value agrees with one of the spin period candidate (∼ 8175.37s) by Schwarz et al. (2007) , and spin period (∼ 8229s) detected by Littlefield et al. (2022). We notice another weak peak at $2\omega - \Omega$, with a period value of 7545 ± 148s. In the FPMA power spectra, these two peaks ($\omega, 2\omega - \Omega$) appear with a much lower power compared to the Ω. Joshi et al. (2016) obtained two low power peaks for ω and $2\omega - \Omega$ adjacent to the strongest peak at orbital period in their power spectra, obtained using previous XMM-Newton observation, but with smaller period values (7800s and 6660s respectively) than ours. In Fig. 4.2 we have also marked the expected positions of several harmonics and sideband frequencies. We notice a relatively strong peak (2850 ± 21s) near $\Omega + 2\omega$ (expected at 2893 ± 48s). We also observe peaks at 4474 ± 52s and 4183 ± 46s which respectively agree with $\Omega + \omega$ (expected at 4423 ± 72) and 2ω (expected at 4182 ± 90s) within error-bar. It is to be pointed here that, the resolution of our power spectra which depends upon the total observation duration, data gaps etc, create hindrance to resolve all the harmonics and sidebands precisely. The another possible candidate of spin period at ∼ 8758.12s according to Schwarz et al. (2007), which is very close to peak Ω, could not be confirmed due to the limitation of the resolution of the power spectra. We also notice that the peaks in the FPMA power spectra are stronger in 3-10 keV band compared to 10-40 keV band.
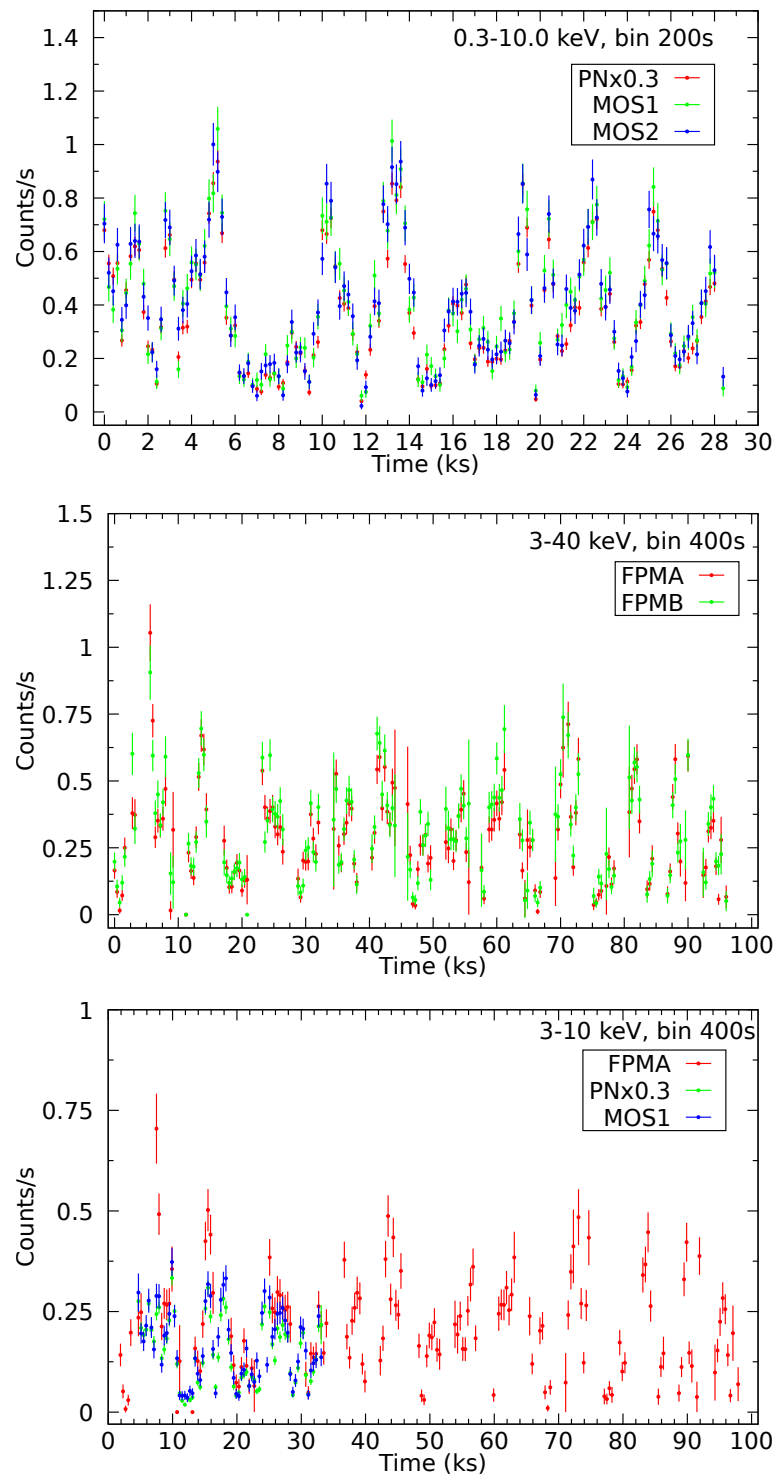
Figure 4.1: Background subtracted lightcuves from XMM-Newton (top), and NuSTAR (middle) and overlapping 3-10 keV lightcurves from both the observatories for comparison (bottom).

In the bottom panel of Fig. 4.2, we have plotted the CLEANed power spectra. Before performing the CLEAN operation, we have detrended the lightcurve for the presence of dc bias, if any, by subtracting a mean value and dividing by the standard deviation. The CLEANed algorithm requires two parameters - number of iterations and loop gain - to deconvolve the window power spectra from the DFT spectra iteratively with the gain fraction in each iteration . We chose gain 0.1, typically used (Norton et al., 1992; Rana et al., 2004) for this algorithm. Iteration number was set at 1000. We find that, the strong Ω peak and the $\Omega + 2\omega$ peak is present, however, other weak peaks at $\omega, 2\omega - \Omega$ and 2ω which were in seen in Lomb-Scargle power spectra are almost diminished in the CLEANed power spectra.

The similar exercise is done for the XMM-Newton PN power spectra (Fig. 4.3). Though the PN lightcurves are continuous, the power spectral resolution is poor due to shorter duration of the observation. We have found that the peak corresponding to Ω is evidently present, with a period value $9400 \pm 761s$, agreeing with that of the FPMA value. We are unable to distinguish neither of ω and $2\omega - \Omega$ in the PN power spectra, because of the broad peak of Ω. It is interesting to note that the peak strength of Ω is much lower in 0.3-3.0 keV band than the 3-10 keV band. However, for all other peaks in the power spectra, peak strength decreases in higher energy band. By our previous definition of orbital and spin periods from FPMA, we have marked their expected positions in the PN power spectra, along with harmonics and sideband frequencies. We notice that there is significantly strong power near the position marked by $\Omega + 2\omega$, as we found from FPMA power spectra.

Folded Lightcurves

Based on our measured orbital period ($9384 \pm 229s$), we have folded the PN and FPMA lightcurves to study the rotational properties of the source. The folding is performed based on the ephemeris TJD=19275, chosen arbitrarily close to start time of NuSTAR observation. The folded lightcurves in different energy bands and the hardness ratios (HR) are shown in Fig. 4.4. In the soft X-rays, 0.3-3.0 keV band obtained from PN (left plot of Fig. 4.4), there is strong modulation in the lightcurve, however the entire lightcurve can be described by one broad hump ($\phi = 0.7 - 1.7$), with several dips in between. There are three prominent minima, appearing at $\phi \sim 0.16, 0.50, 0.70$, with the first one being the strongest. In the 3.0-10.0 keV band, the similar broad hump like feature is visible, with the minima at $\phi \sim 0.70$ being the strongest one. A direct comparison of PN lightcurve with the FPMA lightcurve (right plot of Fig. 4.4) in the same energy band 3-10 keV, shows similar nature of the hump and the presence of a overall minima at $\phi \sim 0.70$. The pulse fraction (PF) of modulation in the 3-10 keV energy band is, $72\pm4\%$ and $72\pm6\%$ respectively from PN and FPMA, using the definition PF $= (I_{max} - I_{min})/(I_{max} + I_{min})$ where I denotes the count rate. The hard X-ray in 3-10 keV band of FPMA follows the same pattern of the lightcurve as that of 10-40 keV.
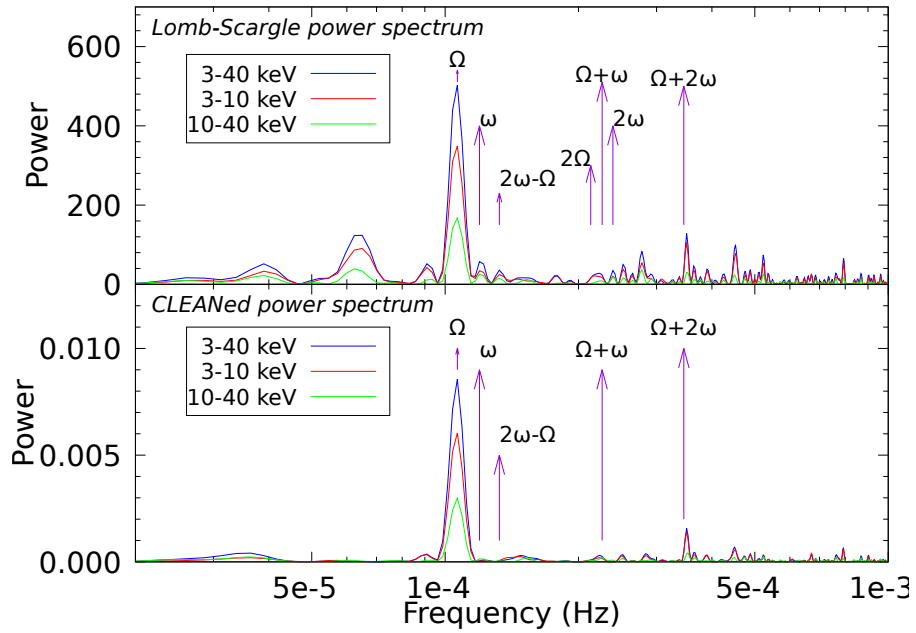
Figure 4.2: Power spectra obtained from NuSTAR-FPMA using Lomb-scargle algorithm (top figure), and CLEAN algorithm (bottom figure). We have identified the two fundamental peaks, Ω and ω, along with the location of few sideband and harmonics.
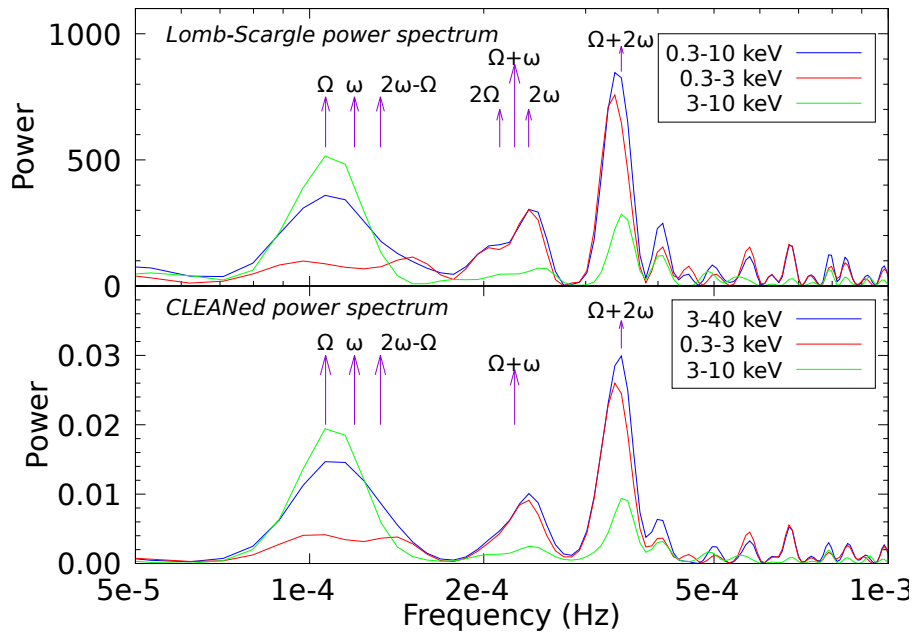
Figure 4.3: Power spectra obtained from XMM-Newton PN using Lomb-Scargle algorithm (top figure), and CLEAN algorithm (bottom figure). The Ω peak is identified along with expected (from FPMA power spectra) position of ω is marked. Few sideband frequencies and harmonics are labelled.
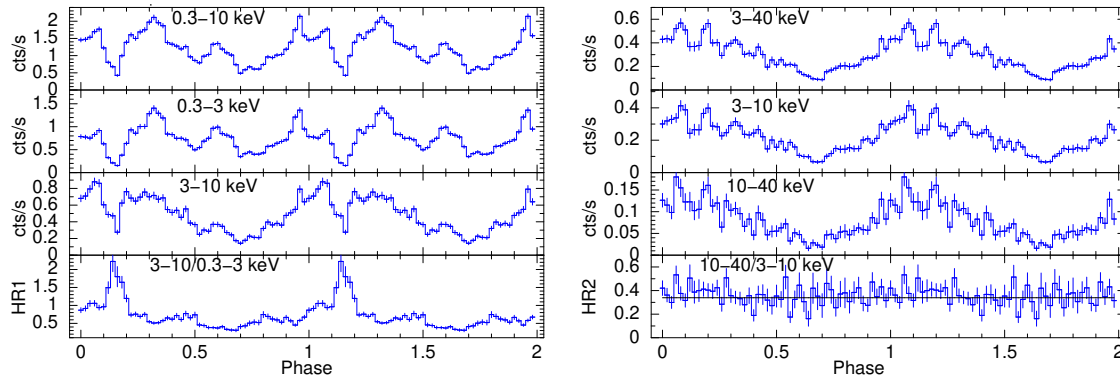
Figure 4.4: Folded lightcurve, based on period 9384s, from different energy bands, using PN (on the Left) and FPMA (on the Right) are shown. The bin size is 188s. In the bottom panels, hardness ratio-1 (Left plot) and hardness ratio-2 (right plot) are shown. A `constant` model is fitted to HR2, represented by a black line.

As we inspect the hardness ratio-1 (HR1), defined as HR1 = $I_{3-10\,\text{keV}}/I_{0.3-3.0\,\text{keV}}$, obtained from PN lightcurve, we notice a strong peak around $\phi \sim 0.16$ (bottom panel of left plot of Fig. 4.4). This corresponds to the dip at the same phase, seen in the 0.3-3.0 keV and 3.0-10.0 keV band of the PN lightcurve. The HR1 can roughly be divided in four intervals, (a) $\phi \sim 0.10 - 0.22$, (b) $\phi \sim 0.22 - 0.50$, (c) $\phi \sim 0.50 - 0.80$, and (d) $\phi \sim 0.80 - 1.10$. In HR1, the phase interval (a) shows the strong peak whereas interval (c) covers the lowest valley region. The (b) and (d) respectively represents the phase intervals before and after the peak region in the HR1.

The hardness ratio-2 (HR2), defined similarly as that of HR1, but for 10-40 keV and 3-10 keV band of FPMA, exhibit a rather flat profile (bottom panel of right plot of Fig. 4.4). We have fit a `constant` model which gives a mean value of 0.34, with an acceptable fit statistic of $\chi^2(DOF) = 141.5(100)$.

We didn't attempt detailed analysis based on the period ω, since this period appears very weakly in the FPMA power spectra and could not be resolved in PN power spectra.

4.3.2 Spectral Analysis

For the spectral analysis, X-ray Spectral Analysis Software package XSPEC v12.12.0 (Arnaud, 1996) is used. We have followed the abundance table defined by Wilms and McCray (Wilms et al., 2000) and photoelectric cross section table set after Verner et al. (1996). All the spectral models used for analysis are part of XSPEC package. The errors on the parameter values are quoted within 90% confidence levels. In this section we have first attempted the spectral analysis with NuSTAR data and XMM-Newton data separately, to have an idea on how the spectra can be modelled in the hard X-ray part and the soft-X ray part, along with detecting the strong line emissions present in the spectra. Finally we have employed the complete spectral model to jointly fit the broadband spectral data obtained from both the observatories.

Phenomenological fit to NuSTAR spectra

The FPMA and FPMB data in 3-40 keV range are employed for probing the shock temperature of PSR and the presence of Compton reflection hump. Beyond 40 keV the background dominates over the source counts, hence not included for the spectral analysis. Initially we have used an absorbed bremsstrahlung model, with a single Gaussian component for modelling the iron line complex, which could not be resolved by NuSTAR data. We obtain a good fit with $\chi^2/DOF = 463(439)$. The column density of the absorber is $3.76^{+1.32}_{-1.27} \times 10^{22} \ cm^{-2}$. This value is larger than the total galactic column density along the direction of the source, $0.42 \times 10^{22} cm^{-2}$ (HI4PI Collaboration et al., 2016). This indicates a strong absorption specific to the source, is present in the spectra. The obtained continuum temperature is $19.9^{+1.9}_{-1.7}$keV. The Gaussian component shows a line energy of $6.59^{+0.05}_{-0.05}$ keV, with a $\sigma = 247^{+67}_{-59}$eV, indicating presence of significant ionised Fe K_α lines.

Since the PSR is multitemperature in nature, the obtained bremsstrahlung temperature, indicates an average temperature of entire PSR. Therefore we used isobaric cooling flow model mkcflow (Mushotzky & Szymkowiak, 1988) to model the PSR (Mukai et al., 2003). This model also incorporates the ionised line emissions including the ionised Fe K_α lines (He-like and H-like). We kept switch parameter set at 2 to determine the spectra based on AtomDB 3.0.9 [3]. The redshift parameter is fixed at 1.35×10^{-7} following the GAIA DR2 distance of 578 ± 35pc (Gaia Collaboration et al., 2018). We have also incorporated the absorption component tbabs . For the neutral iron Kα line at 6.4 keV, we have added a Gaussian component with line central energy fixed at 6.4 keV and line width σ fixed at 0 (as suggested by spectral analysis of XMM-Newton EPIC data, discussed in the next section). We obtained an acceptable fit with $\chi^2(DOF) = 470(440)$. The overall absorber column density remains similar that of the bremsstrahlung fit within statistical uncertainty. The lower temperature reached the lower limit allowed by the model, so we fixed it at 0.0808keV. The upper temperature comes out to be $42.9^{+5.5}_{-5.0}$ keV. To check the presence of Compton reflection, we convolved reflect component with the multitemperature cooling flow model, . It slightly improves the fit statistic to $\chi^2(DOF) = 464(439)$, but the reflection amplitude, gives a high value $0.93^{+0.87}_{-0.65}$ with large uncertainty associated with it. The upper temperature is somewhat lowered in this case, standing at $27.9^{+8.6}_{-5.1}$keV. The value of the other parameters remain similar with no-reflection fit within statistical uncertainty. A strong and complex absorption can affect the spectra beyond 7 keV, thereby the continuum itself. Therefore, we can comment on reflection only after properly modelling the absorption in the source by including soft X-rays from XMM-Newton data.

Phenomenological fit to XMM-Newton spectra

First we have utilized the EPIC (PN, MOS1 and MOS2) spectra in 5-8 keV range to study the Fe K_α emission lines. We have used the absorbed bresmsstrahlung model to fit the

---

[3] The same setting is used for subsequent spectral analysis, whenever required
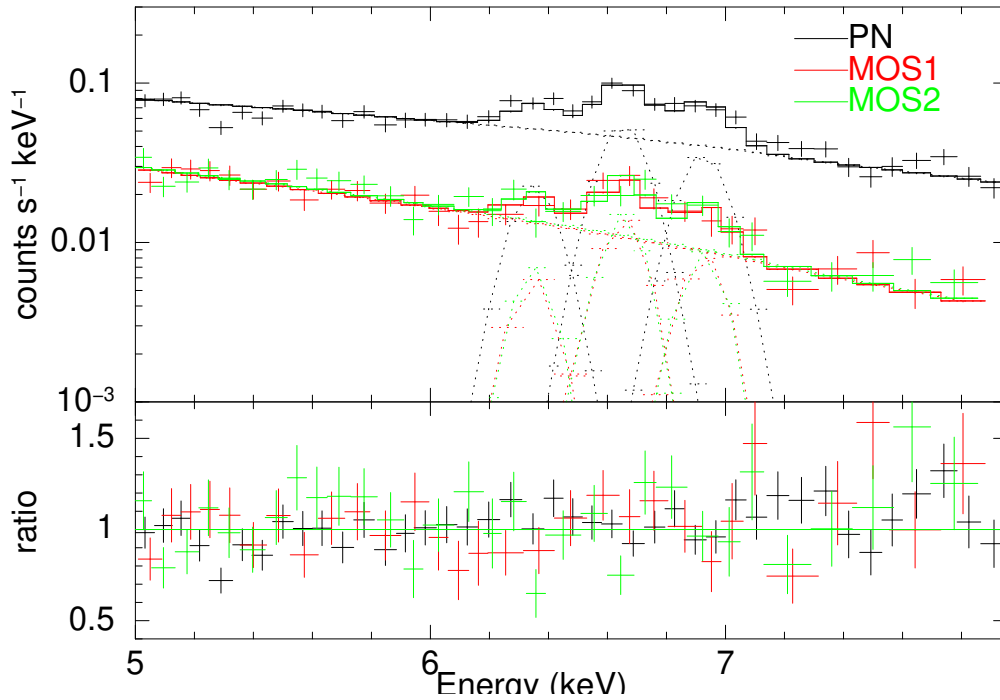
Figure 4.5: Fe K_α lines are fitted with three Gaussian components over an absorbed bremsstrahlung continuum using EPIC data in 5-8 keV range. We show the spectra and data to model ratio in the top and bottom panel respectively

.

underlying continuum. We have added three Gaussians to model the three iron K_α lines; neutral, He-like and H-like. The best-fit parameter values are reported in Table 4.1 with the spectral fitting plotted in Fig. 4.5. The line widths are kept fixed at 0 since all the Fe K_α lines are consistent with the instrumental resolution limit of EPIC (~ 120eV at 6.0keV). This shows that lines are narrow. We have fixed bremsstrahlung temperature and column density of absorber at 19.9 keV and 3.76×10^{22} cm^{-2}, as obtained with NuSTAR only fit using bremsstrahlung model (see Sect. 4.3.2), which otherwise couldn't be constrained. We notice the best-fit values of the line central energies are slightly redshifted, however, that is not statistically important as they agree with their expected theoretical values within error-bar.

We have next looked into the RGS spectra. The spectra from RGS1 and RGS2 are simultaneously fit in 0.45-2.0 keV. The signal to noise ratio of the spectral data is poor, with only 47% of the total count is contributed from source. However, the ionised oxygen line (O-VII) in the spectra is clearly present. To get an overview of the ionised line, we fitted the line with a Gaussian component on top of an absorbed bremsstrahlung continuum. The spectra is shown in Fig. 4.6. The line center appears at $0.568^{+0.004}_{-0.004}$keV with line width (σ) of 6^{+5}_{-2}eV and an equivalent width of 117^{+70}_{-77}eV. We note that, the O-VII line is composed of fine atomic transition lines (intercombination, resonance and forbidden lines), which RGS can not resolve, thereby giving rise to a broad line width. There is visibly some

Table 4.1: Probing Iron lines using EPIC data (5.0-8.0keV)

Parameter	Unit	Value
$n_{H,tb}$	$10^{22} cm^{-2}$	3.76_f
T_{br}	keV	19.9_f
N_{br}	$\times 10^{-3}$	$1.82^{+0.05}_{-0.05}$
$E_{L, Neutal}$	keV	$6.35^{+0.05}_{-0.04}$
σ_{Neutal}	eV	0_f
eqw_{Neutal}	eV	66^{+30}_{-18}
$N_{L, Neutal}$	$\times 10^{-5}$	$0.7^{+0.2}_{-0.2}$
$E_{He-Like}$	keV	$6.66^{+0.02}_{-0.02}$
$\sigma_{He-Like}$	eV	0_f
$eqw_{He-Like}$	eV	182^{+28}_{-23}
$N_{He-Like}$	$\times 10^{-5}$	$1.9^{+0.2}_{-0.2}$
E_{H-Like}	keV	$6.93^{+0.02}_{-0.03}$
σ_{H-Like}	eV	0_f
eqw_{H-Like}	eV	137^{+24}_{-24}
N_{H-Like}	$\times 10^{-5}$	$1.3^{+0.2}_{-0.2}$
$\chi^2(DOF)$		123(93)

\# $n_{H,tb}$ represents column density of the absorber. T_{br} and N_{br} denote the temperature and normalisation of bremsstrahlung continuum.

★ E_L, σ, N_L and 'eqw' respectively represent line central energy, line width, normalisation, and equivalent width of the corresponding Fe K_α line

‡ f denote the line parameter is fixed.
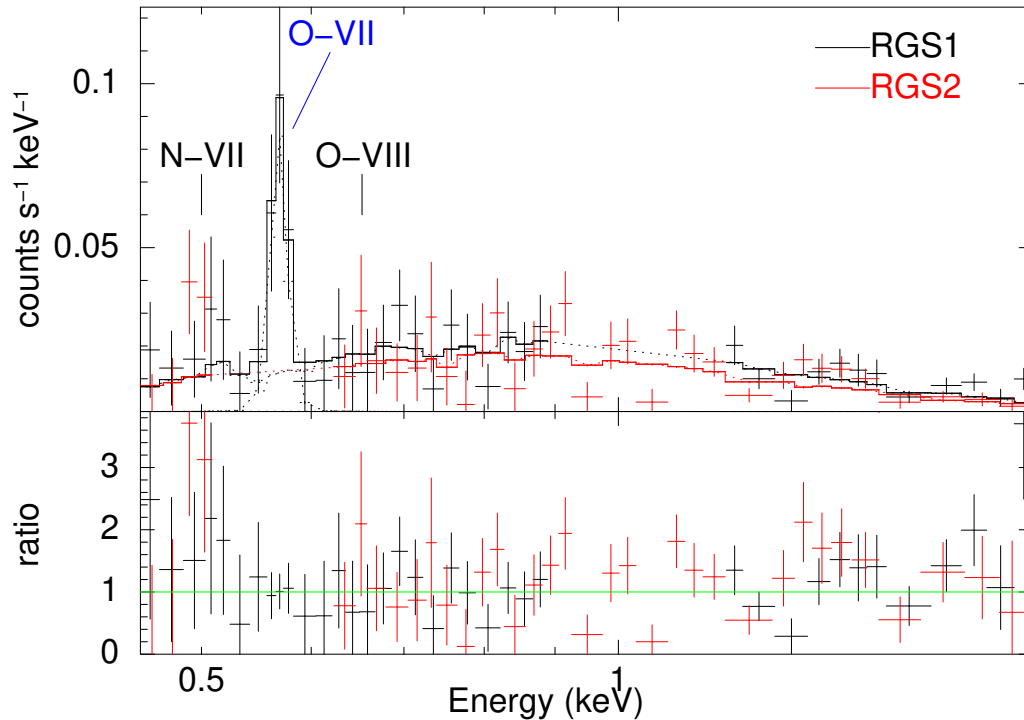
Figure 4.6: Fitting O-VII K_α line in RGS spectra. The spectral quality is poor, but O-VII line appears with significant strength and fitted with a Gaussian over an absorbed bremsstrahlung continuum. The spectra and data to model ratio are shown in top and bottom panel respectively. Expected location of O-VIII and N-VII K_α lines are marked.

excess residual around 0.5 keV, expected from N-VII line. But poor signal to noise ratio for that line makes it statistically unimportant.

In order to constrain the absorption parameters, as well as the nature of the multitemperature PSR, the spectral data from all the three EPIC cameras were simultaneously fit in the 0.3-10.0 keV band. We have used ISM absorption model `tbabs` for modelling the overall absorption near the source as well as any intervening galactic absorption. The multitemperature plasma of the PSR has been modelled with the cooling flow model, implemented by `mkcflow`. The The neutral Fe K_α line is described by an narrow ($\sigma = 0$) Gaussian component. The absorbed cooling flow model with a Gaussian component gives extremely poor fit statistic $\chi^2(DOF) = 5447(424)$. Inclusion of an partial covering absorber dramatically improves the fit, with a $\chi^2(DOF) = 604(421)$. The overall column density appears to be $\sim 6.3 \times 10^{20}\ cm^{-2}$ and partial covering absorber with column density $\sim 6.08 \times 10^{22}\ cm^{-2}$ and covering fraction of $\sim 65\%$. However, the upper temperature of the cooling flow model remains unconstrained (79 keV), the overall abundance is very large (~ 3.77), and the fit statistic is still poor, and deserve further improvement. Inclusion of a `reflect` model substantially improves the fit to $\chi^2(DOF) = 501(420)$, but it appear with an unphysical and large value of reflection amplitude ~ 8.24. A poor fit with a single partial covering component suggests that absorption should require more elaborate

modelling. Also, getting such a high value of reflection amplitude indirectly points that, absorption has an extended effect till the energy range beyond 7 keV which can also be mimicked by tail of reflection hump for an alleged strong Compton reflection. Therefore, instead of `reflect`, we introduced another partial covering absorber (`pcfabs_1*pcfabs_2`). Two partial covering absorbers mathematically describe abosorbers with three column densities and corresponding covering fraction (Eqn 4.1)

$$
\begin{aligned}
&[f_{pc1}e^{-n_{\text{H,pc1}}\sigma(E)} + (1 - f_{pc1})] \times [f_{pc2}e^{-n_{\text{H,pc2}}\sigma(E)} + (1 - f_{pc2})] \\
&= A + Be^{-n_{\text{H,pc1}}\sigma(E)} + Ce^{-n_{\text{H,pc2}}\sigma(E)} + De^{-(n_{\text{H,pc1}}+n_{\text{H,pc2}})\sigma(E)}
\end{aligned}
\tag{4.1}
$$

Here $\sigma(E)$ stands for photoelectric cross section, $n_{\text{H,pc1}}$, f_{pc1} and $n_{\text{H,pc2}}$, f_{pc1} represent column densities and covering fraction contributed from each partial absorber model component. B, C, D are the functions of f_{pc1} and f_{pc2} and represent respective fraction of each of the resultant three column densities, and $A = 1 - (B + C + D)$.

The fit with two partial covering absorber improves the fit statistic significantly ($\chi^2(DOF) = 478(419)$) in comparison to single partial partial absorber model. The column density of the overall absorber is $3.42^{+1.13}_{-1.09} \times 10^{20}$ cm^{-2}. The column density and covering fraction of the two `pcfabs` components become $2.55^{+0.46}_{-0.39} \times 10^{22}$ cm^{-2} with $65 \pm 3\%$ and $22.65^{+5.40}_{-4.20} \times 10^{22}$ cm^{-2} with $50 \pm 5\%$. The upper temperature of the cooling flow model is constrained with a value of $43.2^{+15.7}_{-12.2}$keV. Though the error bars are large, it is expected due to limited coverage of hard X-rays by XMM-Newton data. The lower temperature of $0.86^{+0.29}_{-0.24}$ keV represents some mean temperature near the bottom region of the PSR. At this point we observe slight excess in the soft X-rays, possibly arising due to line emissions of low-Z and Fe L-shell emissions. The main excess is around 0.57keV, representing the O-VII line, which is also observed from RGS spectra. To model that, we introduced an extra optically thin plasma emission component (`mekal`), appearing with a temperature $0.17^{+0.04}_{-0.05}$ keV, which decreased the fit statistic further to $\chi^2(DOF) = 466(417)$. The corresponding F-statistic probability for inclusion of this extra component is 4.9×10^{-3}.

It is evident that the source spectra involves a complicated absorption scenario, where it is paramount to model it appropriately. Motivated by the fact that single partial absorber is not enough to model the local intrinsic absorber, which indicated a distribution of column densities, we introduced `pwab` (Done & Magdziarz, 1998) component to model the intrinsic absorber. This component assumes power law distribution of the covering fraction as a function of column density of neutral absorbers. The fit statistic is $\chi^2(DOF) = 470(418)$, closely similar to the fit statistic obtained from previous two partial absorber fit. We kept the $n_{H,\text{min}}$ of the power law absorber fixed to 1×10^{15} cm^{-2}, which could not be constrained otherwise. The $n_{H,\text{max}}$ provides a value $32.09^{+15.61}_{-6.78} \times 10^{22}$ cm^{-2} along with a power law index of $-0.60^{+0.01}_{-0.01}$. We could not constrain the column density of overall absorber either, which provided us with an upper limit of $< 7.0 \times 10^{19}$ cm^{-2}. However, The parameters from emission components remains similar with the fit of two partial covering

Table 4.2: Model description in XSPEC notation

Abbreviation	Model
M1	`constant*tbabs*pcfabs*pcfabs*(mckflow+mekal+gauss)`
M1-R	`constant*tbabs*pcfabs*pcfabs*(reflect*(mckflow+mekal)+gauss)`
M2	`constant*tbabs*pwab*(mckflow+mekal+gauss)`
M2-R	`constant*tbabs*pwab*(reflect*(mckflow+mekal)+gauss)`
M3	`constant*tbabs*zxipab*(mckflow+gauss)`
M3-R	`constant*tbabs*zxipab*(reflect*mckflow+gauss)`

absorber scenario within statistical uncertainty. Here we notice that, the F-test probability of introducing the extra optically thin component to model the emission features below 1 keV, is 1.5×10^{-18}, indicating much stronger necessity for this component than the two partial absorber case.

Given the complex intrinsic absorber scenario of Paloma, and emission features in soft X-rays, we have also performed an alternate modelling using `zxipab` (Islam & Mukai, 2021). This component can describe the absorption in the pre-shock flow as the power law distribution of warm photoionised absorber, hence providing an alternate description of the soft X-ray features. In this case, we do not introduce extra low temperature plasma emission component. We obtain a similarly good fit statistic like previous cases, $\chi^2(DOF) = 467(420)$. The overall absorber presents itself with a column density of $4.03^{+1.42}_{-1.25} \times 10^{20} \ cm^{-2}$, consistent with two partial absorber scenario. The warm absorber shows a column density value of $31.76^{+10.25}_{-6.68} \times 10^{22} \ cm^{-2}$ for $n_{H,\mathrm{max}}$, and we kept the $n_{H,\mathrm{min}}$ frozen at the lowest value permissible for this parameter ($10^{15} \ cm^{-2}$), because of it becoming unconstrained. The low temperature of cooling flow component now goes to the lower limit allowed by the model, so fixed at 0.0808 keV. The upper temperature ($34.5^{+14.9}_{-7.3}$keV) is consistent with the value obtained from previous two scenarios within statistical uncertainty.

Simultaneous fit to broadband XMM-Newton and NuSTAR spectra

Equipped with our understanding of the complex absorber and the overall continuum from the XMM-only and NuSTAR-only fit, we devised three model variants M_1, M_2, M_3 to model the broadband spectra in 0.3-40.0 keV. The description of the model variants are mentioned in Table 4.2.

We have quoted the best fit values of the parameters in the Table 4.3. For representation, the spectral and ratio (data/model) plots using model M1 are shown in top and middle panels of Fig. 4.7. The spectral parameters agree within the statistical uncertainty for all the three models. However, for model M2, we could not constrain the column density of overall absorber, and a upper limit ($< 0.7 \times 10^{20} \ cm^{-2}$) is obtained. For a low
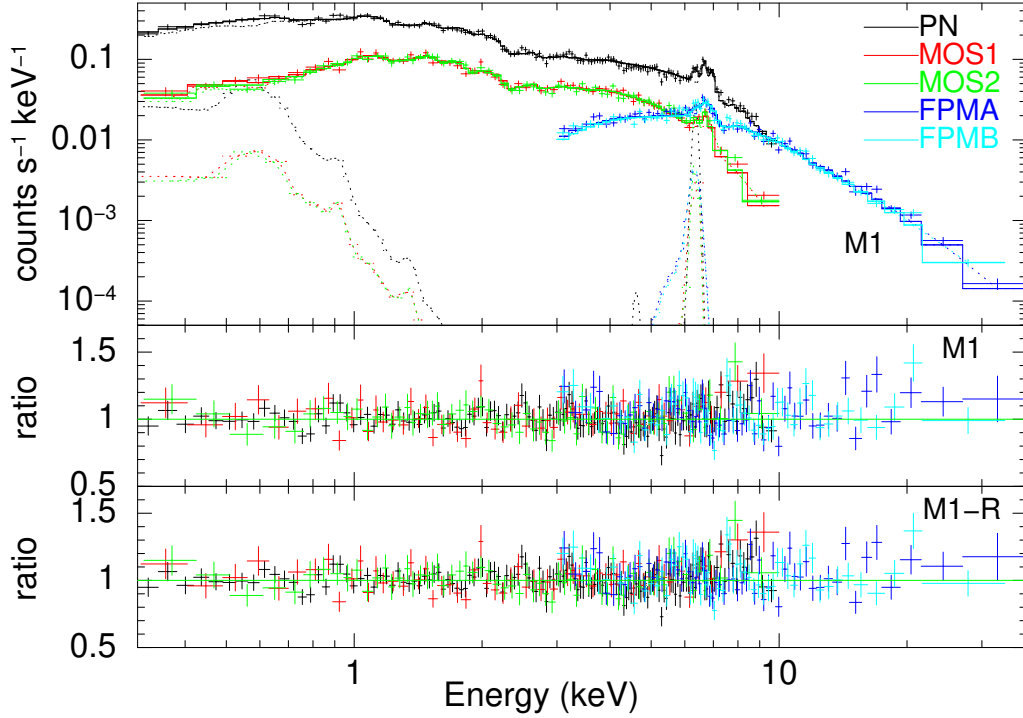
Figure 4.7: The top and middle panel show the plots of the best-fit model and ratio (data/model) for the broadband spectra using model variant M1. We In the bottom panel we show the ratio plot using "`reflect`" version of the model M1, i.e M1-R.

value of overall absorber which includes the galactic absorption, it maybe hard to constrain this parameter, given that we already have a complex intrinsic absorber component to describe the spectra. It is also to be noted that, the neutral power law distribution of absorber `pwab` and the ionised version `zxipab` have significant differences in predicting the model flux below < 0.8 keV (Fig. 1 of Islam & Mukai (2021)). This gives rise to differences in the obtained column densities of the overall absorber between model M2 and M3. All of the M1, M2, and M3 give us consistently statistically acceptable fit, with a $\chi^2(DOF) = 952(859), 956(862), 952(863)$ respectively. Also, the emission parameters for all three model variants give statistically similar values.

Once our spectral model has satisfactorily constrained the absorption parameters and the continuum, we attempted to find the contribution of Compton reflection. We adopted model variants M1-R, M2-R and M3-R (for model description, see Table 4.2), with the abundance parameters of `reflect` component linked to that of emission components. We used default value of the inclination angle (i), set at $\mu = \cos i = 0.45$. The three models produced a reflection amplitude of $0.39^{+0.48}_{-0.25}$, $0.47^{+0.43}_{-0.35}$ and $0.26^{+0.45}_{-0.26}$ along with an improvement in fit-statistic, however not large, of $\Delta\chi^2(\Delta DOF) = 4(1), 4(1)$ and $1(1)$ respectively (Table 4.3). The ratio (data/model) plot using model M1-R is shown in bottom panel of Fig. 4.7. Though mutually agreeing values of reflection amplitudes are obtained in all three models, the large statistical uncertainty and small improvement in fit-stat puts

Table 4.3: Best-fit parameters using simultaneous broadband spectra in 0.3–40.0 keV

Parameter	Unit	M1	M1-R	M2	M2-R	M3	M3-R
$n_{H,tb}$	10^{20} cm^{-2}	$4.5^{+1.2}_{-1.2}$	$4.5^{+1.2}_{-1.2}$	<0.7	<0.7	$4.7^{+1.3}_{-1.3}$	$4.5^{+1.4}_{-1.3}$
$n_{H,pc1}$	10^{22} cm^{-2}	$2.2^{+0.4}_{-0.4}$	$2.1^{+0.4}_{-0.2}$	...	...	...	...
pcf1 / log(xi)[†a]		$0.66^{+0.02}_{-0.03}$	$0.66^{+0.02}_{-0.02}$	...	...	$0.6^{+0.1}_{-0.1}$	$0.6^{+0.1}_{-0.1}$
$n_{H,pc2}$ / $n_{H,max}$ [†b]	10^{22} cm^{-2}	$20.0^{+3.1}_{-3.1}$	$19.0^{+3.2}_{-2.8}$	$27.6^{+7.3}_{-4.1}$	$25.2^{+6.8}_{-4.1}$	$30.5^{+7.3}_{-5.4}$	$28.8^{+7.9}_{-4.6}$
pcf2 / β [†c]		$0.54^{+0.03}_{-0.04}$	$0.54^{+0.03}_{-0.03}$	$-0.59^{+0.01}_{-0.01}$	$-0.58^{+0.01}_{-0.02}$	$-0.55^{+0.01}_{-0.01}$	$-0.58^{+0.02}_{-0.02}$
T_{me}	keV	$0.18^{+0.03}_{-0.05}$	$0.18^{+0.03}_{-0.05}$	$0.19^{+0.02}_{-0.02}$	$0.19^{+0.02}_{-0.02}$	$0.19^{+0.02}_{-0.02}$	...
N_{me}	10^{-4}	$1.7^{+1.1}_{-0.1}$	$2.0^{+1.2}_{-0.9}$	$4.5^{+1.7}_{-1.0}$	$5.5^{+1.5}_{-1.3}$	...	...
$T_{1,mkc}$	keV	$0.67^{+0.18}_{-0.17}$	$0.67^{+0.19}_{-0.16}$	$0.68^{+0.17}_{-0.19}$	$0.69^{+0.18}_{-0.17}$	$0.69^{+0.18}_{-0.17}$	...
$T_{2,mkc}$	keV	$34.2^{+4.2}_{-2.5}$	$29.6^{+4.9}_{-4.9}$	$33.6^{+1.9}_{-4.2}$	$27.9^{+5.8}_{-3.9}$	$31.7^{+3.3}_{-3.5}$	$28.5^{+5.4}_{-3.6}$
N_{mkc}	10^{-11}	$11.1^{+1.0}_{-1.3}$	$12.0^{+1.5}_{-1.4}$	$10.6^{+1.9}_{-1.1}$	$11.8^{+1.6}_{-1.5}$	$11.8^{+1.9}_{-1.4}$	$12.3^{+1.7}_{-1.8}$
Z	$Z_\odot$	$1.4^{+0.2}_{-0.2}$	$1.2^{+0.2}_{-0.2}$	$1.2^{+0.2}_{-0.2}$	$1.1^{+0.2}_{-0.2}$	$1.2^{+0.2}_{-0.2}$	$1.1^{+0.2}_{-0.2}$
$\Omega/2\pi$		...	$0.39^{+0.48}_{-0.25}$	...	$0.47^{+0.43}_{-0.35}$	0.0808_f	$0.26^{+0.45}_{-0.26}$
E_L	keV	$6.36^{+0.04}_{-0.02}$	$6.36^{+0.03}_{-0.04}$	$6.36^{+0.04}_{-0.04}$	$6.37^{+0.04}_{-0.05}$	$6.34^{+0.06}_{-0.01}$	$6.36^{+0.04}_{-0.04}$
σ	eV	0_f	0_f	0_f	0_f	0_f	0_f
N_L	10^{-5}	$1.0^{+0.2}_{-0.2}$	$0.9^{+0.2}_{-0.2}$	$0.9^{+0.2}_{-0.2}$	$0.8^{+0.2}_{-0.2}$	$0.9^{+0.2}_{-0.2}$	$0.8^{+0.2}_{-0.2}$
$\chi^2(DOF)$		952(859)	948(858)	956(862)	952(861)	952(863)	951(862)

†a: Read pcf1 (covering fraction for first partial absorber) for model M1, and log(xi) (ionisation parameter of warm power law absorber) for model M3.

†b: Read $n_{H,pc2}$ (column density of second partial absorber) for model M1, and $n_{H,max}$ (maximum column density of the neutral (and warm) power law absorber) for model M2 (and M3).

†c: Read pcf2 (covering fraction for second partial absorber) for model M1, and β (power law index of neutral (and warm) absorber) for model M2 (and M3).

$n_{H,tb}$ and $n_{H,pc1}$ respectively denote column density of overall and first partial absorber. $T_{1,mkc}$, $T_{2,mkc}$ and N_{mkc} denote upper & lower temperature and normalization of isobaric cooling flow component. T_{me}, N_{me} are temperature and normalisation of optically thin cold plasma emission component. Z stands for overall abundance. E_L, σ, N_L represent line energy, line width and normalisation of the Gaussian component for the neutral Fe K$_\alpha$ line respectively.

★ f denotes the parameter is fixed.

us in a delicate situation to comment about its "robust" presence in our spectra.

Phase resolved spectroscopy

Our orbit folded lightcurve (Fig. 4.4) showed prominent variation in the HR-1, indicating the presence of the change in the complex intrinsic absorber. We extracted phase-resolved spectra in the four phase intervals as defined in section 4.3.1. We have quoted the best-fit parameters for the phase-resolved spectra in Table 4.4. We kept the column density of the overall absorber fixed at the best fit value from the phase averaged spectral fitting. The temperatures of the plasma emission components remain same within statistical uncertainty for all the phases as well as with the phase-averaged value, for any particular model variant. Though the column density of the complex absorbers also remain same within error-bar, our spectral fitting clearly reveals the change in the covering fraction parameters. For phase (a) the model M1 show highest value of the covering fraction (pcf1 and pcf2) for the intrinsic absorbers ($0.79^{+0.04}_{-0.04}$ and $0.73^{+0.05}_{-0.06}$), whereas for the phase (c), the lowest values of those parameters are obtained ($0.49^{-0.11}_{+0.06}$ and $0.31^{+0.12}_{-0.16}$). The parameter values (pcf1 and pcf2) for other two phases - phase (b) ($0.67^{+0.05}_{-0.04}$ and $0.50^{+0.05}_{-0.06}$) and phase (d) ($0.70^{+0.03}_{-0.04}$ and $0.54^{+0.04}_{-0.06}$) are consistent with each other. The model M2 and M3 follow same trend with the power law index for the complex absorber. We obtain highest value of the power law index(~ -0.3) for phase (a) and lowest value (~ -0.7) for phase (c), whereas the phase (b) and (d) gives intermediate values (~ -0.5), similar to each other. For model M_3, we also obtain a low value of ionisation parameter (~ -1.3) during phase (c), compared to other three phases ($\sim 0.7, 0.7, 0.5$ for (a), (b), (d) respectively).

4.4 Discussion

Paloma, one of a unique sources among IPs, has been observed simultaneously in the broadband X-rays (0.3-40 keV) for the first time. We have studied the X-rays properties of the source and in the following section we discuss our results.

4.4.1 Modulations in the lightcurve

The single hump like structure in the orbit folded lightcurve covering a full cycle denotes we are seeing emissions from at least one pole at any point of time during the orbital motion of the WD. The energy dependent dips arise due to presence of complex inhomogeneous absorber. During dip, around the phase (a) ($\phi = 0.10 - 0.22$), we believe the column density of the absorber is the maximum along the line of sight, causing the soft X-rays below 3 keV to undergo maximum absorption. This is what causes the peak in the HR1 (Fig 4.4)at same phase. This absorption feature also appears in the 3-10 keV band, indicating that the column density of the absorber is very high during this phase. However, the amplitude of the dip decreases with increasing energy. The complex intrinsic absorber also describes another extra dip at $\phi \sim 0.5$ in the soft X-rays below 3 keV, but does not impact the lightcurve above 3 keV.

Table 4.4: Best fit parameters for phase Resolved spectra in 0.3–40.0 keV

Parameter	Unit	M1				M2				M3			
		(a)	(b)	(c)	(d)	(a)	(b)	(c)	(d)	(a)	(b)	(c)	(d)
		0.10–0.22	0.22–0.50	0.50–0.80	0.80–1.10	0.10–0.22	0.22–0.50	0.50–0.80	0.80–1.10	0.10–0.22	0.22–0.50	0.50–0.80	0.80–1.10
$n_{H,tb}$	10^{20} cm^{-2}	4.5_f	4.5_f	4.5_f	4.5_f	0.7_f	0.7_f	0.7_f	0.7_f	4.7_f	4.7_f	4.7_f	4.7_f
$n_{H,pc1}$	10^{22} cm^{-2}	$2.3^{+0.7}_{-0.8}$	$1.8^{+0.5}_{-0.3}$	$2.9^{+1.4}_{-1.5}$	$1.9^{+0.4}_{-0.5}$	...	...	...	...	...	...	...	...
pcf1 / log(xi)		$0.79^{+0.04}_{-0.04}$	$0.67^{+0.05}_{-0.04}$	$0.49^{+0.06}_{-0.11}$	$0.70^{+0.03}_{-0.04}$	...	...	...	...	$0.66^{+0.16}_{-0.16}$	$0.68^{+0.12}_{-0.12}$	$-1.30^{+0.21}_{-0.19}$	$0.46^{+0.10}_{-0.09}$
$n_{H,pc2}$ / $n_{H,max}$	10^{22} cm^{-2}	$20.9^{+5.6}_{-4.3}$	$16.3^{+5.7}_{-4.3}$	$21.2^{+21.5}_{-20.2}$	$18.3^{+5.4}_{-4.1}$	$34.6^{+17.7}_{-10.0}$	$18.1^{+9.3}_{-4.7}$	$20.1^{+15.3}_{-8.8}$	$21.7^{+10.7}_{-5.7}$	$38.9^{+17.0}_{-10.2}$	$20.2^{+7.0}_{-4.3}$	$18.6^{+39.1}_{-10.2}$	$22.8^{+9.2}_{-4.8}$
pcf2 / β		$0.73^{+0.05}_{-0.06}$	$0.50^{+0.05}_{-0.06}$	$0.31^{+0.12}_{-0.16}$	$0.54^{+0.04}_{-0.06}$	$-0.36^{+0.04}_{-0.02}$	$-0.59^{+0.03}_{-0.03}$	$-0.74^{+0.03}_{-0.02}$	$-0.57^{+0.02}_{-0.02}$	$-0.32^{+0.04}_{-0.04}$	$-0.55^{+0.02}_{-0.02}$	$-0.77^{+0.03}_{-0.02}$	$-0.52^{+0.02}_{-0.02}$
T_{me}	keV	< 0.27	< 0.19	0.18_f	$0.12^{+0.05}_{-0.04}$	$0.18^{+0.04}_{-0.08}$	$0.17^{+0.03}_{-0.03}$	$< 0.22^{+0.05}_{-0.06}$	$0.12^{+0.04}_{-0.02}$	0.0808_f	0.0808_f	0.0808_f	0.0808_f
N_{me}	10^{-4}	$4.4^{+4.5}_{-3.7}$	$3.4^{+2.1}_{-1.6}$	$0.4^{+0.7}_{-0.4}$	$3.7^{+5.8}_{-2.6}$	$16.8^{+23.2}_{-8.6}$	$5.2^{+3.2}_{-1.7}$	$1.3^{+0.9}_{-0.6}$	$8.0^{+7.8}_{-3.4}$	...	...	...	...
$T_{1,mkc}$	keV	< 1.28	< 0.98	< 0.90	< 0.86	< 1.41	$0.72^{+0.53}_{-0.35}$	< 0.87	$0.58^{+0.30}_{-0.24}$	$33.3^{+17.0}_{-10.2}$	$33.7^{+9.6}_{-6.1}$	$28.3^{+11.6}_{-16.0}$	$40.3^{+9.0}_{-8.3}$
N_{mkc}	10^{-11}	$12.1^{+4.2}_{-3.7}$	$12.0^{+2.8}_{-2.3}$	$4.6^{+1.9}_{-1.2}$	$10.9^{+2.4}_{-2.0}$	$13.1^{+8.6}_{-4.5}$	$10.6^{+3.6}_{-2.1}$	$4.4^{+0.2}_{-0.1}$	$9.9^{+3.4}_{-2.0}$	$14.9^{+9.2}_{-4.8}$	$11.8^{+3.2}_{-2.6}$	$6.5^{+2.8}_{-1.7}$	$11.1^{+3.6}_{-2.1}$
$T_{2,mkc}$	keV	$41.2^{+17.5}_{-10.4}$	$35.4^{+5.7}_{-6.2}$	$38.2^{+13.9}_{-9.3}$	$43.6^{+11.2}_{-7.4}$	$35.7^{+17.6}_{-10.8}$	$36.8^{+9.4}_{-7.7}$	$38.0^{+13.0}_{-10.0}$	$44.2^{+11.1}_{-8.6}$	...	...	...	...
Z	$Z_\odot$	$1.6^{+0.6}_{-0.6}$	$1.8^{+0.5}_{-0.4}$	$1.3^{+0.6}_{-0.4}$	$1.6^{+0.7}_{-0.4}$	$1.2^{+0.8}_{-0.6}$	$1.7^{+0.6}_{-0.4}$	$1.3^{+0.6}_{-0.4}$	$1.5^{+0.5}_{-0.4}$	$1.2^{+0.6}_{-0.5}$	$1.6^{+0.5}_{-0.4}$	$0.8^{+0.3}_{-0.3}$	$1.3^{+0.4}_{-0.4}$
LineE	keV	$6.48^{+0.08}_{-0.12}$	$6.32^{+0.03}_{-0.03}$	$6.44^{+0.07}_{-0.10}$	$6.38^{+0.05}_{-0.05}$	$6.48^{+0.09}_{-0.08}$	$6.32^{+0.03}_{-0.03}$	$6.43^{+0.07}_{-0.09}$	$6.38^{+0.06}_{-0.05}$	$6.48^{+0.09}_{-0.07}$	$6.32^{+0.04}_{-0.03}$	$6.45^{+0.10}_{-0.05}$	$6.38^{+0.05}_{-0.05}$
σ	eV	0_f	0_f	0_f	0_f	0_f	0_f	0_f	0_f	0_f	0_f	0_f	0_f
N_{line}	10^{-5}	$1.5^{+0.8}_{-0.7}$	$1.6^{+0.4}_{-0.4}$	$0.5^{+0.3}_{-0.2}$	$1.1^{+0.4}_{-0.4}$	$1.4^{+0.8}_{-0.7}$	$1.4^{+0.4}_{-0.4}$	$0.5^{+0.2}_{-0.2}$	$1.0^{+0.4}_{-0.3}$	$1.3^{+0.8}_{-0.7}$	$1.4^{+0.4}_{-0.4}$	$0.5^{+0.3}_{-0.3}$	$10.1^{+3.4}_{-3.5}$
χ^2(DOF)		200(203)	393(427)	347(304)	503(463)	203(205)	399(429)	345(305)	506(465)	210(207)	405(431)	355(307)	502(467)

Symbols carry same meaning as that of Table 4.3

The periodic absorption features present at $\phi \sim 0.16$ and 0.5 in the orbital cycle for the soft to medium X-rays (0.3-10.0 keV) of the PN lightcurve can be contributed from absorbing material produced by stream-disc or stream-magnetosphere interactions (Norton et al., 1996; Parker et al., 2005). However, due to close proximity of the orbital and spin periods, and short duration of the PN lightcurve (covering few spin and orbital cycles), the periodic absorption features from accretion curtain or accretion stream arising in the spin cycle can also contribute to the features in orbit folded PN lightcurve.

The significant power at orbital frequency Ω is representative of strong periodic variation at this period. The minima at $\phi \sim 0.7$ during phase (c) is present in all the energy bands in the orbit folded lightcurves, obtained from both the telescopes. Presence of dense blob of material fixed in orbital frame along the line of sight, capable of obstructing hard X-rays can be a possible explanation for this feature during phase (c). We also note relatively weaker peak at Ω in the soft 0.3-3.0 keV band w.r.t to the medium 3.0-10.0 keV band. This can happen because of the features coming from the absorbers fixed in spin phase affect the soft X-rays (0.3-3.0 keV) in PN lightcurve more dominantly, and gets superposed with the modulation features arising in the orbital cycle, thereby reducing the power at Ω in the soft energy band.

The earlier photometric observations revealed variation of spin modulations over a complete beat cycle. Littlefield et al. (2022) found that spin profile changes from single peak to double peak structure and they proposed pole switching or grazing eclipse. Schwarz et al. (2007) showed the change in modulations of the double hump structure (Their case B). They argued for pole shifting scenario. These kind of variations in spin modulations over a beat cycle weakens the power at spin frequency in the NuSTAR power spectra (both 3-10 and 10-40 keV energy band), derived from more than a beat-period long lightcurve. In pole switching case the power at the frequency peak can be shifted from ω to Ω and $2\omega - \Omega$ approximately equally (Littlefield et al., 2019). But in the NuSTAR power spectra we notice the $2\omega - \Omega$ peak is even weaker than ω. Therefore, for a pole switching scenario, if some power is transferred from ω to Ω in the NuSTAR power spectra, then that power shouldn't be of substantial amount. It indicates that the strong orbital frequency peak is a distinguishing feature for Paloma, irrespective of weaker spin frequency peak. However, this is not commonplace in IPs, for e.g in a systematic study of several IPs by Parker et al. (2005), orbital peaks appear to be weaker than or comparable with spin peaks.

4.4.2   Nature of the intrinsic absorber and the variation with orbital phase

The inherently complex nature of the intrinsic absorber is supported from spectral analysis. The simplistic scenario, implemented using two multiplicative partial covering model components as described by model M1, mathematically represents intrinsic inhomogeneous absorbers with at least three distinct column densities with their respective fractional contribution. From the fit to the phase averaged spectra, we calculate three such column densities as $2.2 \times 10^{22} cm^{-2}$, $20.0 \times 10^{22} cm^{-2}$ and $22.2 \times 10^{22} cm^{-2}$ appearing

with fractional contribution of $0.30, 0.18$, and 0.35 (following Eqn. 4.1). We can phys-
ically explain this as the X-ray emission encounters the intrinsic absorbers which are
mentioned in earlier susbection (Sect. 4.4.1). These absorbers are inhomogenous and do
not have a unique column density rather a distribution of column densities. This scenario
is supported by model M2 and M3, where we assume power law distribution of the col-
umn densities of the intrinsic absorber. The maximum values of the column density are,
$\sim 28 \times 10^{22} \ cm^{-2}$, consistent with model M1.

During orbital phase (a), the high value of the covering fractions for model M1, or
high values of the power law indices (β) of the complex absorber for model M2, M3 agree
with the sharp dip that we see in the folded lightcurve. This sharp excess in absorption is
contributed when a large part of emission encounters the absorber. During the other two
phases (b) and (d), we obtain similar value of covering fraction (model M1) or the β of
the complex absorber (model M2 and M3). This indicates the situation while lesser and
lesser amount of emission pass through the absorber, as the system rotates and during
phase (c), the least value of the covering fractions (model M1) or β (model M2 and M3)
are obtained.

4.4.3 Iron K_α lines and Compton reflection

The XMM-Newton EPIC spectra in Fig 4.5 presents three Fe K_α line complex, where
the He-like Fe K_α line appear with maximum strength (equivalent width 182^{+28}_{-23}eV), and
the neutral line is the weakest one (equivalent width 66^{+30}_{-18}eV). All the three lines are
narrow, with line width being consistent with instrument resolution.

The contribution of the neutral Fe K_α line comes from both the intrinsic absorber, as
well as from the Compton reflection of the X-rays from the WD surface (Ezuka & Ishida,
1999). A strong and complex absorber, with a weak neutral Fe K_α line suggests that
the absorber is likely to be the main contributor for the strength of this line for Paloma,
however, there is a possibility that some amount is contributed via Compton reflection.

In the broadband fitting, The "`reflect`" versions of the models (i.e M1-R, M2-R, M3-
R) display small improvement in fit-statistic. This suggests that reflection is weak in the
source.

In order to check the degree of degeneracy between absorption and reflection, we
plotted (Fig. 4.8) the model spectra (using best-fit values of parameters of M1-R fit,
obtained in Table 4.3) when both of the absorption and reflection are present and when
either one of them is absent. This plot shows that the strong intrinsic absorber in Paloma
have effect well around 15 keV (where black and blue curves merge) whereas, the lower
end of the reflection hump tail is comfortably extended till 7 keV (where red and blue
curves merge). It indicates the degeneracy of the reflection and absorption in this energy
range, which can be eliminated by securely detecting the reflection hump beyond 15
keV. The model spectra show a reflection hump feature in 10-30 keV which we could not
robustly detect it in the observed spectra as the improvement in fit-statistics is minimal.
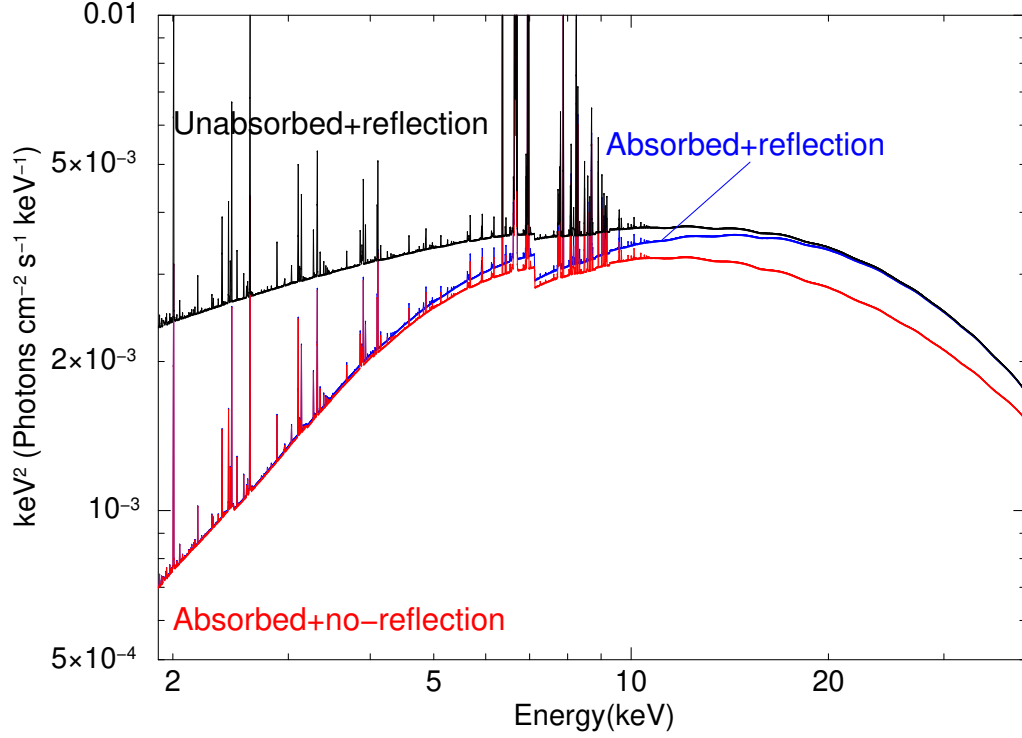
Figure 4.8: Effect of complex absorber and Compton reflection in the spectral modelling. Spectral parameters from model M1-R have been used. The blue curve represents the model spectrum including both reflection and absorption. For the black curve, the absorption is set to zero, but reflection is present. The red curve denotes the spectra when absorption is present but reflection is not.

To be noted, Mukai et al. (2015) have detected strong reflections in IPs. So, reflection in IPs is an important physical process and can be studied in detail provided the spectral quality is such that the detection is robust.

The reflection amplitude ($\Omega/2\pi$) physically denotes the shock height (h) over the surface the WD. Theoretically, reflection amplitude of 1 denotes the shock is happening just over the WD surface whereas a reflection amplitude 0 denotes a tall shock (Mukai, 2017). If we consider that there is certain contribution of Compton reflection in Paloma, though we agree that the statistical improvement to fit is small, we obtain physically acceptable values of the reflection amplitudes $\sim$ 0.39, 0.47 and 0.26 from models M1-R, M2-R and M3-R respectively. These values are much less than the value calculated by Joshi et al. (2016) ($\sim$ 2.4) using XMM-Newton only data. However, remembering the large statistical uncertainty associated with $\Omega/2\pi$ for any of our model variants, we refrain from deducing quantitative information, like value of the shock-height, based on that.

4.4.4   Case of Collisionally excited plasma and photoionised absorber

The RGS spectra shows signature of a strong O-VII line. Due to the poor quality of the data, we could not detect any other lines with statistical significance. Agreeing with RGS

spectra, the ionised oxygen line also appears as a small hump around 0.57 keV in the EPIC spectra, and other features in the soft X-rays. These soft X-rays features are not properly taken care by the cooling flow component, for which we modelled (model M1 and M2) them after an extra optically thin collisionally ionised plasma emission component. The temperature of this component signifies that this emission is coming from the base of the PSR.

As an alternative scenario, the photoionised warm absorber describes the soft X-ray features without the necessity of extra collisionally excited emission. Using Chandra grating data, Islam & Mukai (2021) has shown the presnece of photoionised pre-shock flow for two IPs (V1223 Sgr and NY Lup). Ionisation parameter ($\xi = L/nr^2$) is defined as a ratio of ionisation flux to ionisation density where emission with flux L/r^2 (modulo 4π) ionises the cloud of density n at distance r. This parameter is independent of the specific mass accretion rate. The 4π factor denotes the geometrical effect for an extended cloud covering an extended source. Geometrical effects can reduce the value of the ionisation parameter significantly. Based on the photoionised warm absorber model developed by Islam & Mukai (2021), we modelled our spectra using model M3, and found a similarly good fit in comparison with model M1 and M2. The phase resolved spectral fitting using model M3 gives consistent values of ionisation parameter for phases (a), (c), and (d) within statistical uncertainty. The low value for this parameter (~ -1.3) during the phase of the lowest covering fraction of complex absorber, i.e (c), is because of the geometrical effects, like the orientation and fraction of the absorber available to be ionised.

At this point, within the limited resolution of EPIC spectra and poor signal to noise ratio of RGS data, the two scenarios - presence of photoionised absorption by warm pre-shock flow; and neutral absorber with extra collisionally ionised emission from bottom of PSR, seem equally plausible from statistical perspective. A high quality grating data will reveal ionised emissions as well as absorption edges, which are important for securing the presence of a complex warm absorber.

4.4.5   White dwarf mass

The upper temperature of the cooling flow model represents the shock temperature, i.e the temperature of the shock-front on the top of the PSR. For all three model variants (M1, M2 and M3), the values of this parameter are mutually consistent with each other and well-constrained. Assuming the shock temperature ($31.7^{+3.3}_{-3.5}$ keV) from model M3 (minimum value of reduced χ^2), we estimate a WD mass of $M_{\mathrm{WD}} = 0.74^{+0.04}_{-0.05} M_\odot$ and a WD radius of $R_{\mathrm{WD}} = 7.4^{+0.4}_{-0.3} \times 10^8$ cm. We have used WD mass-radius relationship from Nauenberg (1972), and the formula for shock temperature with WD mass and radius (for eg. Mukai (2017)). Since, this value is measured from the shock temperature, obtained using broadband spectra, it is expected to give a fine estimate of the WD mass. However, for a negligible value of reflection amplitude, indicating a tall shock height, this mass can be somewhat underestimated (Lopes de Oliveira & Mukai, 2019).

The unabsorbed flux in 0.3-40.0 keV range is $F = 2.11^{+0.08}_{-0.07} \times 10^{-11}\ erg\ cm^{-2}\ s^{-1}$, of which $\sim 33\%$ is contributed from 10-40 keV band. The corresponding luminosity (0.3-40.0 keV) is $\sim 8.44 \times 10^{32}\ erg s^{-1}$, where distance to the source, $d = 578 pc$ (Gaia Collaboration et al., 2018).

Accretion luminosity can be represented in terms of the mass accretion rate ($\dot{M}$) as (Frank et al., 2002)

$$L_{acce} = \frac{GM_{\mathrm{WD}}\dot{M}}{R_{\mathrm{WD}}}$$

Using our obtained values of luminosity, mass, and radius of the WD, we calculate $\dot{M} \sim 6.33 \times 10^{15}\ gs^{-1} \sim 9.98 \times 10^{-11} M_\odot yr^{-1}$. This value is in line with the $M_\odot$ seen for other asynchronous polars; for eg. - V1432 Aql: $\sim 3 \times 10^{15}\ gs^{-1}$ (Rana et al., 2005); CD Ind: $\sim 8 \times 10^{14}\ gs^{-1}$ (Dutta & Rana, 2022a); V1500 Cyg: $\sim 6 \times 10^{14}\ gs^{-1}$ (Harrison & Campbell, 2016), and BY Cam: $\sim 6 \times 10^{16}\ gs^{-1}$ (Done & Magdziarz, 1998).

4.4.6   Possibility of formation of Disc

Past studies of Paloma (Schwarz et al., 2007; Littlefield et al., 2022) have favoured a disc-less scenario mainly based on the presence of $2\omega - \Omega$ peak (Wynn & King, 1992) in their periodgram obtained from photometric observation. We also notice the presence of $2\omega - \Omega$ peak in the FPMA Lomb-Scargle power spectra (Fig 4.2), but that peak is much weaker compared to Ω peak and also suppressed in CELANed power spectra. However, the power spectra presented in Figures 2 and 3 show presence of $\Omega + 2\omega$ peak which appears with relatively higher power in power spectra of both the telescopes, and in Lomb-Scargle as well as CLEANed algorithm. This frequency peak is among the set of frequency peaks, which can be produced in a purely disc-fed system with asymmetric dipole condition and additional orbital modulations (like stream-disc impact) scenario (Norton et al., 1996). There are other expected frequency peaks for this scenario, for eg. $\omega + \Omega$ is noticed in the FPMA power spectra (but unresolved in PN power spectra). Surprisingly, the expected lower orbital sideband counterpart $\omega - \Omega$ is not noticed in the FPMA power spectra (PN power spectra is anyway unable to detect it due to smaller duration of lightcurve), and the spin harmonic 2ω and its lower orbital sideband $2\omega - \Omega$ appear with small power in the FPMA Lomb-Scargle power spectra. Therefore, it is difficult to conclusively argue for disc-fed or disc-less system, as evidenced from our power spectra. Another alternate argument for the formation of disc could be made by comparing the magnetospheric radius with the other binary parameters (circularisation radius, distance of closest approach of free fall stream). Unfortunately, we could not do so because of the unavailability of the measured magnetic fields of the WD in Paloma, as of now.

5

A broadband X-ray study of the dwarf nova SS Cyg during quiescence and outburst

Abstract: *We present a broadband X-ray study ($\sim$ 0.3-50 keV) of the dwarf nova SS Cyg highlighting the changes in the accretion during two phases, the quiescence and the outburst states. The investigation was based on simultaneous observations carried out with the XMM-Newton and NuSTAR telescopes in two epochs, involving medium and high-resolution spectroscopy. Spectra were harder during quiescence ($kT_{\rm high} \sim$ 22.8 keV) than outburst ($kT_{\rm high} \sim$ 8.4 keV), while the mass accretion rate increased by $\sim$ 35 times in outburst (1.7×10^{16}g s^{-1}) than quiescence. The bolometric luminosity (0.01-100.0 keV) during the outburst was dominated by a blackbody emission ($kT_{\rm BB} \sim$ 28 eV) from the optically thick boundary layer, and the inner edge of the accretion disk resides very close to the WD surface. X-rays from the accretion disk boundary layer are consistent with the white dwarf having mass $1.18^{+0.02}_{-0.01}$M$_\odot$. Our study conclusively confirms the presence of the reflection hump in the 10-30 keV range for both phases, which arises when X-ray photons hit colder material and undergo Compton scattering. We estimated a similarly strong reflection amplitude during quiescence ($\sim$ 1.25) and outburst ($\sim$ 1.31), indicating both the WD surface and disk are contributing to reflection. The neutral Fe K$_\alpha$ line, which is correlated with Compton reflection, also showed similar strength ($\sim$ 80 eV) in both phases. Finally, X-rays also revealed the presence of a partial intrinsic absorber during the outburst, possibly due to an outflowing accretion disk wind.*

5.1 Introduction

SS Cyg, one of brightest CV in the sky and a popular dwarf nova with WD mass (M_{WD}) $1.19 \pm 0.02 M_\odot$, secondary mass (M_K) $0.704 \pm 0.002 M_\odot$ (Friend et al., 1990) ($M_{WD} = 0.81 \pm 0.19 M_\odot$ and $M_K = 0.55 \pm 0.13 M_\odot$ (Bitner et al., 2007)), binary inclination angle $37° \pm 5°$ and orbital period 6.603 hrs (Shafter, 1983; Hessman et al., 1984; Bitner et al., 2007; Miller-Jones et al., 2013), has been subject to multiple studies in X-rays (Ginga and ASCA (Done & Osborne, 1997), RXTE (McGowan et al., 2004), ASCA (Baskill et al., 2005) and Suzaku (Ishida et al., 2009), NICER and NuSTAR (Kimura et al., 2021)). The studies by Done & Osborne (1997); Ishida et al. (2009); Kimura et al. (2021) of SS Cyg showed the presence of significant Compton reflection during both states. However, these studies have limitations arising from data quality or physical interpretation.

Now, using the simultaneous data from XMM-Newton, having good energy resolution, and NuSTAR, having high sensitivity in hard X-rays and with excellent cross-calibration between these two telescopes, we analysed the broadband spectra of SS Cyg during both the quiescence and outburst phases. We model the multi-temperature continuum with plasma emission components and incorporate the contribution from the iron line complex, the soft X-ray features, absorption, and directly measuring Compton reflection. We aim to address the questions like how the accretion and nature of the X-ray emitting plasma changes between two phases and what are the possible reflection sites in either of the two phases.

In this paper, we have described the observation and data reduction in Section 5.2 , the analysis and the results in Section 5.3, the discussion in Section 5.4.

5.2 Observation and Data Reduction

SS Cyg was observed simultaneously (see Table 5.1, PI: Vikram Rana) with XMM-Newton (Jansen et al., 2001) and NuSTAR telescopes (Harrison et al., 2013) in both of its quiescence and outburst phases. Fig. 5.1 shows the X-ray observational period of XMM-Newton and NuSTAR during quiescence and outburst along with an optical lightcurve from the American Association of Variable Star Observers (AAVSO). The observation was made to secure the broadband spectra extending from 0.3 keV to 79.0 keV of the X-ray energy band. The good energy resolution of XMM-Newton EPIC (European Photon Imaging Camera) detectors (Strüder et al., 2001; Turner et al., 2001) in the low energy band (0.3-10.0 keV), employed with high sensitivity of NuSTAR-FPM detectors in high energy band (staring from 3.0 keV and extending up to 79.0 keV), offer an excellent quality data for analysis. The high-resolution reflection grating spectrometer, RGS (den Herder et al., 2001), onboard XMM, provides spectra in the 0.35-2.5 keV energy band, resolving the prominent emission lines produced in the source.
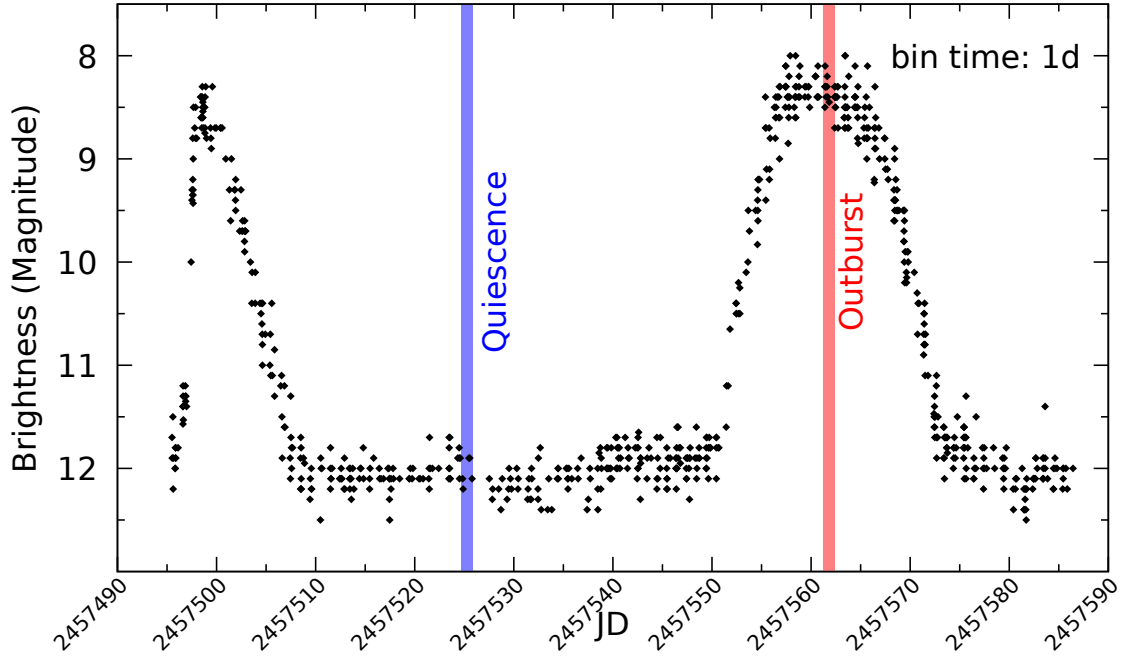
Figure 5.1: Optical lightcurve of SS Cyg in visual band (Source: AAVSO). The epoch of simultaneous NuSTAR and XMM-Newton observations during quiescence and outburst are marked.

ccccc

Table 5.1: Observation log of SS Cyg

State	Telescope	Obs ID	Obs Date & Time	Exposure (s)
Quiescence	XMM-Newton	0791000201	2016-05-16 & 07:18:26	30000
	NuSTAR	80202036002	2016-05-16 & 06:26:08	49789
Outburst	XMM-Newton	0791000101	2016-06-21 & 18:08:10	36000
	NuSTAR	80202036004	2016-06-21 & 17:11:08	52161

5.2.1   NuSTAR

The two focusing imaging telescope modules of NuSTAR, FPMA and FPMB, capable of focusing hard X-rays (3.0-79.0 keV) with very high sensitivity, observed the source. These two telescopes of Wolter-I configuration employ grazing incidence mirrors to bring the X-rays to their focus. Each of the telescope modules is equipped with one detector module, which comprises 4 CZT-detectors. We have selected a 50 arcsec radius circular region to include the source. The 100 arcsec radius circular background region (in the same CZT detector as that of the source) has been selected to extract the background subtracted source data. There are no other X-ray emitting sources present in that detector. The NuSTAR data is devoid of any pile-up issues, thanks to its use of CZT detectors. We have used NuSTARDAS v2.1.2 along with NuSTAR calibration files v20221229 for data calibration, screening and science-products extraction. The default screening criteria for

attitude, dead time, orbit and instrument parameters are used to obtain science data products, like the spectra and detector response files. The spectra from each telescope module have been rebinned using `grppha` to a minimum of 25 counts per bin to utilize χ^2 minimization for spectral fitting. For spectral analysis involving NuSTAR data, both the FPMA and FPMB spectra are used to improve the signal-to-noise ratio.

5.2.2   XMM-Newton

The XMM-Newton satellite consists of three X-ray telescopes. The EPIC-PN detector is placed behind one telescope, receiving X-ray photons with PN-CCD arrays. The EPIC-MOS detectors are two in number and utilize other telescopes for receiving the X-ray photons using Metal Oxide Semiconductor CCD arrays. These three EPIC detectors (one PN, two MOS) have been used to observe the source in 0.3-10.0 keV energy band. The two telescopes, working for MOS1 and MOS2, are also equipped with two grating spectrometers, RGS1 and RGS2. Nearly half of the X-ray flux received by those two telescopes are sent to MOS detectors whereas, other half is used by the RGS. We have used the first order spectra from the grating spectroscope, which can resolve emission and absorption lines in 0.35-2.5 keV band (5-38 Å), comprising the important K_α transition from ionised C, N, O, Ne, Mg, Si elements as well as Fe L-Shell emission lines.

We have used XMMSAS (Gabriel et al., 2004) software (version 20.0.0) for data reduction and extracting science products like the spectra and the detector response files. For the latest calibration files, we have used XMMSAS ccf repository [1]. The observation was taken in Small Window mode for both PN and MOS detectors. Since SS Cyg is a fairly bright source, we have checked for pile-up in all three detectors using the epatplot tool. We have found that the outburst phase data suffers from pile-up, most strongly in PN. The pile-up effect has been reduced by selecting annular regions to include the source. Since the central core pixels contain maximum counts, thus having maximum impact on pile-up, we have excised those pixels to eliminate the pile-up issue. Running some trials on the annular region size, we have finalized on (15,30) arcsec radii annular region for source selection (for PN, MOS1, MOS2), which minimizes the pile-up without sacrificing the number of counts too much. The background is selected from a circular region in the same CCD as that source, with a radius of 40 arcsec (for PN, MOS1, MOS2). However, since RGS detectors get only 50% of the received flux, the pile-up is not noticeable in the RGS data of the outburst phase. This has been cross-checked by comparing the RGS 1st order and 2nd-order spectra. We have checked the quiescence phase data from EPIC and RGS detectors for pile-up, and we didn't notice a significant pile-up there. However, to have a conservative approach, we performed the core-excising technique for the quiescence phase data from EPIC (PN, MOS1, MOS2) detectors as well – by choosing an annular region of (15,30) arcsec radii for the source and selected a circular background region of 40 arcsec radius in the same CCD as that of the source. The pile-up correction

---

[1] https://www.cosmos.esa.int/web/xmm-newton/current-calibration-files

is done following the SAS analysis thread (for EPIC [2] and for RGS [3]).

We have also checked for any high background flares present in the data, occurring due to unpredictable solar soft protons. Fortunately, our data does not include any such flaring backgrounds. After employing the necessary selection criteria, we screened and reduced the final science products eg. the spectra and the detector response files. We have applied corrections to the effective area to remove residuals between simultaneous fits of EPIC and NuSTAR observations by applying the command `applyabsfluxcorr=yes` with the tool `arfgen`. The spectral data from all the detectors have been re-binned using `specgroup` to minimum counts of 25 and the oversample parameter of 3.

5.3 Data Analysis and Results

In this section, we describe the spectral analysis of the data, performed using XSPEC v12.12.1 (Arnaud, 1996). First, we discuss the analysis of the data obtained during the quiescence phase from NuSTAR and XMM-Newton separately and proceed to simultaneous broadband fitting. Next, we discuss the same for the observations during the outburst. Here, we want to mention that while both XMM observations were carried out entirely with the time interval covered by the respective NuSTAR observations, the latter have data gaps and cover longer periods. We have also analyzed strictly simultaneous portion of the data and confirm that this did not unduly influence our results. This appears to be because the random varaibility within these observing periods largely averaged out. The only minor exception is in the cross-normalization factor for NuSTAR data for the quiescence observation: the flux was somewhat higher during the first half (with XMM overlap) than during the second half (without). Even so, we do not observe any statistically significant changes in the best-fit model parameters.

The spectral models used in this work are part of the XSPEC: `mkcflow` (after Mushotzky & Szymkowiak, 1988), a multi-temperature model assuming cooling flow from a hot optically thin plasma to account for the primary X-ray emission arising from the boundary layer; `reflect` (Magdziarz & Zdziarski, 1995), describing Compton hump expected by reflection; `tabs` (Wilms et al., 2000), responding for the photoelectric absorption features of the ISM and local absorbers, eventually associated to the `partcov` model to partial coverage; `bbody` to consider the soft X-ray emission from optically thick boundary layer during outburst; `gaussian` to describe the iron fluorescence line at 6.4 keV; and `constant` to accommodate and evaluate cross-correlation issues between XMM-Newton and NuSTAR cameras We have set the abundance table as Wilms (Wilms et al., 2000) and chosen the Verner photo-electric absorption cross-section (Verner et al., 1996). As for the `mkcflow` model, the switch parameter was set to 2 to follow the AtomDB database and the redshift parameter was fixed at 2.67×10^{-8} – corresponding to the GAIA DR2 distance to SS Cyg

---

[2]https://www.cosmos.esa.int/web/xmm-newton/sas-thread-epatplot
[3]https://www.cosmos.esa.int/web/xmm-newton/sas-thread-pile-up-in-the-rgs

adopted in this work, of 114.62 pc (Gaia Collaboration et al., 2018).[4] The model flux has been calculated using `cflux` component from the broadband models. We have extended the range of energy response for all spectral groups in the range 0.01 keV-100.0 keV using `energies extend` command.

5.3.1   Quiescence Phase

First, we have looked into the NuSTAR spectra to get an idea of the hard X-ray properties of SS Cyg in quiescence. The data are used in the 3.0-50.0 keV band since photon counts are very low above 50.0 keV and dominated by background. The multi-temperature emission from hot optically thin plasma of the boundary layer has been modelled using cooling flow component `mkcflow`. The lower temperature of this component is fixed at the lowest value allowed, 0.0808 keV, since it is closer to the expected lower temperature of the boundary layer plasma while not constrained from the data. The ISM absorption is incorporated using `tbabs`. Since the NuSTAR data cannot constrain the column density of the ISM, which influences the spectra below a few hundred of eV, we have fixed its value at $3.5 \times 10^{19}\ cm^{-2}$ (Mauche et al., 1988). We have kept the abundance of the cooling flow model free, to reproduce the necessary strength of Fe H-like and He-like K_α emission lines. We introduce a narrow `gaussian` ($\sigma = 0$ eV) for the neutral Fe K_α line. The resultant best-fit ($\chi^2/DOF = 719/657$) returns a upper temperature of ~ 33 keV. However, excess residual for the Compton reflection hump in the hard X-rays ($\sim 10 - 30$ keV) is evident, and we convolve the `reflect` component with the plasma emission component to consider Compton reflection. Since the possible reflection sites are regions of white dwarf surface which has freshly accreted material and/or the accretion disk surface, we can assume the same elemental abundance between the Compton reflection component and the plasma emission component. The viewing angle (i) of the reflection site is fixed at the default value ($\mu = cos\,i = 0.45$, which is the ensemble average of the viewing angles of the accreting binary systems) of the reflection component. The final best-fit model ($\chi^2/DOF = 666/657$) gives upper temperature $21.3^{+1.5}_{-1.3}$ keV, which is in agreement with the finding of Done & Osborne (1997) ($21.0^{+11.0}_{-5.7}$ keV) and Ishida et al. (2009) ($20.4^{+4.0}_{-2.6}$ keV). The abundance comes out to be $0.53^{+0.09}_{-0.08}$ w.r.t solar. The reflection amplitude is obtained as $1.18^{+0.26}_{-0.25}$, validating the presence of reflection as noticed from the excess residual. However, this component may have degeneracy with a complex intrinsic absorber, which can affect even beyond 10 keV for a strong absorber (Fig. 8 of Dutta & Rana (2022b)), thereby, the measured value of reflection amplitude can change. Now, in order to probe the effect of the intrinsic absorber in the soft X-rays, we next perform the analysis of the XMM-Newton EPIC spectra.

For the XMM-Newton EPIC data (PN, MOS1, and MOS2), initially, we probed the

---

[4]We are aware of the geometric distance determined by Bailer-Jones et al. (2021) from GAIA data of $112.35^{+0.39}_{-0.35}$ pc, which is only 2% less than the adopted distance and as such has no impact on the results presented here.

spectra in 5-9 keV which include the Fe line complex in 6-7 keV. We have used an absorbed bremsstrahlung component to model the continuum and three Gaussian components for the neutral, H-like and He-like Fe K_α lines. The column density of the absorber is fixed at the literature value. The fit resulted in a fit-statistic of $\chi^2/DOF = 110/91$, and the best-fit parameters are quoted in Table 5.4. A spectral plot comparing three iron lines in quiescence and outburst phases are shown in Fig. 5.4. We noticed that the σ of all three lines are consistent with EPIC instrument resolution ($\Delta E \sim 120$ eV at ~ 6 keV), and the line widths could not be constrained, so fixed at zero. The line central energies appear at the theoretically expected values, within statistical uncertainty, and the strength of the neutral line is weaker (82^{+34}_{-30}eV) compared to the H-like (102^{+62}_{-31}eV) and He-like (131^{+46}_{-28}eV).

We next model the EPIC spectra in 0.3-10.0 keV energy range. The spectra are described with the cooling flow component (`mkcflow`) and an absorption component `tbabs`). The lower temperature is fixed at 0.0808 keV, whereas the upper temperature of the cooling flow component is kept free. We added one narrow Gaussian component for the neutral Fe line. The resultant fit statistics is $\chi^2/DOF = 530/417$. However, the column density is not constrained, and we obtained an upper limit of 5×10^{19} cm^{-2}. At this point, to probe the presence of the intrinsic absorber, we included a partial covering photo-electric absorption model (`partcov*tbabs`), and obtained an improved fit-statistic of $\chi^2/DOF = 511/415$. The covering fraction of the intrinsic absorber is $0.21^{+0.09}_{-0.07}$ with a column density of $4.2^{+2.7}_{-1.5} \times 10^{23}$ cm^{-2} indicating that the intrinsic absorber is quite strong. The overall absorber column density, which includes the ISM absorption along the line of sight, is now constrained ($8.8^{+5.1}_{-4.3} \times 10^{19}$ cm^{-2}). The upper temperature and the elemental abundance of the cooling flow component are found to be $30.7^{+3.8}_{-4.0}$ keV and $0.61^{+0.16}_{-0.15}$ as that of solar values, respectively.

Now, to check the effect of the reflection and degeneracy with the partial absorber, we introduced the Compton reflection component instead of the partial covering absorber. We obtained a similar fit statistic ($\chi^2/DOF = 514/416$), with a reflection amplitude of $1.07^{+0.32}_{-0.43}$. The parameter values of the other components are similar (within statistical uncertainty) to that of partial absorber fit. This points to the delicate degeneracy between the partial absorber and the reflection present in the modelling of the EPIC spectra.

In the final stage, guided by the individual modelling of the NuSTAR and EPIC spectra, we proceed towards jointly fitting the simultaneous spectra. Considering the possibility of an intrinsic absorber, we used two model variants - one including the partial absorber and another without it. In XSPEC notations the models are (Q1) `constant* tbabs* (partcov* tbabs)* (reflect* mkcflow+ gaussian)` and (Q2) `constant* tbabs* (reflect* mkcflow+ gaussian)`. The best-fit parameter values are quoted in Table 5.2 and the spectra are plotted in Fig. 5.2. In the first model, Q1, both the partial absorber and the Compton reflection are considered, where we obtain a reflection amplitude $0.40^{+0.47}_{-0.19}$ and intrinsic absorber column density of $2.6^{+1.2}_{-0.6} \times 10^{23}$ cm^{-2} with covering fraction of $0.16^{+0.05}_{-0.05}$.

For the second model, Q2, the reflection amplitude comes out to be $1.25^{+0.27}_{-0.20}$, which is close to the value obtained from individual EPIC or NuSTAR analysis when intrinsic absorber was not considered. All other parameter values agree within statistical confidence between the models Q1 and Q2. Also, the cross normalisation parameters for model Q2 are: $C_{MOS1}=1.02^{+0.01}_{-0.01}$, $C_{MOS2}=1.05^{+0.01}_{-0.01}$, $C_{FPMA}=1.13^{+0.02}_{-0.02}$, $C_{FPMB}=1.09^{+0.02}_{-0.02}$, while C_{PN} is fixed to 1.

At this point, we argue that, since statistically, both these models are equally acceptable, we need to favour one model over another based on physical considerations. This has been discussed in the Section 5.4.2.

5.3.2 Outburst Phase

The outburst NuSTAR spectra in the 3.0-40.0 keV range are fitted with the cooling flow model `mkcflow` and the ISM absorption model `tbabs`. We restrict the analysis to energies up to 40 keV, after which the background begins to dominate over source counts. We kept the lower temperature of the cooling flow model fixed at 0.0808 keV (for the same reasons explained in Section 5.3.1) and the column density of the ISM absorber at the literature value, not constrained from the data. We included a `gaussian` component with free sigma to consider the iron line complex in 6-7 keV, which appears to be a broad peak and could not be resolved by NuSTAR. The fit statistic is $\chi^2/DOF = 668/554$ with an upper temperature of $10.9^{+0.2}_{-0.2}$ keV, which is expected for the softer spectra in the outburst phase. For the Compton reflection hump, we next included the `reflect` component with its abundance linked to the cooling flow component, and viewing angle fixed at default value as mentioned in the quiescence phase analysis. We now obtain an improved fit statistic of $\chi^2/DOF = 650/553$, with reflection amplitude of $0.74^{+0.39}_{-0.31}$. The upper temperature is now $9.3^{+0.6}_{-0.6}$ keV, and the abundance is $0.43^{+0.09}_{-0.11}$ w.r.t solar values.

Next, we attempted fitting the iron line complex in 6-7 keV using the XMM-Newton EPIC spectra in the 5.0-9.0 keV range, as done for quiescence phase analysis. The best-fit parameters are quoted in Table 5.4. We notice that all line widths are consistent with the EPIC instrument resolution, and therefore σ was fixed at zero. The strength of the He-like Fe K_α line is maximum (263^{+43}_{-36}eV) among the three dominant lines. The neutral Fe K_α line has similar strength as that during the quiescence phase, whereas the He-like line is much stronger than quiescence. We notice the apparent blueshift ($6.46^{+0.03}_{-0.03}$ keV) of the neutral line. The reason behind is that the K shell lines from the lower ionisation states - Fe XVII through Fe XXII (which are certainly present, as the corresponding L-shell emissions are strongly detected in the RGS spectra of outburst phase, Fig. 5.5) - have intrinsic centroid around 6.5 keV, which are blended with the neutral line.

We then proceeded to model the entire EPIC spectra (PN, MOS1 and MOS2) in 0.3-10.0 keV. We introduced the cooling flow model to consider the emission from the multi-temperature boundary layer, along with the ISM absorption model. The lower temperature is fixed at 0.0808 keV and the ISM column density is at the literature value.

The fit statistic is extremely poor with $\chi^2/DOF = 6871/438$. We notice that outburst EPIC spectra are significantly complex with an evident signature of blackbody emission, which presents itself as excess in residual in soft X-ray below 0.5 keV. We added the blackbody component, which improved the fit statistic to $\chi^2/DOF = 4574/437$. There are multiple strong emission line features as expected during the outburst phase of a dwarf nova, like SS Cyg (Mauche, 2004; Okada et al., 2008). Though many lines can be resolved in RGS spectra (see Fig 5.5), EPIC only detect those as narrow or broad peaks in the soft X-rays below and around $\sim$ 2 keV. Therefore, we needed to carefully add multiple emissions components to bring down the fit statistic to an acceptable value. We introduced five Gaussian components to consider the line emission features and obtained an improved fit statistic of $\chi^2/DOF = 604/426$. Three narrow Gaussian components consider the emission features due to the O-VII line, Si lines and Mg lines. One broad Gaussian accounts for a strong O-VIII line and few neighbouring Fe L-shell emissions, and another broad Gaussian incorporates Ne-lines. At this stage, we include the partial covering component (`partcov*tbabs`) to probe the presence of the complex intrinsic absorber. The improved fit statistic is now $\chi^2/DOF = 581/421$, with a column density of the intrinsic absorber 3.2×10^{22} cm^{-2} and covering fraction of $0.14^{+0.04}_{-0.04}$.

After receiving the clues regarding model components from analysing individual EPIC and NuSTAR spectra, we attempted simultaneous broadband spectral modelling. In XSPEC notation, our model is `constant* tbabs* (partcov* tbabs)* (reflect* mkcflow+ gauss+ gauss+ gauss+ gauss+ gauss+ gauss+ bbody)`. The fit statistic comes out to be $\chi^2/DOF = 1257/979$ and best-fit parameter values are quoted in Table 5.3. The spectra are plotted in Fig. 5.3 The fit statistic is acceptable for the purpose of our study, where we focus on obtaining the overall description of the continuum. The cross normalisation parameters are: $C_{MOS1}=1.04^{+0.01}_{-0.01}$, $C_{MOS2}=1.11^{+0.01}_{-0.01}$, $C_{FPMA}=1.21^{+0.02}_{-0.02}$, $C_{FPMB}=1.18^{+0.02}_{-0.01}$, while C_{PN} is fixed to 1. In this broadband modelling, we considered similar five Gaussian components, as that of EPIC only fit, to consider the excess residual due to line emission features in soft X-rays. The strong blackbody emission is also modelled in the broadband spectra. The reflection amplitude is constrained at $1.31^{+0.30}_{-0.30}$. The abundance ($0.51^{+0.03}_{-0.02}$) is statistically consistent with the corresponding value of that parameter during quiescence. We have also checked that fitting the broadband quiescence and outburst data together with a tied abundance value recovers, to within statistical uncertainties, the results from individual broadband fits, in terms of all the parameters including the abundance ($0.46^{+0.06}_{-0.01}$) and the reflection amplitudes ($1.18^{+0.13}_{-0.12}$ in quiescence and $1.49^{+0.17}_{-0.24}$ in outburst). We could not constrain the overall absorber column density, whose fit value was reaching the lowest limit allowed for that component; so was fixed at the ISM column density from the literature. The intrinsic absorber is evidently required in our fitting, which if not considered, produces a much worse fit statistic of $\chi^2/DOF = 1358/980$ along with an unphysically high value of reflection amplitude ($\sim$ 2.5). The upper temperature

Table 5.2: Best-fit parameter values from quiescence joint XMM-EPIC and NuSTAR fit (0.3-50.0 keV)

Parameters	Unit	$Q_1^{\dagger c}$	$Q_2^{\dagger d}$
nH_{tb}	$10^{19} cm^{-2}$	$12.5^{+4.0}_{-2.2}$	$15.8^{+2.8}_{-2.7}$
nH_{pcf}	$10^{22} cm^{-2}$	$25.7^{+11.9}_{-5.8}$	
pcf		$0.16^{+0.05}_{-0.05}$	
T_{low}	keV	0.0808_f	0.0808_f
T_{high}	keV	$25.9^{+1.1}_{-2.3}$	$22.8^{+1.5}_{-1.1}$
$N_C^{\dagger a}$	10^{-11}	$1.46^{+0.13}_{-0.06}$	$1.32^{+0.05}_{-0.04}$
Z	$Z_\odot$	$0.56^{+0.04}_{-0.13}$	$0.44^{+0.06}_{-0.04}$
rel_{refl}		$0.40^{+0.47}_{-0.19}$	$1.25^{+0.27}_{-0.20}$
E_L	keV	$6.40^{+0.04}_{-0.02}$	$6.42^{+0.02}_{-0.04}$
σ	eV	0_f	0_f
$N_L^{\dagger b}$		$2.5^{+0.4}_{-0.4}$	$2.4^{+0.4}_{-0.4}$
χ^2/DOF		1189/1076	1202/1078

$\dagger a$: Norm of MCKFLOW (in $M_\odot\ yr^{-1}$)

$\dagger b$: Norm of Gaussian (in total $photons\ cm^{-2}\ s^{-1}$)

$\dagger c$: Best-fit model using partial absorber and Compton reflection.

$\dagger d$: Best-fit model using Compton reflection. The model description is in the text.

of the cooling flow component is ∼ 8.4 keV, less than the quiescence phase (temperature ∼ 22.8 keV), indicating softer spectra during the outburst.

5.3.3   High resolution RGS spectra during quiescence and outburst Phase

To verify the line emission features that appeared in the soft X-rays obtained from EPIC, we further checked the RGS spectra. The RGS spectra in 0.35-2.5 keV range for both phases are shown in Fig. 5.5. We notice that during the quiescence phase, the O-VIII line appears to be the strongest with other weak emission lines. During the outburst, multiple strong emission lines are present, including K_α lines of highly ionised states of several low Z elements, e.g., C, N, O, Ne, Mg, Si, and Fe L shell emissions. However, given the complexity involved in modelling the line emissions from the dwarf nova systems, particularly in the outburst phase, we did not attempt robust modelling of the RGS spectra, which is out of scope for this work.

5.4   Discussion

5.4.1   Quiescence vs Outburst X-ray : Hard vs Soft

In dwarf novae systems like SS Cyg, where the material is accreted via an accretion disk, the kinetic energy of the accreting material in the boundary layer is equal to half of
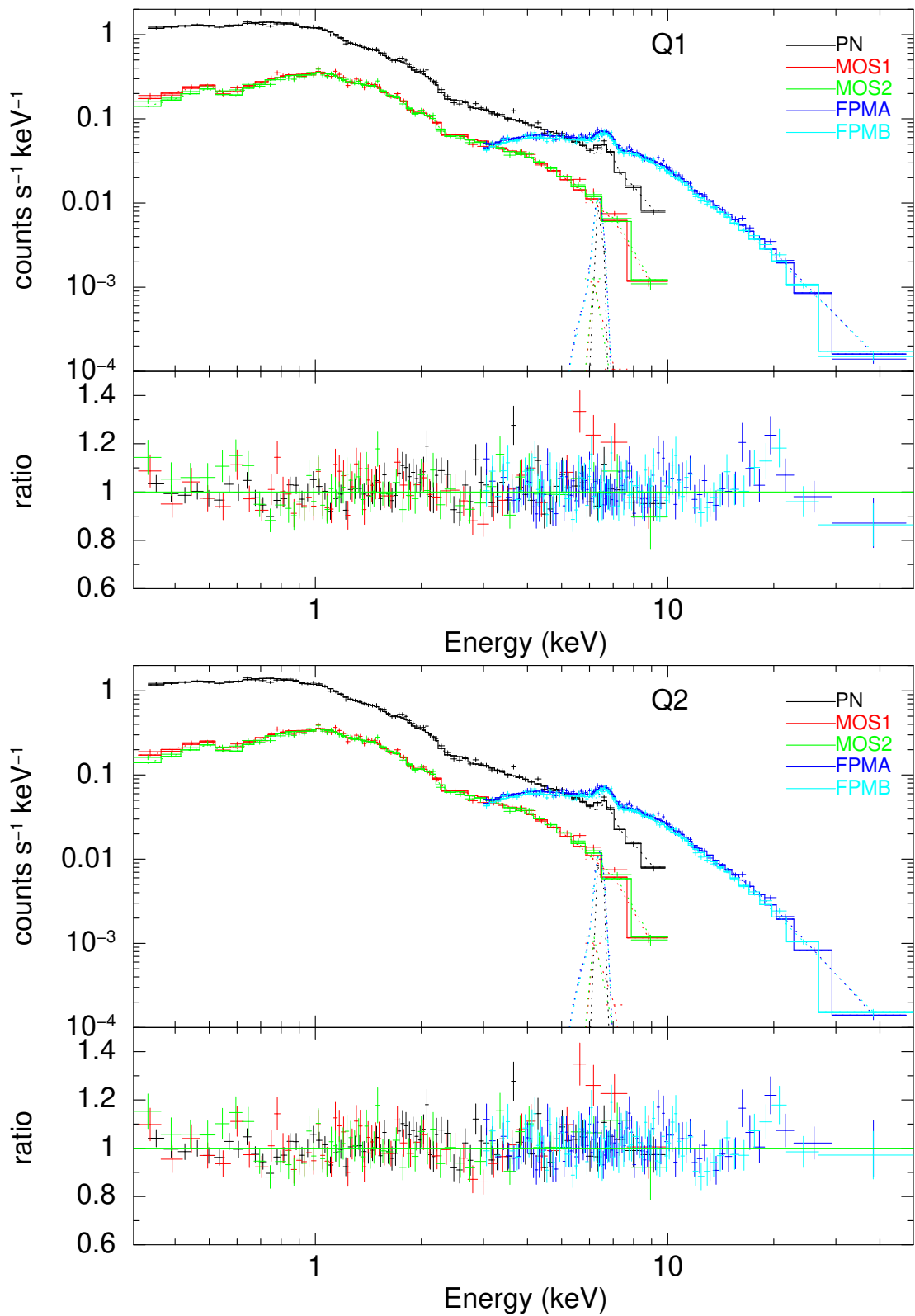
Figure 5.2: Spectrum and ratio (data/model) plot of the quiescence phase joint XMM-EPIC and NuSTAR data including partial covering absorber and Compton reflection, model Q1 (top) and including only the Compton reflection component, model Q2 (bottom)

Table 5.3: Best-fit parameter values from joint outburst XMM-EPIC and NuSTAR fit (0.3-40.0 keV)

Parameters	Unit	Values
nH_{tb}	$10^{19} cm^{-2}$	3.5_f
nH_{pcf}	$10^{22} cm^{-2}$	$3.4^{+1.0}_{-0.9}$
pcf		$0.23^{+0.02}_{-0.02}$
rel_{refl}		$1.31^{+0.30}_{-0.30}$
T_{BB}	eV	$27.9^{+1.2}_{-1.7}$
$N_{BB}^{\dagger a}$	10^{-3}	$24.2^{+18.1}_{-7.2}$
T_{low}	keV	0.0808_f
T_{high}	keV	$8.4^{+0.3}_{-0.3}$
$N_C^{\dagger b}$	10^{-11}	$5.2^{+0.1}_{-0.1}$
Z	$Z_\odot$	$0.51^{+0.03}_{-0.02}$
E_1	keV	$0.563^{+0.006}_{-0.002}$
σ_1	eV	0_f
$N_1^{\dagger c}$	10^{-3}	$2.1^{+0.1}_{-0.2}$
E_2	keV	$0.647^{+0.016}_{-0.029}$
σ_2	eV	135^{+32}_{-19}
$N_2^{\dagger c}$	10^{-3}	$3.3^{+1.0}_{-0.4}$
E_3	keV	$1.89^{+0.01}_{-0.01}$
σ_3	eV	0_f
$N_3^{\dagger c}$	10^{-3}	$6.8^{+1.6}_{-1.6}$
E_4	keV	$1.34^{+0.01}_{-0.01}$
σ_4	eV	0_f
$N_4^{\dagger c}$	10^{-3}	$7.6^{+1.8}_{-1.8}$
E_5	keV	$0.958^{+0.015}_{-0.016}$
σ_5	eV	58^{+15}_{-14}
$N_5^{\dagger c}$	10^{-3}	$0.6^{+0.2}_{-0.2}$
E_L	keV	$6.44^{+0.01}_{-0.01}$
σ	eV	0_f
$N_L^{\dagger d}$	10^{-5}	$4.2^{+0.5}_{-0.4}$
χ^2/DOF		1257/979

$\dagger a$: Norm of blackbody (L_{39}/D_{10}^2 where L_{39} is in 10^{39} erg s^{-1} and D_{10} is in 10 kpc

$\dagger b$: Norm of MCKFLOW (in $M_\odot\ yr^{-1}$)

$\dagger c$: Norm of Gaussian (in $photons\ cm^{-2}\ s^{-1}$) components, added for the considering the soft X-ray emission features.

$\dagger d$: Norm of gaussian (in $photons\ cm^{-2}\ s^{-1}$)

Table 5.4: Iron line comparison from outburst and quiescence XMM-EPIC data in 5-9 keV

	Parameters	Unit	Quiescence	Outburst
	nH_{tb}	$10^{19}cm^{-2}$	3.5_f	3.5_f
	T_{Brems}	keV	$11.6^{+5.6}_{-3.0}$	$7.1^{+1.7}_{-0.5}$
Neutral	E_L	keV	$6.42^{+0.03}_{-0.03}$	$6.46^{+0.03}_{-0.03}$
line	σ	eV	0_f	0_f
	eqw	eV	82^{+34}_{-30}	81^{+23}_{-22}
	$N_L^{\dagger a}$	10^{-5}	$2.4^{+0.8}_{-0.8}$	$3.0^{+1.1}_{-0.5}$
He-like	E_L	keV	$6.68^{+0.03}_{-0.02}$	$6.69^{+0.01}_{-0.01}$
line	σ	eV	0_f	0_f
	eqw	eV	131^{+46}_{-28}	263^{+42}_{-33}
	$N_L^{\dagger a}$	10^{-5}	$3.7^{+0.9}_{-0.8}$	$8.4^{+1.1}_{-1.0}$
H-like	E_L	keV	$6.99^{+0.03}_{-0.03}$	$6.93^{+0.03}_{-0.02}$
line	σ	eV	0_f	0_f
	eqw	eV	102^{+62}_{-31}	86^{+36}_{-28}
	$N_L^{\dagger a}$	10^{-5}	$2.5^{+0.8}_{-0.9}$	$2.8^{+0.8}_{-0.7}$
	χ^2/DOF		110/91	118/97

$\dagger a$: Norm of gaussian (in $photons\ cm^{-2}\ s^{-1}$)
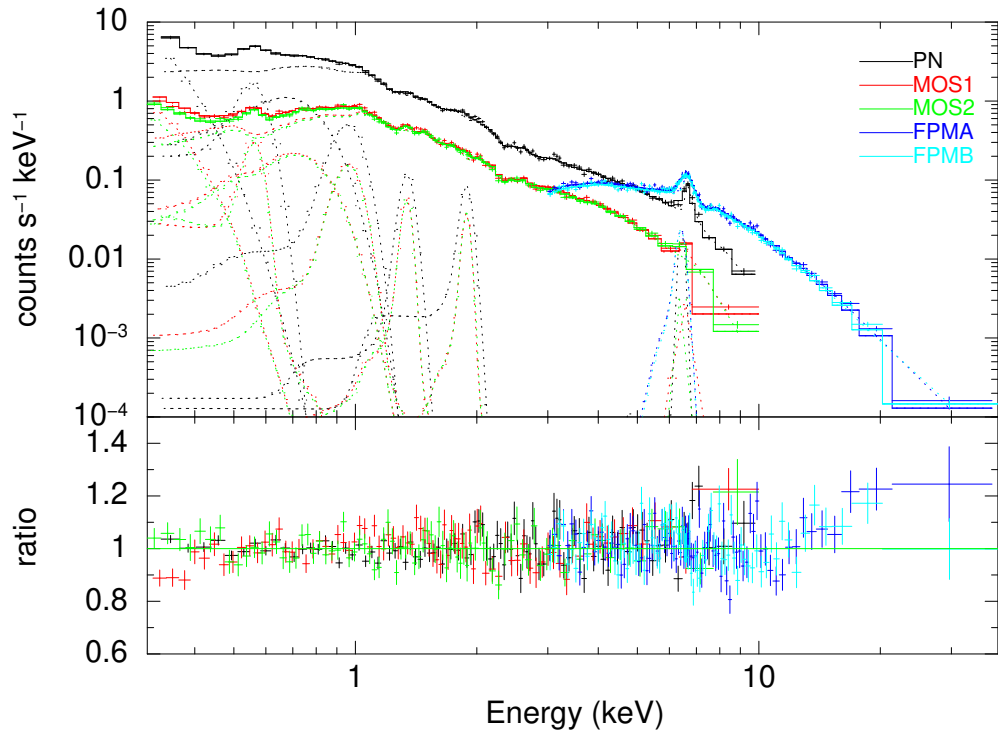
Figure 5.3: Spectrum and ratio (data/model) plot of the outburst phase joint XMM-EPIC and NuSTAR data
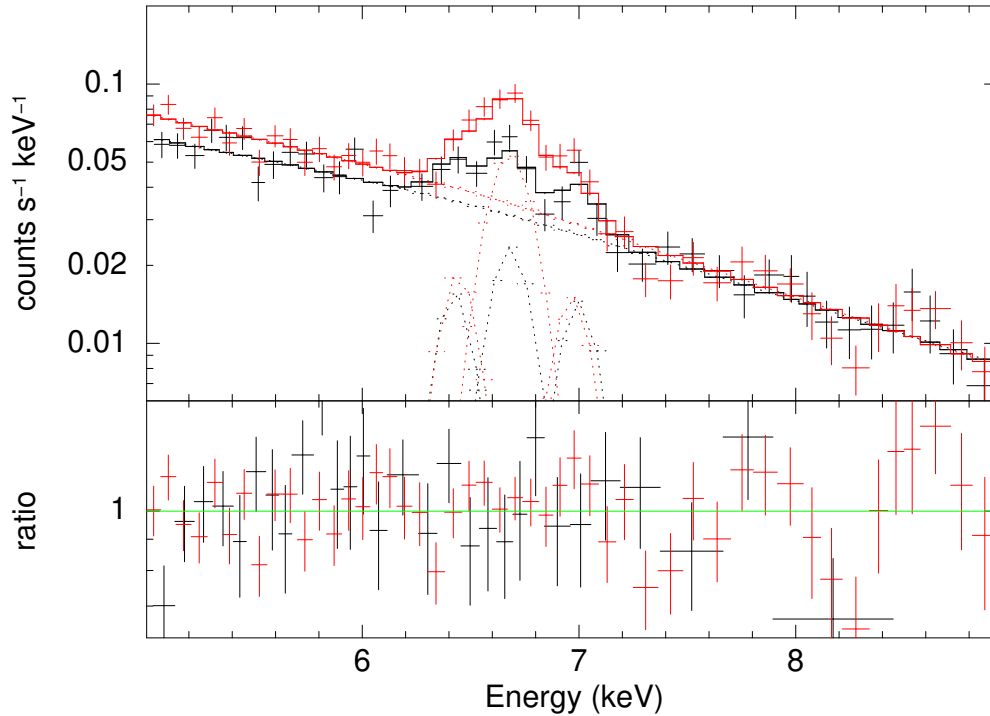
Figure 5.4: Comparison of three iron lines in quiescence and outburst phase. The spectrum and ratio (data/model) plot is shown for PN data only. Quiescence phase data is shown with black, and outburst phase data is shown in red.

the gravitational potential energy of the WD. Following the formation of a strong shock, a fraction of this kinetic energy is transformed into thermal energy, and the remaining kinetic energy gradually converts into thermal energy as the matter cools down, giving rise to the multi-temperature nature of the plasma. If we assume model Q2 during quiescence (the reason discussed in the Sec. 5.4.2), the upper temperature of the cooling flow component ($22.8^{+1.5}_{-1.1}$ keV) is related to the shock temperature of the optically thin plasma in the boundary layer (Pandel et al., 2005). By relating the thermal energy of the accreting material with the gravitational potential energy of WD and incorporating the empirical correction factor ($\alpha = T_{\text{high}}/T_{\text{s,k}}$, where T_{high} is the maximum temperature obtained from plasma emission model, $T_{\text{s,k}}$ is the Keplerian shock temperature) of 0.611 (Mukai & Byckling, 2022); we can write the following equation (Yu et al., 2018; Byckling et al., 2010):

$$KT_{high} = \alpha \times \frac{3}{16} \times \frac{GM_{\text{WD}}\mu m_{\text{P}}}{R_{\text{WD}}} \tag{5.1}$$

where K, G, μ and m_{P} represents the Boltzmann constant, gravitational constant, mean molecular weight (assumed to be 0.615) of the accreting material, and mass of proton, respectively. M_{WD} and R_{WD} denote mass and radius of WD respectively. Coupling this equation with the mass-radius relationship for WD (Nauenberg, 1972), we obtain a WD mass of $1.18^{+0.02}_{-0.01}M_{\odot}$ and a WD radius of $0.40^{+0.01}_{-0.02} \times 10^9$cm. Our measured mass value
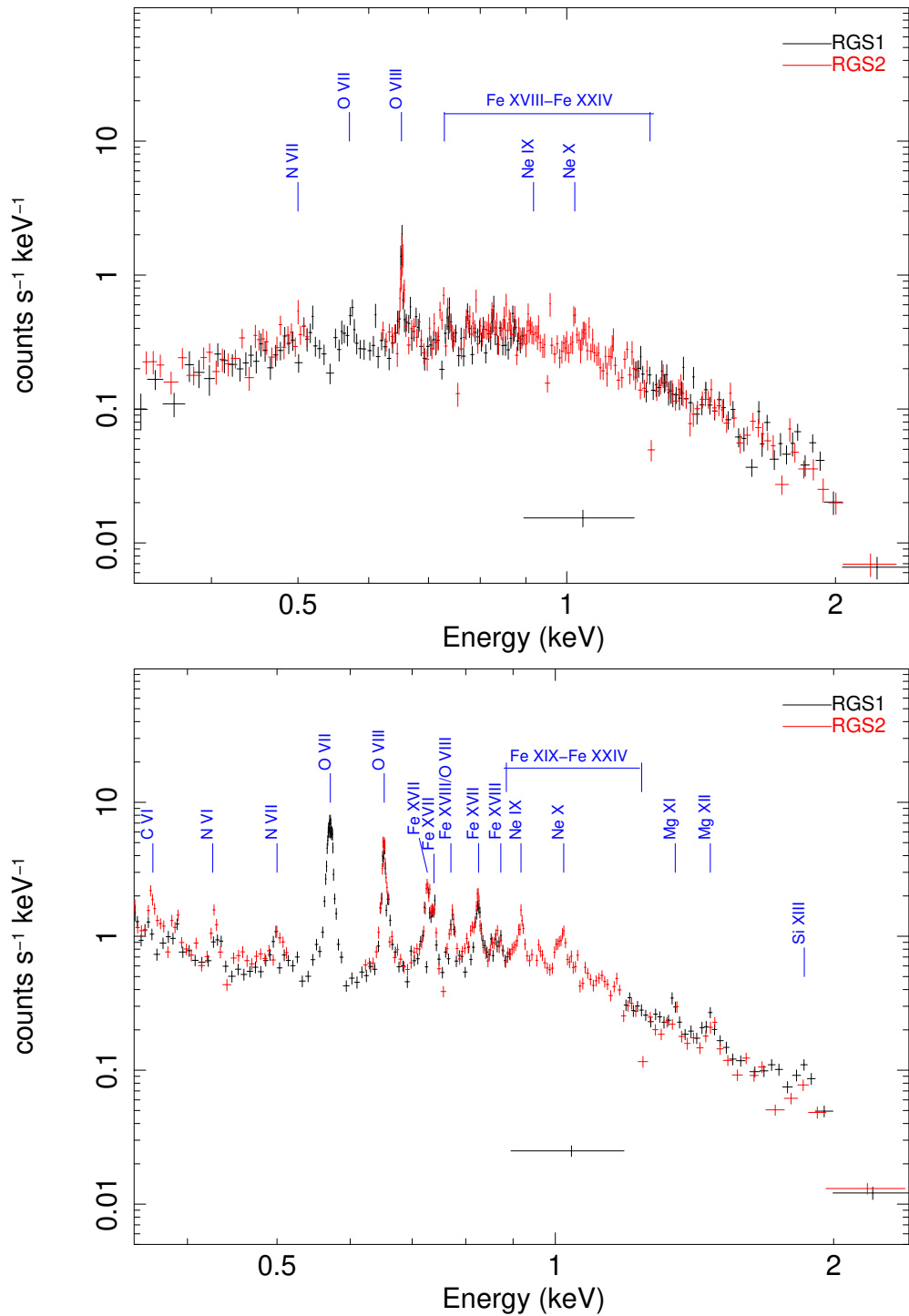
Figure 5.5: Multiple strong line emission features seen in the RGS spectra during quiescence(top) and outburst (bottom) phase.

agrees very well with the value obtained by Friend et al. (1990) ($1.19^{+0.02}_{-0.02}M_\odot$) using radial velocity study of sodium doublet line. On the other hand, the mass measurement by Bitner et al. (2007) using absorption line based optical spectroscopic study is smaller ($0.81 \pm 0.19 M_\odot$) than ours. However, we should note that the above two methods rely on the indirect way of measuring the WD mass by performing the difficult task of precise measurement of the inclination angle and mass ratio of SS Cyg. Whereas our X-ray spectroscopy method of WD mass estimate is more direct; by measuring the shock temperature obtained from broadband X-ray spectra which is directly linked to the accretion onto the WD (thereby, linked to its mass). However, we want to caution the reader that the empirical correction factor, which we have used and definitely needed, may not be universal for all DNe (Mukai & Byckling, 2022).

Our spectral model during the quiescence measures an unabsorbed bolometric flux of $5.9^{+0.1}_{-0.1} \times 10^{-11}$ erg cm^{-2} s^{-1} in 0.01-100.0 keV energy range. Considering a distance of 114.62pc to the source, this flux value corresponds to a luminosity of $\sim 9.3 \times 10^{31}$ erg s^{-1}. Now, relating the luminosity with the mass accretion rate as follows,

$$L = \frac{GM_{WD}\dot{m}}{2R_{WD}} \tag{5.2}$$

we obtain a mass accretion rate ($\dot{m}$) of $\sim 4.7 \times 10^{14}$ g s^{-1} $\sim 7.5 \times 10^{-12}$ $M_\odot$ yr^{-1}. This value is consistent with the mass accretion rate obtained from the `mkcflow` normalisation parameter after incorporating the empirical correction factor (actual mass accretion rate = empirical correction factor $\times$ cooling flow normalization; since cooling flow T_{high} is empirical factor times the actual shock temperature, therefore T_{high} gives an apparently lower M_{WD}/R_{WD} ratio, thus apparently higher mass accretion rate).

Now, for the outburst phase, broadband spectral analysis indicates an upper temperature of the optically thin plasma to be $8.4^{+0.3}_{-0.3}$ keV. This result points out the spectral softness during the outburst than quiescence. The possible origin of this hard X-ray emitting plasma is the optically thin corona instead of the boundary layer, which is optically thick during this phase. The outburst model results in an unabsorbed bolometric flux (0.01-100.0 keV) of $2.1^{+0.2}_{-0.6} \times 10^{-9}$ erg cm^{-2} s^{-1} and a corresponding luminosity of $\sim 3.3 \times 10^{33}$ erg s^{-1}. Using eqn. 5.2, we obtain $\dot{m} \sim 1.7 \times 10^{16}$ g s^{-1} $\sim 2.7 \times 10^{-10}$ $M_\odot$ yr^{-1} during the outburst. This enhanced $\dot{m}$ during outburst (~ 35 times of quiescence phase) is expected for an optically thick boundary layer (Patterson & Raymond, 1985b). We clearly notice the signs of the blackbody emission in the soft X-rays from our modelling, which is consistent with an optically thick boundary layer. The temperature of the blackbody (T_{BL}) is 28^{+1}_{-2} eV, along with an unabsorbed blackbody flux (0.01-100.0 keV) of $2.0^{+0.8}_{-0.2} \times 10^{-9}$ erg cm^{-2} s^{-1} and a corresponding luminosity (L_{BL}) of $\sim 3.2 \times 10^{33}$ erg s^{-1}. This agrees with the expectation that the increased luminosity in X-rays during outburst emits almost entirely ($\sim 97\%$) in the very soft X-rays in the form of blackbody from the optically thick BL. Following Frank et al. (2002), we can relate the blackbody luminosity

to the area of the emitting region as follows,

$$L_{\mathrm{BL}} = 4\pi R_{\mathrm{WD}} H \sigma T_{\mathrm{BL}}^4 \qquad (5.3)$$

where σ is the Stefan–Boltzmann constant, and H denotes the radial extent of the emitting region. Substituting for $L_{\mathrm{BL}}, T_{\mathrm{BL}}$ and R_{WD}, we obtain $H \sim 1.0 \times 10^6$ cm $\sim 2.6 \times 10^{-3} R_{\mathrm{WD}}$. This result shows that the optically thick BL is very close to the WD surface, which is consistent with the picture that the disk's inner edge reaches almost near the WD surface.

5.4.2   Clues from Reflection and Partial absorber: Location of X-ray emitting plasma

The Compton reflection is undoubtedly confirmed during both phases from our broadband spectral analysis. During quiescence, there is a degeneracy between the intrinsic partial absorber and the Compton reflection, which influence an overlapping energy band. Considering model Q1 involving both of those two components, we obtain a reflection amplitude of $0.40^{+0.47}_{-0.19}$.

In a simplistic geometry, the reflection from cold neutral material is ~ 1 when a point source emitter subtends a 2π solid angle over the reflector, i.e. emitter is just above the reflector. The reflection amplitude ($\Omega/2\pi$, where Ω is the solid angle subtended by the emitter on the reflector) thus can be related to the height of the emitter (h) from the reflector as (see Lopes de Oliveira & Mukai (2019)), $h/(R_{\mathrm{WD}}) = \sqrt{1/(1-(1-\Omega/2\pi)^2)} - 1$. We visualise a scenario in which the hard X-rays from optically thin BL plasma get reflected by the WD surface. Assuming a point like plasma and using the obtained value of the solid angle subtended by the optically thin BL on the surface of the WD, we calculate a height, $0.25^{+0.38}_{-0.24}$ R_{WD}, of the plasma from the WD surface. Though this quantity is very poorly constrained, the central value represents that the inner edge of the disk is quite far away from WD surface compared to the typical values obtained for other dwarf nova. For example, eclipsing dwarf nova Z Cha (Nucita et al., 2011), HT Cas (Nucita et al., 2009; Mukai et al., 1997), OY Car (Ramsay et al., 2001; Wheatley et al., 2003) shows that extent of the X-ray emission region is slightly smaller than that the WD radius or almost comparable within few per cent more than WD radius. This makes the large value of the height of the X-ray emitting boundary layer from the WD surface ($\sim 25\% R_{\mathrm{WD}}$) doubtful, which deviates from the typical picture of dwarf nova. The next concern of this scenario is that the inner edge of the disk, which is considerably far away from the WD surface, cannot be contributing to the partial absorber, especially when the binary inclination angle is relatively small $\sim 37°$. As a consequence, it becomes difficult to explain such a strong ($\sim 10^{23}$ cm^{-2}) partial absorber during the quiescence phase. Due to these ambiguities, we do not favour the scenario based on model Q1.

For the model Q2 in quiescence, the reflection amplitude is more than 1 (~ 1.25) and demands multiple sites of reflection. In this scenario, the photons emitted from the X-

ray emitting plasma will get Compton scattered by both the WD surface as well as the accretion disk.

For the outburst phase, the reflection amplitude is almost similar (~ 1.31), within statistical uncertainty, to that of the quiescence phase value and a similar reflection geometry can be envisaged. We assume a picture where the hard X-ray emitting corona is present above the optically thick BL. Since the disk's inner edge is almost near the WD surface (as supported by the calculation in Section 5.4.1), the X-rays from the emitted source can be reflected by both the WD surface and the cold accretion disk. Also, our spectral analysis showed that the outburst exhibit presence of a partial absorber (column density of $3.4^{+1.0}_{-0.9} \times 10^{22}$ cm^{-2} with a covering fraction of $0.23^{+0.02}_{-0.02}$), intrinsic to the source. During the outburst, the accretion disk remains turbulent. The partial absorber we see during this phase may originate from the outflowing accretion disk wind.

Done & Osborne (1997) found that the reflection amplitude is higher (~ 2.2) during the outburst than the quiescence (~ 0.7). They conclude that in outburst, the BL extends over the WD surface, thus providing more reflection site - WD surface as well as the inner disk. In contrast, in the quiescence phase, the inner disk is truncated or optically thin, so no reflection from the disk. But we should note that this conclusion on the value of reflection amplitudes has limitations. Their spectral analysis, based on GINGA observation, already fits a simpler continuum model with reasonably good statistics even without considering reflection.

On the other hand, Ishida et al. (2009) obtained much higher reflection amplitude in quiescence (~ 1.7) than in outburst (~ 0.9). Their explanation is quite the opposite to Done & Osborne (1997), where they describe the reflection of the emission by BL from both the accretion disk and the WD surface in quiescence. But, in the outburst, the optically thin thermal plasma is distributed as corona over an optically thick accretion disk, thereby getting reflected only from the accretion disc. But the difficulty with their measured reflection amplitudes is that either the data is not directly extended till Compton reflection hump (in outburst, using only Suzaku XIS data extended till 10 keV), or the complications due to systematic uncertainties in the HXD/PIN background level and/or cross-calibration between XIS and HXD/PIN (in quiescence, using simultaneous XIS and HXD/PIN data in 4.2-40 keV).

A recent study (Kimura et al., 2021) of anomalous outburst event of SS Cyg in 2021 using simultaneous NICER and NuSTAR data showed a weak reflection (~ 0.2) amplitude during the anomalous outburst event as well as during the quiescence phase before it. They proposed a large shock height where the hard X-ray emitting corona is expanded in the vertical direction greatly, similar to a coronal siphon flow scenario, to an extent which is more than the WD radius and resulting in a weak reflection (their Figure 10). However, it would be unusual (see the results on eclipsing dwarf novae mentioned earlier) for the inner edge of the disk to be truncated so far away from the WD radius ($\sim 10 R_{\text{WD}}$) during

quiescence, and the X-ray emitting plasma is extended till such a great distance. Note also that the maximum plasma temperature during quiescence epochs T1 and T2 derived by Kimura et al. are higher (~ 33 keV) than our value. More importantly, the Fe abundance value obtained by Kimura et al. of ~ 0.10 is significantly lower than our value (~ 0.5) or that of Ishida et al. (~ 0.37). Harrison & Hamilton (2015), using infrared spectroscopy of the secondary, also found a Fe abundace of $\sim 0.3 - 1.0 Z_\odot$, even though they noted the potential degeneracy between the secondary temperature and abundance. We note that there is correlation among the reflection amplitude, the plasma upper temperature and the Fe abundance, and thereby the measurement of reflection amplitude can be impacted by the other two parameter values. In particular, while the reflection amplitude and the maximum temperature can change from one state to another, the abundance is expected to remain constant, so it is essential to reconcile the discrepant abundance values. Finally, we note the possibility that the result of Kimura et al. potentially depends on perfect cross-calibration between NICER and NuSTAR, which may be unrealistic considering the relatively young age of the NICER mission.

At this point, our study, based on the simultaneous XMM-Newton and NuSTAR data having good cross-calibration among the instruments and extended broadband coverage, securely proves the existence of the reflection. Our measured reflection amplitudes are similar and higher than 1, indicating that both the disk and the WD surface are responsible for the reflection in both phases. We agree that there are disagreements of our results with the previous studies. Although we have our reasons to believe our modelling is correct, the disagreements should be resolved in future studies.

Now, another important feature is the neutral Fe K_α line, whose parameters agree within statistical uncertainty (see Table 5.4) in both phases. This is expected because the strength of the neutral iron is correlated with the reflection amplitude as both the fluorescence emission and the Compton reflection originate from the cold material like the WD surface or accretion disk. The Gaussian line width of the neutral line is consistent with the instrument resolution during both the quiescence and outburst phases. We should note that the actual widths of the Fe lines are limited by the instrument resolution of the EPIC detectors ($\Delta E \sim 128$ eV at 6.4 keV). Therefore, it is hard to distinguish from the EPIC data whether an actual narrow component of this line is contributed from the WD surface and a relatively broader component is contributed from the accretion disk. As a matter of fact, the disk contribution is unlikely to be resolved with EPIC data, given the possible Keplarian velocity near WD surface along the line of sight ($v_k \sin i \sim 3700$km s^{-1}, for the given WD mass and radius of SS Cyg and its binary inclination (i)) can at most produce a line width of ~ 80eV. Also, the high-resolution spectroscopic study (Rana et al., 2006) of neutral Fe line of SS Cyg in both the quiescence and outburst phase using HETG data suggest that the lines are of similar width (~ 60 eV). The relative contribution of WD surface and the disk to Compton reflection can be calculated based

on the strength of the narrow and broad components of the neutral Fe K_α line. In that regard, future observations with high-resolution instruments, e.g., XRISM, has the potential to determine this via a secure deconvolution of the neutral Fe K_α line into a narrow and broad component.

X-ray properties of asynchronous polars V1432 Aql and BY Cam

Abstract: We examined the X-ray characteristics of two asynchronous polar sources, V1432 Aql and BY Cam. For V1432 Aql, we utilized simultaneous Swift and NuSTAR observations and a separate Suzaku observation at a different time. The analysis of V1432 Aql revealed variations in the spin-folded lightcurves morphology during different epochs—displaying a double-humped pattern (NuSTAR) suggestive of two-pole accretion and a triple-humped pattern (Suzaku) indicating stream splitting. This implies a complex magnetic field structure within the white dwarf (WD). Additionally, V1432 Aql exhibited a total eclipse lasting approximately 715 ± 6 seconds, resulting from the WD's occultation by the secondary star. This provided an estimated binary inclination of approximately $73.5° - 0.5^{+0.4}$. The spectral analysis uncovered a robust and intricate intrinsic absorber, with both Suzaku and simultaneous Swift+NuSTAR observations indicating consistent strong column densities and covering fractions. This suggests inhomogeneous absorption, possibly linked to the intricate accretion stream structure. The pronounced reflection amplitude pointed to a shock height near the surface (about 2% of R_{WD}) above the pole. Additionally, soft X-rays displayed a blackbody component ($T_{BB} \sim 68eV$) arising from WD surface reprocessing at the pole. The WD's mass was determined to be $0.82^{+0.04}_{-0.04}$ M_{WD} based on the shock temperature derived from broadband spectral modelling. In the case of BY Cam, NuSTAR observations revealed a single hump-like profile throughout a spin cycle, indicating single pole accretion. A strong Compton reflection in the spectra suggested a tall shock height (around 2% of R_{WD}), similar to V1432 Aql. The WD's mass was estimated to be $0.80^{+0.03}_{-0.03} : M_{\odot}$ based on the shock temperature derived from spectral modelling. We shall incorporate the work on these two sources in a broader work of the sample study of APs

6.1   Introduction

V1432 Aql, and BY Cam are two asynchronous polars, a rare category of the mCVs with slight difference in their spin and orbital periods ($\frac{|P_o - P_s|}{P_o}$ for V1432: $\sim 0.2\%$ (Mukai et al., 2003) and for BY Cam: $\sim 0.7\%$ (Mason et al., 2022)). V1432 Aql is also an eclipsing system with an eclipse duration $\sim 700s$ and an egress and ingress duration of ($\sim 5 - 7s$) (Mukai et al., 2003). For both the systems, the spin and orbital periods are well studied in earlier photometric and X-ray observations (Littlefield et al., 2015; Mason et al., 2022; Schwarz et al., 2005). Both the systems are in the process of attaining synchronicity by gradually changing their spin period towards orbital period, and a typical time scale for V1432 Aql is $\sim 110yr$ (Pagnotta & Zurek, 2016) and BY Cam is 1200yr (Piirola et al., 1994). While V1432 Aql poses a spin period higher than the orbital period ($\sim 12150s$ vs $\sim 12116s$), BY Cam has a lower spin period than the orbital period (11963s vs $\sim 12074s$). These two systems show dominant hard X-ray spectra (Scaringi et al., 2010), generally seen in the Intermediate polars. Another interesting spectral properties for both these systems are significant blackbody emissions in very soft X-rays (V1432 Aql: Rana et al. (2005) and BY Cam: during soft state, (Ramsay & Cropper, 2002)), which is generally observed in the polars. In this work, we shall study the X-ray properties of these two exciting sources using the observations from Suzaku, Swift and NuSTAR (for V1432 Aql) and NuSTAR (for BY Cam). We shall also probe the role of complex absorption and Compton reflection in these two sources. The next section will mention the observation and data reduction methods. In Sec. 6.3, the results obtained from timing and spectral analysis of the data will be described. In Sec. 6.4, we shall interpret the results. (Wang et al., 2021) employed the same simultaneous Swift and NuSTAR data in their study. We shall also make a detailed comparison of our results with theirs.

6.2   Observations and Data reduction

6.2.1   NuSTAR

V1432 Aql was observed with NuSTAR (Harrison et al., 2013) on 2018 April 5 for $\sim 27ks$ (Obs ID: 30460004002) using its FPMA and FPMB modules, which is capable of focusing X-rays in 3-79 keV. The two focusing imaging telescope modules with very high sensitivity in hard X-rays (above 10 keV) are useful for improving the signal-to-noise ratio. We have used NuSTAR Data Analysis Software, NuSTARDAS[1] to reprocess the data. We have used a circle with a 50" radius to extract the source region and a circle with a 100" radius in a source-free region of the same detector (as of source region), out of four detectors for each telescope module, for the background region. We have generated the lightcurves in 3-79 keV and 3-10 keV, 10-30 keV and 30-55 keV bands. The phase averaged spectrum files, necessary detector response matrices, and ancillary response files have been produced

---

[1] https://heasarc.gsfc.nasa.gov/docs/nustar/analysis/

with individual spectra rebinned using GRPPHA to a minimum of 25 counts per bin to utilize χ^2 minimization for spectral fitting.

6.2.2   Swift

Swift (Gehrels et al., 2004) observed the source V1432 Aql on 2018 April 5 UTC 04:40:57, simultaneously with the NuSTAR observation, for ~ 6.7ks seconds (Obs ID: 00088611001). The X-Ray Telescope (XRT) (Burrows et al., 2005; Hill et al., 2000) of Swift, capable of focusing X-rays in the energy range 0.2-10 keV, enables us to probe the source properties in the low energy band simultaneous with NuSTAR observation. We have extracted the cleaned event files in the full energy band of XRT using `xrtpipeline` task. We have used the data in photon counting mode to select a circle with a 50" radius for the source region and a circle with a 100" radius for the background region. The spectrum has been produced using `xelect` [2] and has been regrouped using GRPPHA to a minimum of 25 counts per bin to improve chi-square minimization.

6.2.3   Suzaku

Suzaku (Mitsuda et al., 2007) observed the source V1432 Aql on 2008 April 16 UTC 21:33:07 for an exposure duration of 32ks (Obs ID: 403027010). We have used the data obtained from the X-ray Imaging Spectrometer or XIS (Koyama et al., 2007), capable of focussing X-rays in the range 0.2-10 keV. We have used the Suzaku pipeline task `aepipeline` to perform the calibration and screening of the data with default parameters and produce the cleaned event files. The source are constructed from a circular region of 180 arcsec radius around the source, and the background regions are taken from a source-free circular region of 180 arcsec. We have employed `xselect` tool to extract the lightcurves and spectra files from the source and background regions using the `GRADE == 3` cleaned event files. The instrument response files are generated using the tools `xisrmfgen` and `xissimarfgen`. We have rebinned the spectra to 25 minimum counts per bin using tool `grppha`.

6.3   Results

6.3.1   Timing Analysis:V1432 Aql

The total duration of NuSTAR lightcurve is ~ 60 ks, and that of Swift is ~ $20ks$, including the actual on-source time (for NuSTAR ~ 27ks, for Swift ~ 6.7ks) and the gaps due to earth occultation and South Atlantic Anomaly (SAA) passage. An overplot of simultaneous NuSTAR (FPMA and FPMB) lightcurves (3-55 keV), and Swift/XRT lightcurves (0.3-10.0 keV) are shown in the right panel of Figure 6.1. The very short on-source duration of Swift data makes it less competent for deriving useful timing information from the source. The Suzaku (XIS0, XIS1, XIS3) lightcurves are overplotted in the left panel of Figure 6.1, spanning ~ 72ks, covering the on-source time ~ 32 ks,

---

[2]https://heasarc.gsfc.nasa.gov/ftools/xselect/
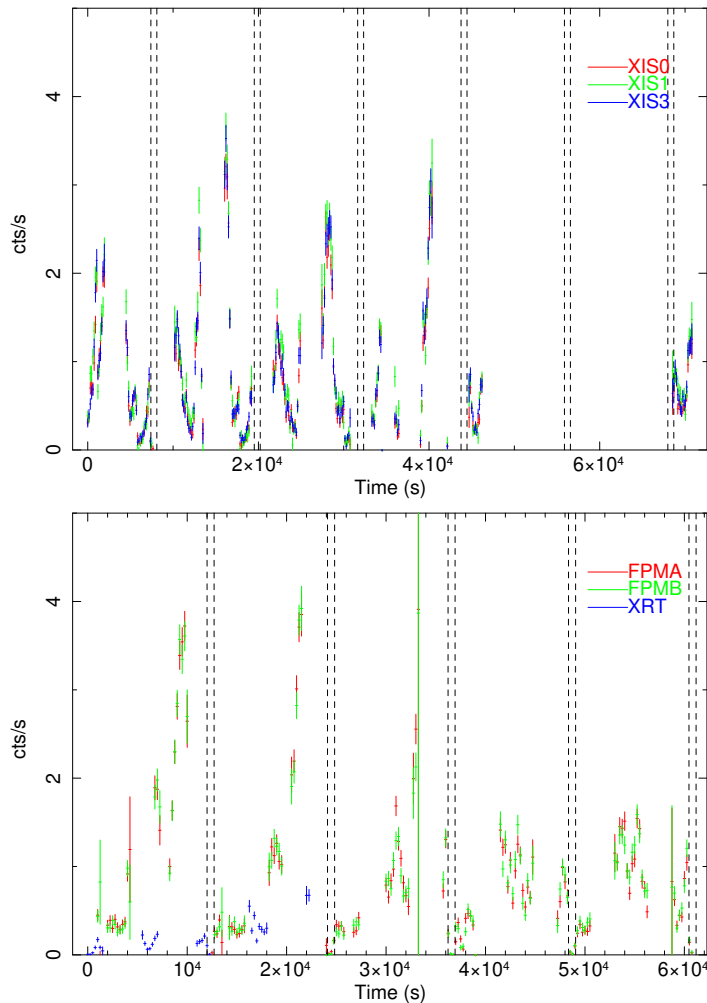
Figure 6.1: Overplot of background subtracted Suzaku/XIS lightcurves (top), and the simultaneous Swift/XIS and NuSTAR lightcurves (bottom) of V1432 Aql. The time bin size is 150s for the Suzaku lightcurves and 250s for the Swift and NuSTAR lightcurves. The marked regions denote the expected durations of eclipse

and the data gaps, as mentioned for other observatories like NuSTAR and Swift. These gaps in the lightcurves lead to difficulties in finding the exact periods of the system with high accuracy. So, we have used the spin and orbital periods and rate of change of spin periods as mentioned in Mukai et al. (2003). The NuSTAR lightcurves cover roughly three eclipses around $\sim 24, 36, 48$ks (Figure 6.1), while the other two expected eclipse locations fall partially or completely inside data gaps. All the expected eclipse locations in Suzaku lightcurves are partially or completely covered by data gaps (Figure 6.1), therefore not useful for eclipse study.

To study the eclipse properties, we have folded the NuSTAR lightcurves (see Figure 6.2) using the orbital period of (P_o) 12116.282 s, based on the mid-eclipse ephemeris $= HJD$ 2449199.693 + 0.14023475E(Mukai et al., 2003). The interesting part of the orbit folded lightcurve is the presence of the true eclipse in the binary phase, $\phi \sim 0.965\,to\,1.025$
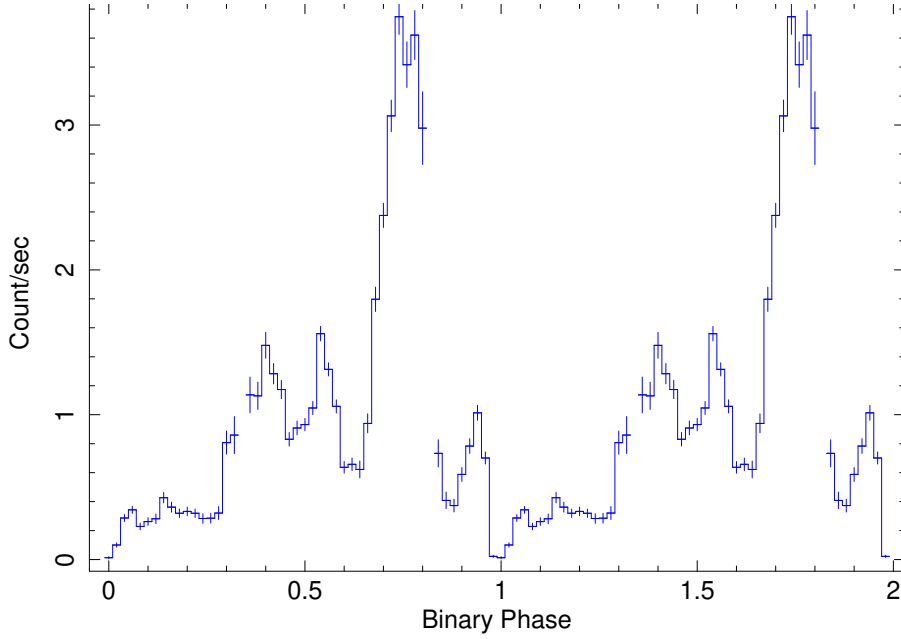
Figure 6.2: Orbit folded NuSTAR lightcurve of V1432 Aql based on orbital period of 12116.2824s in 3-55 keV. The time duration of each phase bin is ∼ 240s. The eclipse is seen around phase 0 (or 1).

when the X-ray emitting region of the WD is entirely occulted by the secondary. We have modelled the eclipse region using a piece-wise linear function in the range [0.96 to 1.027] to constrain the duration with 1σ confidence. We obtained the phase duration of the eclipse to be 0.0590 ± 0.0005 (6.3) Figure 6.3 shows the eclipsing region of the orbit folded lightcurve in 3-55 keV band. The ingress starts around phase $\phi \sim 0.96$ and the egress starts around $\phi \sim 1.025$ with the X-ray emitting region of the WD unveiling itself from behind the secondary, marking the end of the eclipse.

To Study the variation in the lightcurves over a complete rotation of the WD around its own axis, we have folded the NuSTAR and Suzaku/XIS lightcurves using the ephemeris = HJD 2449197.741 + 0.140630E − 6.5×10$^{-10}E^2$. This equates to a spin period of 12150.432 s at HJD = 2449197.741 (corresponding to the start ephemeris on UTC 1993, July 27, 05:47:02), a spin period of 12146.252 at HJD = 2454573.398 (corresponding to Suzaku observation on UTC 2008 April 16 at 21:33:07) a spin period of 12143.421 s at HJD = 2458213.702 (corresponding to the NuSTAR observation on UTC 2018, April 5, 04:51:09). We have considered the spin period change rate while folding the lightcurves. The energy-resolved spin folded lightcurves are plotted in Figure 6.4. In the spin-folded Suzaku/XIS lightcurves (left plot of Figure 6.4), we notice three broad hump-like structures, with hump profiles in phase $\Delta\phi \sim 0.15 - 0.3$ appearing incompletely, and $0.35 - 0.62, 0.8 - 1.15$. Each humps have dips in between. The hump profile in $\Delta\phi \sim 0.35 - 0.62$ appears strongest in all the energy bands (0.3-3 keV and 3-10 keV). The hardness ratio plot (HR1=$I_{3-10keV}/I_{0.3-3keV}$), showed increased hardness around phase ∼ 0.23. While an increment in HR1 is observed
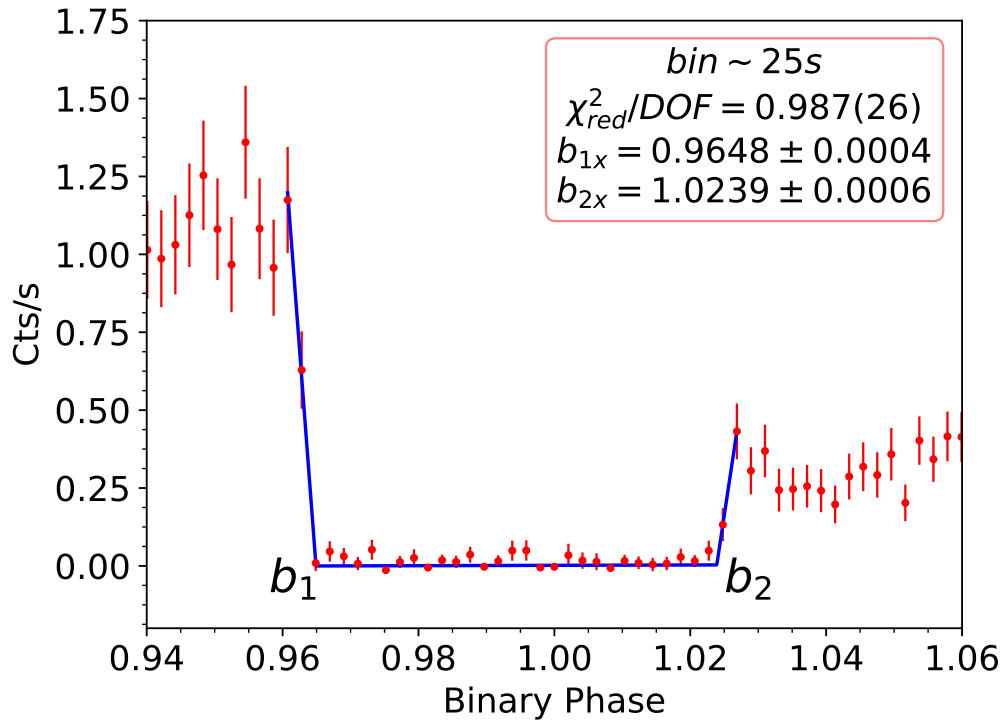
Figure 6.3: The modelling of the eclipse region of V1432 Aql with a piece-wise linear function.

during $\phi \sim 0.7$, the associated error bars are large, and spectral variability may not be significant owing to low count statistics. The spin-folded NuSTAR lightcurves (right plot of Figure 6.4) show double hump-like structures, with the strongest hump profile in $\Delta \phi \sim 0.4 - 0.6$, and the other in $\Delta \phi \sim 0 - 0.38$, with dips inside each hump. The hardness ratio (HR2=$I_{10-55 keV}/I_{3-10 keV}$) increases around $\phi \sim 0.32$.

6.3.2 Timing Analysis: BY Cam

The total duration of the NuSTAR lightcurve is ~ 60 ks, which includes the actual on-source time (for NuSTAR ~ 27ks) and earth occultation gaps and South Atlantic Anomaly (SAA) passage gaps. An overplot of simultaneous NuSTAR (FPMA and FPMB) lightcurves (3-50 keV) is shown in Figure 6.5. To study the variations on the spin period, we have followed the ephemeris, $= BJD2458827.2742 + 0.1384611E$, as determined by (Mason et al., 2022) using long duration TESS observation. The ephemeris corresponds to a spin period of 11963.039s at BJD 2458827.2742 (corresponding to UTC 2019, December 12, 18:34:50). We did not determine the spin period from NuSTAR lightcurves since the exposure time along with the data gaps of the NuSTAR lightcurves are not suitable for precisely resolving the closely spaced spin and orbital periods. Since the start time of ephemeris is close to the observation start time of NuSTAR, the spin change will be too small to affect the features of the folded lightcurves significantly. In Figure 6.6, we have plotted the spin folded lightcurves in the total 3-50 keV energy band and the 3-10
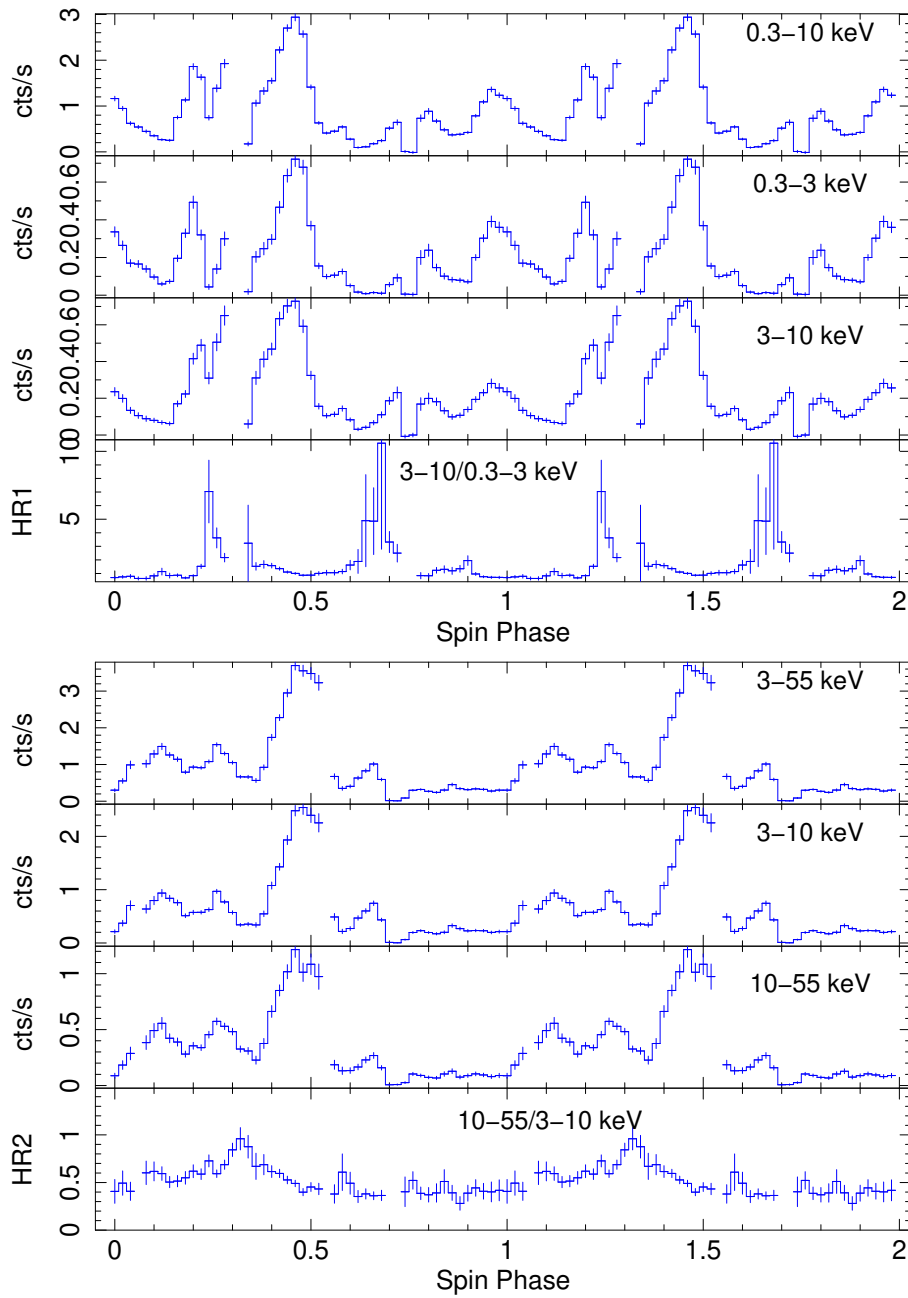
Figure 6.4: Spin folded Suzaku/XIS lightcurves of V1432 Aql in 0.3-10 keV, 0.3-3 keV and the 3-10 keV are shown in the top figure. The hardness plot between 3-10 keV and 0.3-3 keV is shown in the bottom panel. The spin-folded NuSTAR lightcurves in 3-55 keV, 3-10 keV and 10-55 keV bands are shown in the bottom figure. The hardness ratio between the 10-55 keV and 3-10 keV is shown in the bottom panel. For folding, we have mentioned the spin ephemeris in the text. The time duration of each phase bin is ~ 240s
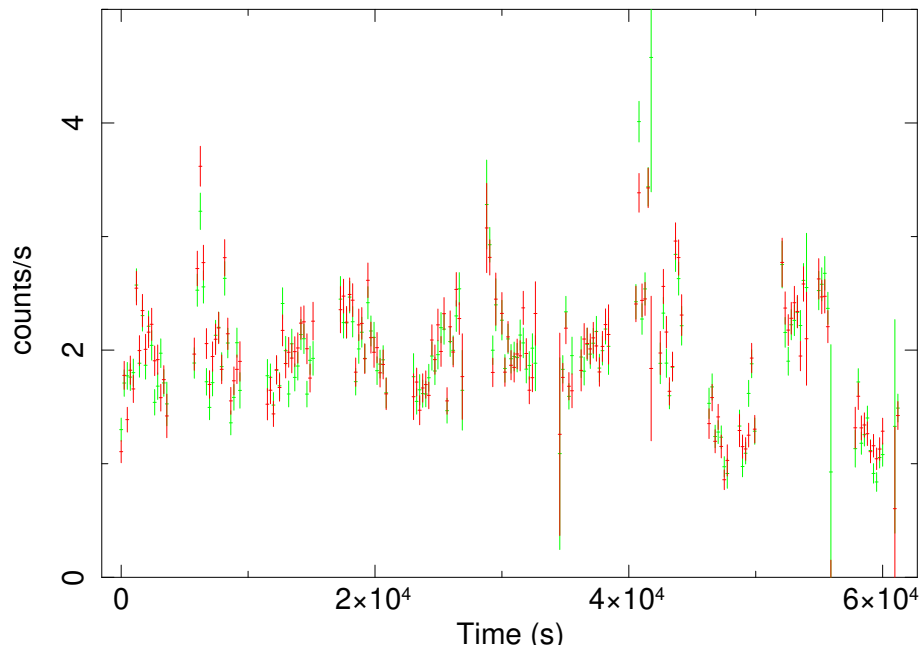
Figure 6.5: Overplot of background subtracted NuSTAR lightcurves of BY Cam. The time bin size is 250s for the NuSTAR lightcurves.

keV and 10-50 keV energy bands. The hardness ratio between 10-50 keV and 3-10 keV ($HR = 10 - 50keV/3 - 10keV$) are shown in the bottom panel of Figure 6.6. We notice the single broad hump-like structure covering the entire spin cycle in all the energy bands. Also, the hardness ratio does not show any statistically significant variation and fluctuates around a mean value of ~ 0.38. This indicates no spectral variation over a spin cycle between the 3-10 and 10-50 keV bands.

Orbit folded light curves

6.3.3 Spectral Analysis: V1432 Aql

We have used the spectral analysis package `xspec` (Arnaud, 1996) to perform the spectral analyses. The spectral models used for the analysis are part of the `xspec`. We followed the solar abundance table defined by Wilms (Wilms et al., 2000) and chose the photo-electric absorption cross-section after Verner (Verner et al., 1996).

We have first analyzed the Suzaku XIS spectra. We have simultaneously considered the XIS0 and XIS3 spectra in 0.4-10.0 keV and XIS1 spectra in 0.2-10.0 keV. We started with a simple absorbed multi-temperature plasma emission model. We gradually improved the model by including more physically expected model components to describe the spectra and to obtain a statistically significant fit. By examining the residuals from the preliminary models, we noticed the presence of blackbody component in very soft X-ray, Fe K_α line complex and a strong complex intrinsic absorber, which affects the overall spectra. The earlier literature (Rana et al., 2005) using the XMM data also showed the presence of similar components. The analysis of NuSTAR data (Wang et al., 2021) based
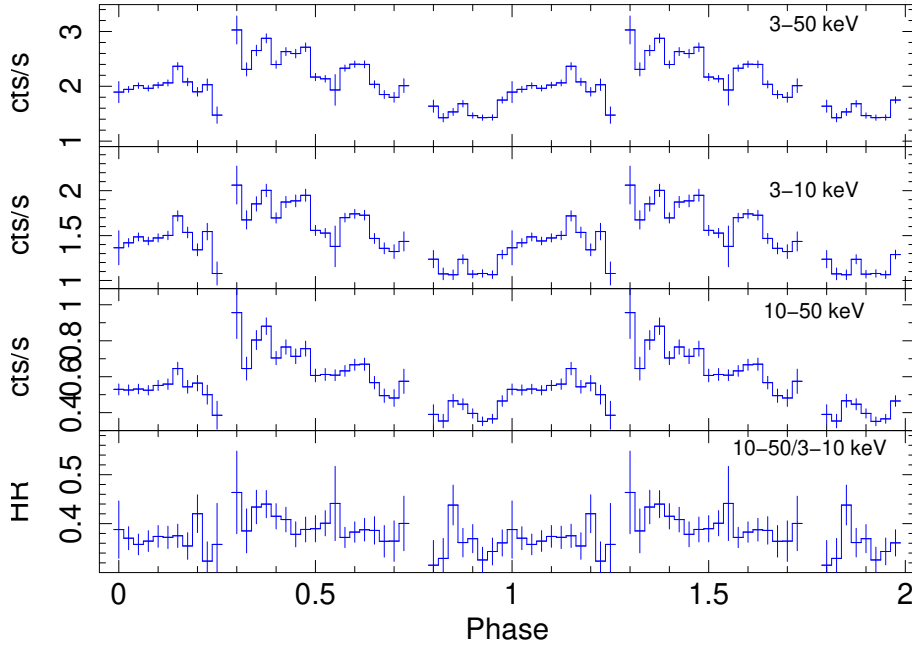
Figure 6.6: The spin-folded NuSTAR lightcurves of BY Cam in 3-50 keV, 3-10 keV and 10-50 keV band are shown in the right plot. The hardness ratio between the 10-55 keV and 3-10 keV is shown in the bottom panel. For folding, we have mentioned the spin ephemeris in the text. The time duration of each phase bin is $\sim$ 240s

on the same observation ID, which we also used (see next paragraph), showed strong Compton reflection. We fixed the reflection amplitude at 1, corresponding to a strong reflection due to a short shock height. Considering all these components, we obtained a fit statistic of χ^2(DOF)=1963(2064). The requirement of two partial covering absorption components was necessary to model the spectra (worsening of fit-statistic by $\Delta\chi^2$=200 for ΔDOF =2 if only one component was used). Though the introduction of Compton reflection is physically motivated, the statistical improvement was minimal in the Suzaku-only spectral modelling (worsening by $\Delta\chi^2$ = 7 for 1 ΔDOF). This is attributed to the absence of simultaneous coverage of hard X-ray spectra beyond 10 keV, a range crucial for detecting prominent Compton reflection. The best-fit spectral parameters are mentioned in Table 6.1, and the spectral plot is shown in Figure 6.7. The upper temperature of the plasma is $\sim$ 33.8keV, and the lower temperature is fixed at 0.0808 keV, the lowest value permissible by the model, and consistent with the temperature at the bottom of the PSR. The abundance of the plasma $0.61^{-0.13}_{+0.13}$, consistent with the value ($\sim$ 0.7) obtained by Rana et al. (2005) using XMM data. The column densities of the intrinsic absorbers are sim2.1 and 22.8, with a covering fraction of sim61% and51%, respectively. The black body component in the soft X-rays has a temperature $\sim$ 68eV. We measure a strong equivalent width of the neutral iron K_α line ($\sim$ 141eV).

Next, we proceed towards modelling the broadband simultaneous Swift/XRT and NuSTAR spectra, covering the energy range 0.3-55 keV. Beyond 55 keV, background
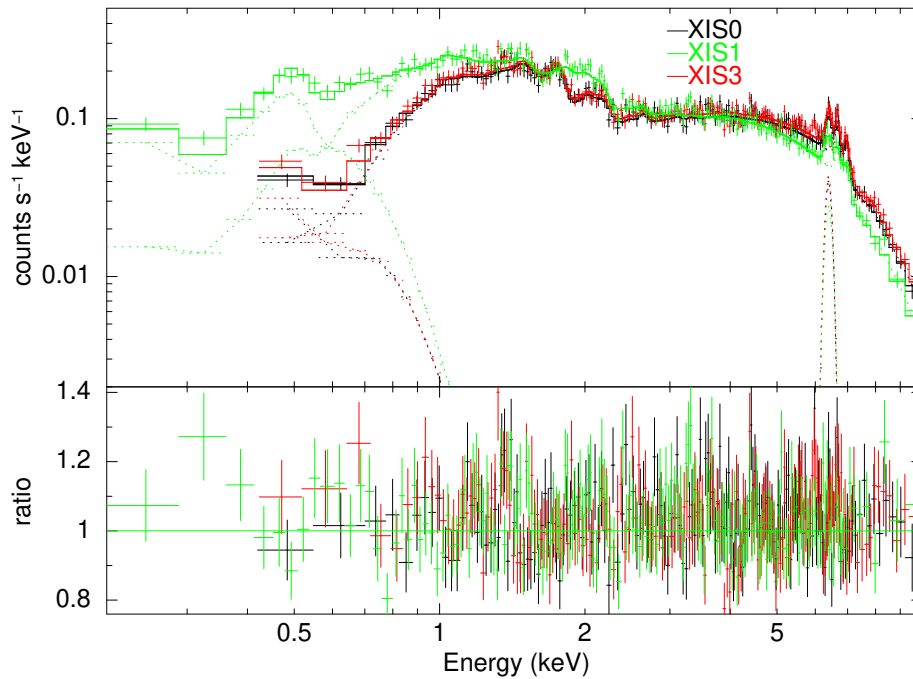
Figure 6.7: Spectrum and ratio (data/model) plot with Suzaku/XIS data of V1432 Aql. The top panel is the spectra with the best-fit final model, and the bottom panel shows the ratio.
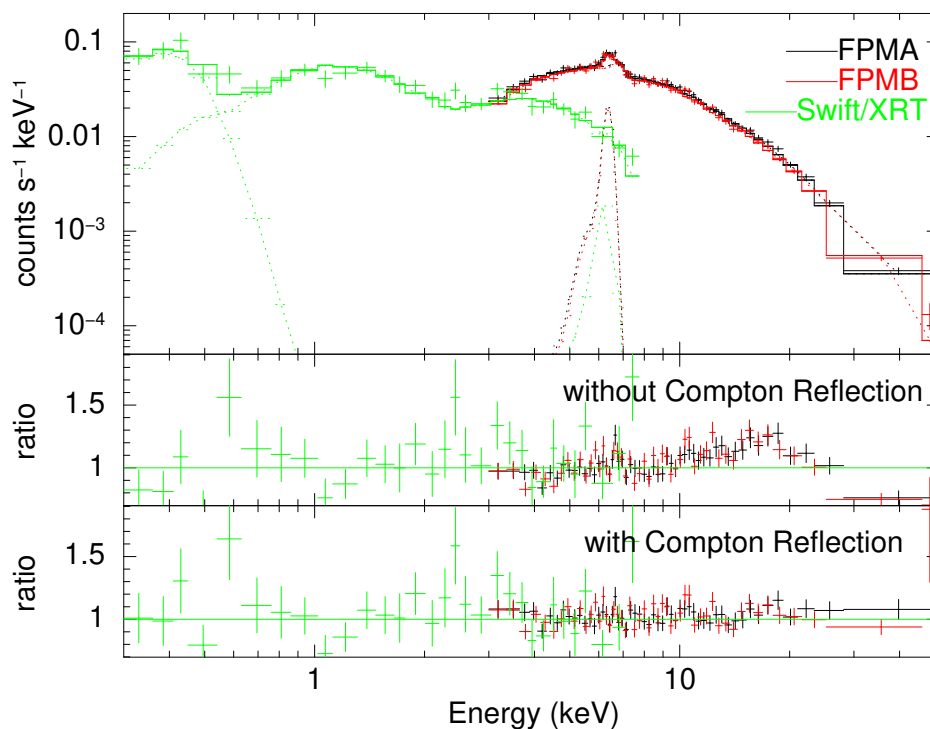
Figure 6.8: Spectrum and ratio (data/model) plot with Swift/XIS+NuSTAR data of V1432 Aql. The top panel is the spectra with the best-fit final model. The middle panel shows the ratio without the reflection component, and the bottom panel with the reflection component

spectra dominate and are not considered. While the Swift and NuSTAR coverage are simultaneous and allow us to probe the broadband X-ray range, the Swift/XRT exposure is limited and lacks the good spectral quality to properly investigate the soft to medium X-rays for complex absorption, blackbody, Fe line complex and the abundance. Guided by the analysis of Suzaku spectra, we have used similar spectral model components (`cons*tbabs*pcfabs*pcfabs*(reflect*mkcflow+bbody+gauss)`) to fit the broadband data. The plasma abundance is fixed at the Suzaku value (~ 0.61), which is also consistent with the value ($\sim 0.7 \pm 0.2$) from Rana et al. (2005), since we do not expect the abundance of the accreting material to change between Suzaku and NuSTAR epochs. We should note that the abundance obtained by Wang et al. (2021) using the same broadband data is much lower (~ 0.22), and limited exposure Swift/XRT data is unreliable for abundance determination, which can not resolve the Fe lines. Abundance is a factor which can influence the determination of the reflection amplitude. The best fit spectral parameters are mentioned in 6.1 and the spectral plot is shown in Figure 6.8. Column density of the total absorber, column densities of the complex intrinsic absorbers, covering fractions, and plasma temperature are consistent between both Suzaku and NuSTAR epochs. We have measured reflection amplitude to be $0.82^{+0.37}_{-0.29}$, which is consistent with a strong reflection, and the lower limit of the viewing angle of reflection is $< 0.67°$. The strong reflection and a strong and complex intrinsic absorber affect the spectra in an overlapping energy band (few keVs to more than 10 keVs, see Figure 8 of (Dutta & Rana, 2022b)). Therefore, better modelling of the intrinsic absorber in our fitting, along with using a consistent value of abundance, results in a physically acceptable value of reflection amplitude unlike high value (~ 4.9) of (Wang et al., 2021) which is hard to explain physically. The equivalent width of the neutral Fe K_α line is strong, with value 144^{+36}_{-26}eV. The blackbody temperature is 50^{+6}_{-7}eV. This temperature is lower than the Suzaku/XIS modelling (~ 68eV) or the value (~ 80eV) obtained by (Rana et al., 2005). It is to be noted that the blackbody component dominates in very soft X-rays; therefore, it is mostly guided by the limited exposure and low count-statistics Swift/XRT spectra in this spectral modelling. The normalisation of this component is poorly constrained (also evident from the poorly constrained blackbody flux obtained by modelling the same spectra by (Wang et al., 2021)). Therefore, we should take this low blackbody temperature of V1432 Aql, obtained in this broadband modelling, with caution, which differs from the value obtained from Suzaku or XMM modelling.

Spectral Analysis: BY Cam

We have analysed the NuSTAR spectra in 3.0-50.0 keV. The spectra are initially modelled with the absorbed multitemperature cooling flow model, with a fit statistic χ^2(DOF)=966(832). The residual shows the presence of the Compton reflection hump in 10.0-30.0 keV. After considering the Compton reflection, the fit-statistic improves to χ^2(DOF)=889(831). The best-fit parameters are quoted in the 6.2, and the spectral plot is shown in Figure 6.9. We kept the abundances linked between the plasma emission
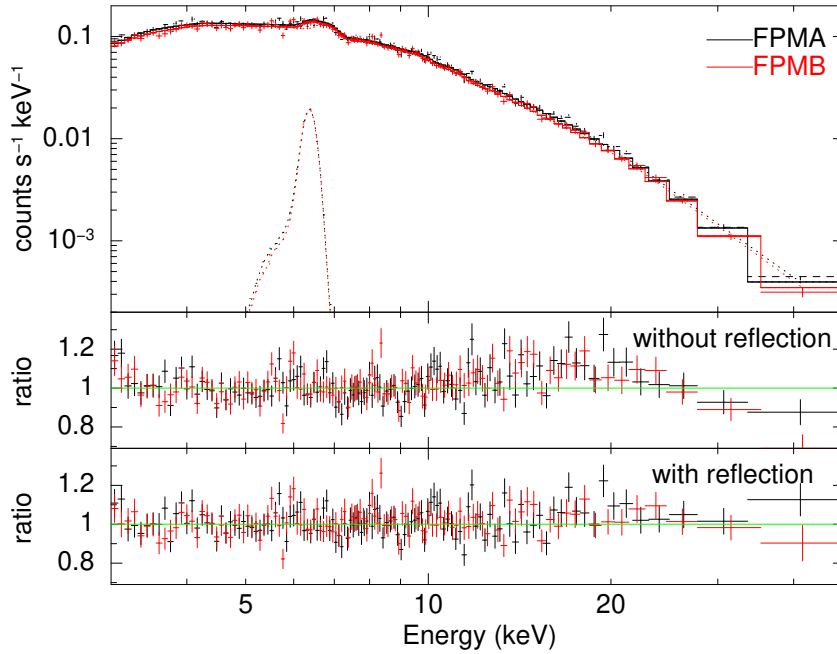
Figure 6.9: Spectrum and ratio (data/model) plot with NuSTAR data of BY Cam. The top panel is the spectra with the best-fit final model, and the bottom panel shows the ratio.

component and the reflection component, as the reflection occurs from the surface of the WD with freshly accreted material. The viewing angle of the reflection could not be constrained and, therefore, kept fixed at the default value of that parameter $cos\mu = 0.45$, corresponding to the ensemble average of the viewing angles of accreting binary systems. The reflection amplitude is large ($0.82^{+0.25}_{-0.21}$). The equivalent width of the neutral Fe line measures 68^{16}_{-20}eV. While a complex intrinsic partial photo-electric absorber is also expected for BY Cam(Done & Magdziarz, 1998), our NuSTAR spectra did not allow us to confirm it statistically. There is a lack of observation in the soft X-ray counterpart, which is simultaneous with the NuSTAR observation. However, the column density of the overall absorption is much higher, $\sim 1.51 \times 10^2 2$ cm^{-2}, compared to the ISM column density $\sim 1.56 \times 10^2 1$ cm^{-2} obtained from HI4PI survey (HI4PI Collaboration et al., 2016). This indicates the presence of extra absorption near the source.

6.4   Discussions

6.4.1   Accretion geometry of V1432 Aql

Corresponding to the binary phase difference of 0.0590 ± 0.0005 (Section 6.3.1), the eclipse duration is $715 \pm 6s$. The value ($\sim$700s) is consistent with Mukai et al. (2003), who obtained. The inclination angle (i) of the system is measured to be $73.5°$ $^{+0.4}_{-0.5}$ following the equation:

Table 6.1: Best-fit parameters from spectral modeling of V1432 Aql

Parameters	Unit	Suzaku/XIS (0.2-10.0 keV)	Swift/XRT + NuSTAR (0.3-55.0 keV)
$n_{H,tbabs}$	10^{20} cm^{-2}	$5.1^{+1.1}_{-1.0}$	$8.4^{+4.5}_{-4.0}$
T_{BB}	eV	68^{+6}_{-5}	50^{+6}_{-7}
N_{BB}	10^{-3}	$0.6^{+0.3}_{-0.1}$	$1.24^{+26.6}_{-1.15}$
$n_{H,pcf1}$	10^{22} cm^{-2}	$2.1^{0.4}_{-0.4}$	$3.4^{3.1}_{-1.9}$
%(pcf1)		$0.62^{+0.03}_{-0.03}$	$0.69^{+0.07}_{-0.15}$
$n_{H,pcf2}$	10^{22} cm^{-2}	$22.8^{+5.0}_{-3.3}$	$29.8^{+19.9}_{-11.5}$
%(pcf2)		$0.51^{+0.04}_{-0.04}$	$0.54^{+0.13}_{-0.13}$
kT$_1$	keV	0.0808_f	0.0808_f
kT$_2$	keV	$33.8^{+7.9}_{-7.1}$	$38.3^{+3.6}_{-3.4}$
N$_C$	10^{-10}	$2.1^{+0.7}_{-0.4}$	$1.6^{+0.3}_{-0.2}$
E$_l$	keV	6.40_f	6.40_f
σ	keV	0_f	0_f
eqw	eV	141^{+18}_{-18}	144^{+36}_{-26}
N$_L$	10^{-5}	$5.4^{+0.6}_{-0.6}$	$4.7^{+1.0}_{-0.9}$
Z	Z$_\odot$	$0.61^{+0.13}_{-0.13}$	0.61_f
Ω_r		1_f	$0.82^{+0.37}_{-0.29}$
i_r	deg	63.2_f	< 67
χ^2/DOF		1963(2064)	706(668)

Model in `xspec` notation is `constant*tbabs*pcfabs*pcfabs*(reflect*mkcflow+gauss+bbody)`

Table 6.2: Best-fit parameter values from NuSTAR fit (3.0-50.0 keV) of BY Cam

Parameters	Unit	Value
$n_{H,tbabs}$	10^{22} cm^{-2}	$1.51^{+0.67}_{-0.70}$
kT$_1$	keV	0.0808_f
kT$_2$	keV	$36.5^{+2.5}_{-2.2}$
N$_C$	10^{-10}	$1.09^{+0.05}_{-0.05}$
E$_l$	keV	6.40_f
σ	keV	0_f
eqw	eV	68^{+16}_{-20}
N$_L$	10^{-5}	$4.18^{+1.05}_{-1.05}$
Z	Z$_\odot$	$0.37^{+0.09}_{-0.09}$
Ω_r		$0.82^{+0.25}_{-0.21}$
χ^2/DOF		889(831)

Model in `xspec` notation is `constant*tbabs*(reflect*mkcflow+gauss)`

$$i = 90° - \sin^{-1}[\sqrt{(0.462)^2 * (\frac{q}{1+q})^{2/3} - (\frac{t_e}{P_\Omega})^2}] \qquad (6.1)$$

where q is the mass ratio of WD and secondary, t_e is the eclipse duration, P_Ω is the orbital period. The secondary is found to be of spectral class M4V (Watson et al., 1995). Correspondingly the typical mass is taken to be $0.3M_\odot$ resulting in $q = \frac{M_{sec}}{M_{WD}} = 0.36^{+0.02}_{-0.02}$ (using $M_{WD} = 0.82^{+0.04}_{-0.04}$, described in next paragraph). In Equation 6.1, we have judiciously approximated the radius of the secondary (R_2) by its Roche lobe radius, which is valid for the CVs where the secondary fills its Roche lobe and the mass transfer takes place. We have expressed R_2 in q following Paczyński (1971). The measured inclination angle verifies the highly inclined nature of the system and is consistent with values mentioned in Mukai et al. (2003).

Using the plasma upper temperature ($33.2^{+3.6}_{-3.4}$keV), representing the shock temperature, and obtained from the broadband modelling, we can calculate the mass of WD to be $0.82^{+0.04}_{-0.04}$ M_{WD} and the radius to be $6.8^{+0.3}_{-0.3} \times 10^8$cm (using Eqn 1.8, and mass-radius relationship of Nauenberg (1972)). Shaw et al. (2020) calculated the mass of the WD to be $0.76^{+0.09}_{-0.08}M_\odot$ utilizing the NuSTAR data as a part of the mass survey, which is consistent with our value. However, we believe our value provides a more accurate measurement since it measures shock temperature from broadband spectral modelling, whereas that of Shaw et al. (2020) is based on a simpler model based on only the NuSTAR data above 20 keV. Wang et al. (2021) measured a WD mass of $0.85^{+0.07}_{-0.07}$ $M_\odot$ using the same broadband Swift/XRT and NuSTAR data, and consistent with ours within statistical uncertainty. However, our value seems more accurate as our broadband spectral model is more robust in describing the complex absorption and reflection, thereby the overall continuum.

The spin folded lightcurve (Figure 6.4) of V1432 Aql shows intense and complicated variations throughout the X-ray band (soft to hard). We notice a similar pattern of double-humped structure in both the 3-10 keV and 10-55 keV bands of the NuSTAR lightcurves over the spin phase, whereas the pattern is triple-humped in the Suzaku/XIS lightcurves in both 0.3-3 keV and 3-10 keV band. The dips in each hump are possibly due to the presence of absorbing material like pre-shock flow and accretion stream. This agrees with the strong complex intrinsic absorber obtained in spectral modelling. The increase in the hardness ratios in the NuSTAR and Suzaku/XIS lightcurves denotes situations when harder X-rays can pass through the absorbing material while softer X-rays are attenuated. The dips due to the presence of dense clouds of material near the source, a variation which may be expected over the binary phase, can also appear in the spin folded lightcurves since the orbital and spin periods are very close. We have only $\sim 5 - 6$ cycles of the spin period, where the effect of orbital variations can not be averaged out. The spectral modelling of both the Suzaku and Swift+NuSTAR spectra supports the presence of a similarly strong and complex intrinsic absorber. The two partial covering absorption components indicate that the X-ray emission undergoes absorption through

highly inhomogeneous absorbing material with different column densities.

The previous studies of V1432 Aql by Staubert et al. (2003) and Rana et al. (2005) using ROSAT data showed that the accretion process can be described using the dipole accretion model. Similarly, we note the presence of a double hump-like structure in the NuSTAR lightcurves, which can be explained by the dipole accretion model.

Again the analysis of XMM and ASCA data by Rana et al. (2005) showed the presence of a triple hump profile, from which they indicated the split of double stream structure in one pole, i.e. a total of three accretion spots in the V1432 Aql system. This has also been observed by Littlefield et al. (2015) in their 28-month photometry campaign. The Suzaku/XIS observation epoch presented in our work also shows a similar kind of triple hump profile and agrees with the finding of the change in morphology of the spin-folded lightcurves during different epochs, falling in different phases of the beat period.

The broadband spectra show the presence of strong reflection for V1432 Aql. We also deduce the high equivalent width (EW) of the 6.4 keV line ($\sim$ 144 eV) for V1432 Aql. This agrees with the strong reflection from the WD surface and the strong intrinsic absorber, which can contribute to the large equivalent width of this line (Ezuka & Ishida, 1999).

For a point like reflection emission region over height h of WD surface, and covering a solid angle ω on the surface (Figure 2 of Tsujimoto et al. (2018)), the reflection amplitude $\Omega_r = \Omega/2\pi$ is given by

$$\Omega_r = \left(1 - \sqrt{1 - \frac{1}{(1+h)^2}}\right) \tag{6.2}$$

For shocks that happen just over the WD surface, a maximum solid angle (2π) is available for reflection, and a reflection amplitude of 1.0 is expected. Also, the reflection amplitude is strongest along the normal to reflecting surface and weakens with the increasing viewing angle (i_r) as a function of $\cos i_r$.

The strong reflection in V1432 Aql attests that the reflection is happening very close to the surface. Corresponding to the best-fit value of the reflection amplitude $\sim$ 0.82, the shock height will be only 2% of the R_{WD} over the WD pole.

Alternatively, based on the Aizu (1973) model, the shock height can be determined by the post-shock cooling time, i.e., the time remaining for the accreted shocked material to cool down and settle onto the WD surface. The shock height can be expressed as (Frank et al., 2002) :

$$h = \frac{1}{3} \times 9 \times 10^8 \, \dot{M}_{16}^{-1} \, f_{-2} \, M_{WD}^{3/2} \, R_9^{1/2} \, cm \tag{6.3}$$

where, $\dot{M}_{16}$ is the mass accretion rate in $10^{16} \, gm \, s^{-1}$, f_{-2} is the fractional accretion area in 10^{-2}, M_{WD} is mass of WD in terms of solar mass $M_\odot$, R_9 is the radius of WD in terms of $10^9 \, cm$. Again , accretion rate $\dot{M}$ can be determined using accretion luminosity (L_{acc})

$$L_{acc} = \frac{GM_{WD}\dot{M}}{R_{WD}} \tag{6.4}$$

where G is the universal gravitational constant. We have obtained the unabsorbed flux (F) in $0.01 - 100.0$ keV band from the broadband Swift+NuSTAR spectra to be $1.8^{+0.3}_{-0.2} \times 10^{-10}\ ergs\ cm^{-2}\ s^{-1}$. Correspondingly the accretion luminosity is $4.5^{-0.1}_{+0.1} \times 10^{33}\ ergs\ s^{-1}$ (Using $L_{acc} = 4\pi d^2 F$, where the distance to the source is 456 ± 10 pc (Gaia Collaboration et al., 2021)). Using the values of L_{acc}, M_1, R_1, we obtain $\dot{M} \sim 2.8 \times 10^{16}$ gm s$^{-1} \sim 4.4 \times 10^{-10}\,M_\odot$ yr^{-1}. Using the typical value of specific mass accretion rate ($\dot{m}$) $\sim 1\ gm\ cm^{-2}\ s^{-1}$ for V1432 Aql (Rana et al., 2005), we calculate $f \sim 0.163 \times 10^{-2}$. Now, we can compute $h \sim 1.06 \times 10^7\ cm \sim 1.6\% R_{WD}$ using the method based on the cooling time of Aizu type post-shock column. This estimate of h is harmonious to our finding from reflection amplitude that shock height is very small. We have obtained the upper limit of the spin averaged angle of reflection as ($i_r \lesssim 67°$). This value is close to the binary inclination angle of $73.5°$. This perhaps indicates that the angle between the binary axis and the spin axis of the WD is at least $73.5° - 67° = 6.5°$. Wang et al. (2021) also commented on very small shock height based on strong reflection amplitude in the NuSTAR spectra. Nevertheless, there exists a disparity in the lower limit of the angle of reflection, with their value ($\lesssim 37°$) differing from ours ($\lesssim 67°$), attributed to variations in spectral modelling approaches. We assert the reliability of our estimate as it stems from the robust characteristics of our modelling.

6.4.2   Accretion geometry of BY Cam

The energy resolved spin folded lightcurve of BY Cam in 3-50 keV, 3-10 keV, and 10-50 keV all show similar single broad hump-like structures, which indicates one pole accretion. BY Cam shows pole switching during the beat cycle, and accretion is switched from one pole to another Mason et al. (2022). The NuSTAR observation covers one such interval when one pole is actively accreting during the observation duration. The spectral modelling shows strong reflection amplitude (~ 0.82) in BY Cam like V1432 Aql, which corresponds to a shock height of 2% of the R_{WD} over the WD pole. The shock temperature (~ 36.5keV) of BY Cam is also similar to that of V1432 Aql. We estimate the WD mass to be $0.80^{+0.03}_{-0.03}\,M_\odot$ using the shock temperature obtained from the spectral modelling. The corresponding WD radius is $7^{+0.2}_{-0.2} \times 10^8$ cm. The unabsorbed bolometric flux in 0.01-100.0 keV is $1.46^{+0.03}_{-0.03} \times 10^{10}$ ergcm^{-2}s^{-1}, which corresponds to an accretion luminosity of $\sim 1.25 \times 10^{33}$ ergs^{-1} for a distance of 267pc (Gaia Collaboration et al., 2021). We calculate a mass accretion rate of $\sim 8.2 \times 10^{15}$ gms$^{-1} \sim 1.3 \times 10^{-10}\,M_\odot$yr^{-1}. This value is of the same order as that of the V1432 Aql. A future simultaneous broadband x-ray data will give us more insight into the accretion physics of BY Cam.

7

Summary & Future Prospects

In this thesis, we have examined CV sources categorised in various classes, analysing their X-ray timing and spectral characteristics to gain insights into the accretion physics within these systems. We have explored the X-ray characteristics of sources from both magnetic and non-magnetic CV categories. Within the magnetic CVs, our focus has been on a rare subcategory, namely the asynchronous polars such as CD Ind in Chapter 3, V1432 Aql and BY Cam in Chapter 6, and the intriguing intermediate polar source Paloma in Chapter 4. Regarding the non-magnetic CVs, we have delved into the quiescence and outburst properties of one of the most luminous and representative dwarf nova sources, SS Cyg, as discussed in Chapter 5. This chapter provides a summary of our findings in this section, while in Section 7.2, we outline the future prospects of our research.

7.1 Summary

- Our simultaneous broadband X-ray observation from XMM-Newton and NuSTAR of the asynchronous polar CD Ind, in chapter 3, supports a single-pole accretion model where one accretion region is active and remains visible throughout the spin phase. This fits with the existing picture of the pole-switching scenario of the source where, alternatively, two poles become active during two different phases of a beat cycle. The presence of a complex absorber is indicated in our study. The emitted X-rays pass through the inhomogeneous accretion stream, causing several narrow dips in the folded lightcurve. We also notice a significant increase in column density of the overall absorber for certain spin phase, affecting the soft X-rays below ~ 3 keV. We have also constrained the mass of the WD to be $0.87^{+0.04}_{-0.03}$ $M_\odot$. This is directly measured from the shock temperature using the extended hard X-ray data from NuSTAR, and thus an improvement from the earlier measured masses. We could not unambiguously detect the Compton reflection, which may have been small and not revealed in our spectra. We predict a possible scenario where the shock height is large. The bottom of the PSR cools down sufficiently, as supported by the presence of strong ionised oxygen K_α lines in the spectra.

- Using the simultaneous broadband X-ray observation from XMM-Newton and NuSTAR of the intermediate polar source Paloma in chapter 4, we have observed that the emission from at least one WD pole is visible at any point during the orbital cycle. The complex intrinsic absorbers play a crucial role in the system, most likely contributing from the accretion curtain/accretion stream and absorbing material

due to stream-disc/stream-magnetospheric interaction. The contribution of the complex intrinsic absorber changes significantly over a complete orbital cycle with maximum contribution during orbital phase $\phi = 0.1 - 0.22$ and minimum during phase $\phi = 0.5 - 0.8$. The X-ray power spectra show that the orbital frequency peak is much stronger than the spin frequency peak, which is not commonplace in regular intermediate polars. Strong orbital modulation possibly resulted from the presence of dense blob fixed in the orbital frame. Literature on this source showed spin modulations change significantly over the beat cycle, which is the reason behind weak power at spin frequency in the power spectra. However, from the power spectra of the source, it is difficult to conclusively argue for the presence or absence of a partial accretion disk based on the different peaks we observed. We have also estimated the WD mass to be $0.74^{+0.04}_{-0.05} M_\odot$ using the shock temperature, measured directly from the broadband spectra using multitemperature emission model for the PSR. The features in the soft X-rays can be explained with similar statistical goodness either by the extra optically thin collisionally excited cold plasma emission from PSR or by using the photoionised absorption from the warm pre-shock. To definitively favour one possibility, good quality high-resolution data are required in the soft to medium X-rays. The O-VII K_α emission line is noticed in soft X-rays. The neutral Fe K_α is weaker than ionised lines, and presumably, the neutral line strength is mostly contributed by strong intrinsic absorber. We also measured reflection amplitude but with a poor constraint and a small statistical improvement to the broadband fitting, suggesting weak reflection and tall shock height in the system.

- The spectral modelling of dwarf nova SS Cyg using simultaneous broadband X-ray observation from XMM-Newton and NuSTAR, in chapter 5, showed that the spectra were harder during quiescence (upper temperature of the plasma emission component is ~ 22.8 keV) than the outburst phase (~ 8.2 keV). the bolometric (0.01-100.0 keV) luminosity (and mass accretion rate) during outburst is ~ 35 times more than quiescence. The significant contribution to flux during outburst appears from the optically thick boundary layer in the form of blackbody emission ($T_{BL} \sim 28$ eV). During the outburst, the inner edge of the disc resides very close to the WD surface ($\sim 0.0026 R_{WD}$). Both the quiescence and outburst spectra showed similarly strong reflection amplitude, demanding both the disk and the WD surface to contribute to the reflection in both phases. The strengths of the neutral iron K_α lines are also similar between both phases. Our current data have limitations to resolve in the broad and narrow components of the line, which could potentially reveal the relative contribution of the disk and the WD surface to Compton reflection. The partial intrinsic absorber ($\sim 3 \times 10^{22}$ cm^{-2} with covering fraction ~ 0.23), possibly arising from outflowing accretion disk wind, is present during the outburst. Our modelling exhibited a delicate statistical degeneracy for quiescence between the

partial absorber and the reflection component. However, we could not physically justify the presence of the partial intrinsic absorber during this phase. The WD mass is consistent with $1.18^{+0.02}_{-0.01}\mathrm{M}_\odot$, as inferred from the X-ray broadband spectral modelling of the quiescence phase.

- We have studied the X-ray properties of two asynchronous polar sources (in chapter 6) - V1432 Aql using simultaneous Swift and NuSTAR observation and the Suzaku observation taken at a different epoch and BY Cam using the NuSTAR observation. The study on V1432 Aql showed the changes in the morphology of the spin-folded lightcurves in different epochs - double humped, indicating two-pole accretion, and triple-humped, indicating splitting of the streams. This suggests a complex magnetic field structure in the WD. The source V1432 Aql also shows a total eclipse ($\sim 715 \pm 6s$), occurring due to occultation of the WD by the secondary star, which gives us an estimate of the binary inclination to be $\sim 73.5°\ ^{+0.4}_{-0.5}$. The spectra reveal the presence of a strong and complex intrinsic absorber. Both the Suzaku observation and the simultaneous Swift+NuSTAR observation revealed similarly strong column densities and covering fractions of the absorber, indicating inhomogeneous absorption in the source, possibly arising from the complex structure of the accretion stream. The strong reflection amplitude suggests a shock height very close to the surface ($\sim 2\%$ of $\mathrm{R_{WD}}$) above the pole. The spectra also show the presence of blackbody component ($T_{BB} \sim 68\mathrm{eV}$) in soft X-rays, arising from reprocessing by the WD surface in the pole. We measure the mass of the WD to be $0.82^{+0.04}_{-0.04}\ M_{WD}$, using the shock temperature obtained from broadband spectral modelling.

  The NuSTAR observation of BY Cam unfolds a single hump-like profile over a spin cycle, indicating single pole accretion. We detected a strong Compton reflection in the source, which indicated tall shock height ($\sim 2\%$ of $\mathrm{R_{WD}}$), similar to V1432 Aql. The mass of the WD is estimated to be $0.80^{+0.03}_{-0.03}\ M_\odot$ based on the shock temperature obtained from the spectral modelling.

7.2 Future Prospects

Cataclysmic Variables constitute a diverse stellar family of accreting compact objects that are characterised by their high variability and dynamic behaviour. Exploring specific aspects, such as the intricate interactions between accreting matter and the WD magnetic field lines or the accretion disk surrounding the WD, different unique features in the optical to X-ray light curves, turbulent transport within the disc, or the ultimate fate of these objects which are not yet fully understand, requires more detailed research. Importantly, CVs are multi-wavelength laboratories of accreting compact objects, having the advantage of being nearby sources due to their dominant presence in our galaxy. This allows us to scrutinise their accretion behaviour, including the radiative processes involved in accretion, the geometrical properties of the binary system, and the physical

properties of the WD and the companion stars, using the observation in hard X-rays to radio waves. This is crucial for advancing our understanding of the nature of CVs. Based on the work done in this thesis, we plan to extend our existing works as follows:

- *Study of the asynchronous polars:* The APs are achieving synchronicity, with their spin period values slowly changing towards that of the orbital periods. While past nova eruption may be a cause of the asynchronicity in one of such system, V1500 Cyg, it can not be used as an explanation for other APs. There is another hypothesis that these systems are transitioning from IPs to polars in the scheme of the evolution of CVs from longer to shorter binary orbits. The polars are generally expected with a low mass accretion rate, small shock height, softer X-ray spectra, and blackbody emission, whereas the IPs typically have a high mass accretion rate, tall shock height, harder spectra and presence of complex structure of intrinsic absorber In our work (Dutta & Rana, 2022a) on the AP system CD Ind using broadband XMM+NuSTAR data, we noticed a hard X-ray dominated continuum, and no indication of soft blackbody component. Another important feature in the hard X-ray spectra is the presence of Compton reflection, which reveals information on geometrical properties like the shock height and viewing angle of the X-ray emitting region. Non-detection of the Compton reflection in the broadband spectra of CD Ind implied a taller shock height. These properties of CD hint at it being more IP-like. Another two AP sources, V1432 Aql and BY Cam, show hard X-ray continuum like the IPs, yet they also exhibit soft blackbody components, generally seen in polars. One key commonality in all these sources is the hard X-ray dominated spectra. Therefore, a class study of these objects is required to address the important question about APs: whether they possess some common link between IPs and polars. I shall use our proposed NuSTAR observation (*General Observer (GO) Program cycle-9*, **Proposal ID: 09201**, *PI: Anirban Dutta*), scheduled for three AP sources V1432 Aql, BY Cam and IGR J19552+0044, along with the archival X-ray data from other observatories for these three sources, to have a comparative study. Later, this study shall be extended to a few other newly discovered AP sources.

- *Study of photoionisation in Intermediate Polars:* The line emissions in soft to medium X-rays in IPs can unveil the stories of their accretion process and geometry. Mukai et al. (2003) have discussed that the line emissions from ionised plasma can follow two dominant processes - collisionally excited and photoionised. Interestingly, the photoionised spectra are found for sources that are all IPs (V1223 Sgr, AO Psc, GK Per) and have high specific mass accretion rates ($\dot{m}$, ratio of mass accretion rate to the area of the accretion region). They put the proposal that, owing to low accretion footprint (consistent with high $\dot{m}$) and short post-shock column height, a significant part of X-ray emissions pass through the pre-shock flow and photoionises the same,

leading to photoionised emission and absorption features in the spectra. A study by Islam & Mukai (2021) observed photoionisation contributes to plasma emission and absorption in the IP NY Lup and V1223 Sgr, in which they confirmed a short shock height from the broadband Chandra+NuSTAR data. However, the photoionised absorption signatures in the spectra are present for the unique IP source, Paloma, in which *tall shock height* is confirmed (Dutta & Rana, 2022b) using broadband XMM+NuSTAR data. However, a conclusive comment on the photoionzed nature of the plasma could not be made and required high-resolution spectral data from observatories like Chandra, XRISM for secure confirmation. These high-resolution spectra shall clearly resolve and measure the excess flux due to the photoionised emission of the He-like lines from medium-Z elements over the prediction of the collisionally excited emissions (coming from post-shock accretion column), and detect the photoionised O-VII edge at 0.9 keV. Secure detection of photoionisation in Paloma can help us understand the effect of shock height and the geometry of the pre-shock flow on the degree of photoionisation. The degree of photoionisation in the pre-shock flow can be measured following the available spectral models of photoionised warm absorbers (like `zxipab` after Islam & Mukai (2021)). The degree of photoionisation depends on the emitted X-ray luminosity and the solid angle subtended by the emitting shock front on the photoionised material, like pre-shock flow. Another aspect of this project will be the class study of a broader sample of IPs using archival high-resolution spectral data to measure the degree of photoionisation in the pre-shock flow. Measurement of the degree of photoionisation will serve as an important probe to decipher the geometries of the pre-shock flow, like accretion curtain or stream in front of the X-ray emitting shock-front in the IPs.

- *Study of the location of plasma in dwarf nova:* The geometry of the X-ray emitting plasma in the DNs during both quiescence and outburst phases is still an unconcluded problem. In our comparative work (Dutta et al., 2023) between the quiescence and outburst phase of the DN system SS Cyg using broadband XMM+NuSTAR data, we have suggested that X-ray emitting plasma be compact and close to the WD surface during both phases. The compact nature (<few per cent of WD radius) of the X-ray emitting plasma has been observed for a few eclipsing DN sources by analysing their timing properties of the eclipses. A schematic diagram of the expected plasma locations are shown in Figure. 7.1, where X-rays are emitted from the optically thin boundary layer during quiescence, and during the outburst, the optically thick boundary layer, along with the corona present over the inner edge of the disk, produces X-rays.

Here, we propose an exciting approach to conclusively measure the size of the X-ray emitting plasma in all typical DN systems, including SS Cyg, by performing the spectral analysis of the neutral Fe K_α line. The neutral Fe K_α line (6.4 keV)
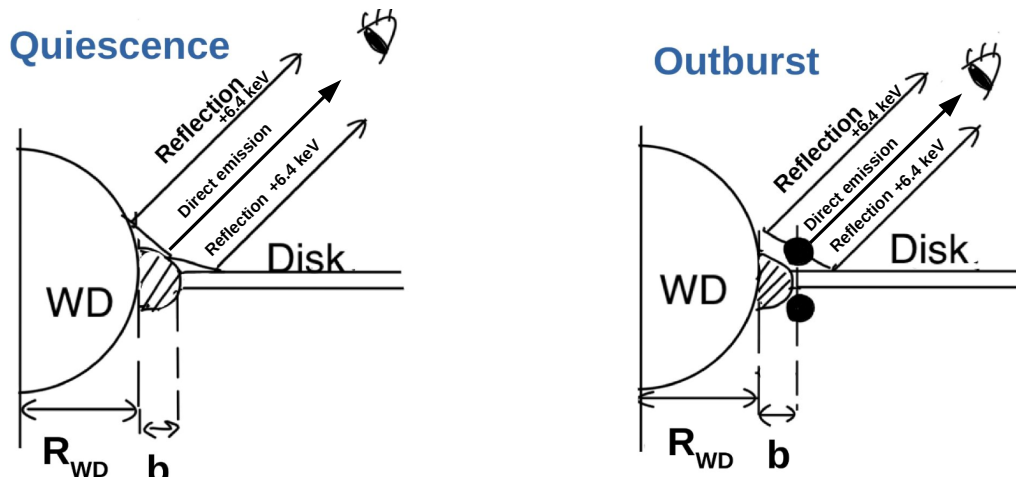
Figure 7.1: Schematic diagram of the X-ray emission from the DN source SS Cyg. The shaded regions are the boundary layers. The solid black circles represent the corona over the disk. Based on Ishida et al. (2009)

arises by reprocessing from the WD surface or inner edge of the disk has two components, a narrow component (arising from slowly rotating WD surface) and a broad component (originating from the inner edge of the disk spinning at a high Keplerian velocity). Also, the 6.4 keV line is correlated with the strength of the Compton reflection amplitude, which measures the distance of the emitter from the reflecting surface. Thus, the relative contribution of the two components of this line measures the distance of the X-ray emitting plasma from the WD surface and the disk during both the quiescence and the outburst phase. Also, during the outburst, the width of the ionised Fe K_α lines arising from the hard X-ray emitting corona formed over the inner edge of the disk measures the Keplerian velocity and thus the location of the inner edge of the disk. I shall use the archival high-resolution spectral data from Chandra for DNs and the broadband data from other observatories and propose new observations for high-resolution data from the XRISM for working on this project.

- We also plan to extend our study on CVs employing the multiwavelength observation involving optical, polarisation and UV data. These data reveal interesting properties of the companion star, the WD surface, the WD magnetic field, the accretion disk and the disk-stream interaction.

———

References

Aizu K., 1973, Progress of Theoretical Physics, 49, 1184

Araujo-Betancor S., Gänsicke B. T., Long K. S., Beuermann K., de Martino D., Sion E. M., Szkody P., 2005, ApJ, 622, 589

Arnaud K. A., 1996, in Jacoby G. H., Barnes J., eds, Astronomical Society of the Pacific Conference Series Vol. 101, Astronomical Data Analysis Software and Systems V. p. 17

Bailer-Jones C. A. L., Rybizki J., Fouesneau M., Demleitner M., Andrae R., 2021, AJ, 161, 147

Barthelmy S. D., 2004, in Flanagan K. A., Siegmund O. H. W., eds, Society of Photo-Optical Instrumentation Engineers (SPIE) Conference Series Vol. 5165, X-Ray and Gamma-Ray Instrumentation for Astronomy XIII. pp 175–189, doi:10.1117/12.506779

Baskill D. S., Wheatley P. J., Osborne J. P., 2005, MNRAS, 357, 626

Bitner M. A., Robinson E. L., Behr B. B., 2007, ApJ, 662, 564

Bode M. F., et al., 2006, ApJ, 652, 629

Burrows D. N., et al., 2005, Space Sci. Rev., 120, 165

Byckling K., Mukai K., Thorstensen J. R., Osborne J. P., 2010, MNRAS, 408, 2298

Cash W., 1979, ApJ, 228, 939

Chomiuk L., et al., 2014, ApJ, 788, 130

Chomiuk L., Metzger B. D., Shen K. J., 2021, ARA&A, 59, 391

Clark D. H., Stephenson F. R., 1977, The historical supernovae

Cooley J. W., Tukey J. W., 1965, Mathematics of computation, 19, 297

Córdova F. A. D., 1995, in X-ray Binaries. pp 331–389

Cordova F. A., Mason K. O., 1983, in Lewin W. H. G., van den Heuvel E. P. J., eds, Accretion-Driven Stellar X-ray Sources. pp 147–187

Craig N., Howell S. B., Sirk M. M., Malina R. F., 1996, ApJ, 457, L91

Cropper M., 1990, Space Sci. Rev., 54, 195

Currie M. J., Berry D. S., Jenness T., Gibb A. G., Bell G. S., Draper P. W., 2014, in Manset N., Forshay P., eds, Astronomical Society of the Pacific Conference Series Vol. 485, Astronomical Data Analysis Software and Systems XXIII. p. 391

Done C., Magdziarz P., 1998, MNRAS, 298, 737

Done C., Osborne J. P., 1997, MNRAS, 288, 649

Dutta A., Rana V., 2022a, MNRAS, 511, 4981

Dutta A., Rana V., 2022b, ApJ, 940, 100

Dutta A., Rana V., Mukai K., de Oliveira R. L., 2023, ApJ, 957, 33

Ezuka H., Ishida M., 1999, ApJS, 120, 277

Forman W., Jones C., Cominsky L., Julien P., Murray S., Peters G., Tananbaum H., Giacconi R., 1978, ApJS, 38, 357

Frank J., King A., Raine D. J., 2002, Accretion Power in Astrophysics: Third Edition

Friend M. T., Martin J. S., Smith R. C., Jones D. H. P., 1990, MNRAS, 246, 654

Gabriel C., et al., 2004, in Ochsenbein F., Allen M. G., Egret D., eds, Astronomical Society of the Pacific Conference Series Vol. 314, Astronomical Data Analysis Software and Systems (ADASS) XIII. p. 759

Gaia Collaboration et al., 2018, A&A, 616, A1

Gaia Collaboration et al., 2021, A&A, 649, A1

Gehrels N., Williams E. D., 1993, ApJ, 418, L25

Gehrels N., et al., 2004, ApJ, 611, 1005

Gendreau K. C., et al., 2016, in den Herder J.-W. A., Takahashi T., Bautz M., eds, Society of Photo-Optical Instrumentation Engineers (SPIE) Conference Series Vol. 9905, Space Telescopes and Instrumentation 2016: Ultraviolet to Gamma Ray. p. 99051H, doi:10.1117/12.2231304

George I. M., Fabian A. C., 1991, MNRAS, 249, 352

Gordon A. C., Aydi E., Page K. L., Li K.-L., Chomiuk L., Sokolovsky K. V., Mukai K., Seitz J., 2021, ApJ, 910, 134

HI4PI Collaboration et al., 2016, A&A, 594, A116

Hakala P., Ramsay G., Potter S. B., Beardmore A., Buckley D. A. H., Wynn G., 2019, MNRAS, 486, 2549

Harrison T. E., Campbell R. K., 2016, MNRAS, 459, 4161

Harrison T. E., Hamilton R. T., 2015, AJ, 150, 142

Harrison F. A., et al., 2013, ApJ, 770, 103

Hellier C., 1993, MNRAS, 265, L35

Hellier C., 2001, Cataclysmic Variable Stars

Henze M., Ness J. U., Darnley M. J., Bode M. F., Williams S. C., Shafter A. W., Kato M., Hachisu I., 2014, A&A, 563, L8

Hessman F. V., Robinson E. L., Nather R. E., Zhang E. H., 1984, ApJ, 286, 747

Hill J. E., Zugger M. E., Shoemaker J., Witherite M. E., Koch T. S., Chou L. L., Case T., Burrows D. N., 2000, in Flanagan K. A., Siegmund O. H., eds, Society of Photo-Optical Instrumentation Engineers (SPIE) Conference Series Vol. 4140, X-Ray and Gamma-Ray Instrumentation for Astronomy XI. pp 87–98, doi:10.1117/12.409162

Hind J. R., 1848, MNRAS, 8, 146

Honda M., et al., 1975, IAU Circ., 2826, 1

Ishida M., Okada S., Hayashi T., Nakamura R., Terada Y., Mukai K., Hamaguchi K., 2009, PASJ, 61, S77

Islam N., Mukai K., 2021, ApJ, 919, 90

Jansen F., et al., 2001, A&A, 365, L1

Jones M. H., Watson M. G., 1992, MNRAS, 257, 633

Joshi A., Pandey J. C., 2019, Bulletin de la Societe Royale des Sciences de Liege, 88, 240

Joshi A., Pandey J. C., Singh K. P., Agrawal P. C., 2016, ApJ, 830, 56

Joye W. A., Mandel E., 2003, in Payne H. E., Jedrzejewski R. I., Hook R. N., eds, Astronomical Society of the Pacific Conference Series Vol. 295, Astronomical Data Analysis Software and Systems XII. p. 489

Kelley R. L., et al., 2007, PASJ, 59, 77

Kimura M., et al., 2021, PASJ, 73, 1262

King A. R., Shaviv G., 1984, MNRAS, 211, 883

Knigge C., Baraffe I., Patterson J., 2011, ApJS, 194, 28

Koyama K., et al., 2007, PASJ, 59, 23

Kraft R. P., Mathews J., Greenstein J. L., 1962, ApJ, 136, 312

Krautter J., 2008, in Evans A., Bode M. F., O'Brien T. J., Darnley M. J., eds, Astronomical Society of the Pacific Conference Series Vol. 401, RS Ophiuchi (2006) and the Recurrent Nova Phenomenon. p. 139

Kuijpers J., Pringle J. E., 1982, A&A, 114, L4

Lamb D. Q., Masters A. R., 1979, ApJ, 234, L117

Littlefield C., et al., 2015, MNRAS, 449, 3107

Littlefield C., Garnavich P., Mukai K., Mason P. A., Szkody P., Kennedy M., Myers G., Schwarz R., 2019, ApJ, 881, 141

Littlefield C., et al., 2022, arXiv e-prints, p. arXiv:2205.02863

Lomb N. R., 1976, Ap&SS, 39, 447

Lopes de Oliveira R., Mukai K., 2019, ApJ, 880, 128

Magdziarz P., Zdziarski A. A., 1995, MNRAS, 273, 837

Mason K. O., et al., 2001, A&A, 365, L36

Mason P. A., et al., 2020, Advances in Space Research, 66, 1123

Mason P. A., et al., 2022, ApJ, 938, 142

Matt G., Perola G. C., Piro L., 1991, A&A, 247, 25

Mauche C. W., 2004, ApJ, 610, 422

Mauche C. W., Raymond J. C., Cordova F. A., 1988, ApJ, 335, 829

McGowan K. E., Priedhorsky W. C., Trudolyubov S. P., 2004, ApJ, 601, 1100

Miller-Jones J. C. A., Sivakoff G. R., Knigge C., Körding E. G., Templeton M., Waagen E. O., 2013, Science, 340, 950

Mitsuda K., et al., 2007, PASJ, 59, S1

Mukai K., 2017, PASP, 129, 062001

Mukai K., Byckling K., 2022, Research Notes of the American Astronomical Society, 6, 65

Mukai K., Ishida M., 2001, ApJ, 551, 1024

Mukai K., Ishida M., Osborne J. P., 1994, PASJ, 46, L87

Mukai K., Wood J. H., Naylor T., Schlegel E. M., Swank J. H., 1997, ApJ, 475, 812

Mukai K., Kinkhabwala A., Peterson J. R., Kahn S. M., Paerels F., 2003, ApJ, 586, L77

Mukai K., Orio M., Della Valle M., 2008, ApJ, 677, 1248

Mukai K., Rana V., Bernardini F., de Martino D., 2015, ApJ, 807, L30

Mushotzky R. F., Szymkowiak A. E., 1988, in Fabian A. C., ed., NATO Advanced Science Institutes (ASI) Series C Vol. 229, NATO Advanced Science Institutes (ASI) Series C. p. 53, doi:10.1007/978-94-009-2953-1_6

Myers G., et al., 2017, PASP, 129, 044204

Narayan R., Popham R., 1993, Nature, 362, 820

Nasa High Energy Astrophysics Science Archive Research Center (Heasarc) 2014, HEAsoft: Unified Release of FTOOLS and XANADU, Astrophysics Source Code Library, record ascl:1408.004 (ascl:1408.004)

Nauenberg M., 1972, ApJ, 175, 417

Norton A. J., Watson M. G., King A. R., Lehto H. J., McHardy I. M., 1992, MNRAS, 254, 705

Norton A. J., Beardmore A. P., Taylor P., 1996, MNRAS, 280, 937

Norton A. J., Hellier C., Beardmore A. P., Wheatley P. J., Osborne J. P., Taylor P., 1997, MNRAS, 289, 362

Norton A. J., Wynn G. A., Somerscales R. V., 2004, ApJ, 614, 349

Nucita A. A., Maiolo B. M. T., Carpano S., Belanger G., Coia D., Guainazzi M., de Paolis F., Ingrosso G., 2009, A&A, 504, 973

Nucita A. A., Kuulkers E., Maiolo B. M. T., de Paolis F., Ingrosso G., Vetrugno D., 2011, A&A, 536, A75

Okada S., Nakamura R., Ishida M., 2008, ApJ, 680, 695

Osaki Y., 1974, PASJ, 26, 429

Paczyński B., 1971, ARA&A, 9, 183

Page K. L., et al., 2015, MNRAS, 454, 3108

Page K. L., et al., 2022, MNRAS, 514, 1557

Pagnotta A., Zurek D., 2016, MNRAS, 458, 1833

Pandel D., Córdova F. A., Mason K. O., Priedhorsky W. C., 2005, ApJ, 626, 396

Parker T. L., Norton A. J., Mukai K., 2005, A&A, 439, 213

Patterson J., Raymond J. C., 1985a, ApJ, 292, 535

Patterson J., Raymond J. C., 1985b, ApJ, 292, 550

Piirola V., Coyne G. V., Takalo S. J., Takalo L., Larsson S., Vilhu O., 1994, A&A, 283, 163

Popham R., Narayan R., 1995, ApJ, 442, 337

Press W. H., Rybicki G. B., 1989, ApJ, 338, 277

Prialnik D., Kovetz A., 1995, ApJ, 445, 789

Pringle J. E., Savonije G. J., 1979, MNRAS, 187, 777

Ramsay G., Cropper M., 2002, MNRAS, 334, 805

Ramsay G., Buckley D. A. H., Cropper M., Harrop-Allin M. K., 1999, MNRAS, 303, 96

Ramsay G., Potter S., Cropper M., Buckley D. A. H., Harrop-Allin M. K., 2000, MNRAS, 316, 225

Ramsay G., et al., 2001, A&A, 365, L288

Rana V. R., Singh K. P., Schlegel E. M., Barrett P., 2004, AJ, 127, 489

Rana V. R., Singh K. P., Barrett P. E., Buckley D. A. H., 2005, ApJ, 625, 351

Rana V. R., Singh K. P., Schlegel E. M., Barrett P. E., 2006, ApJ, 642, 1042

Rappaport S., Cash W., Doxsey R., McClintock J., Moore G., 1974, ApJ, 187, L5

Rawat N., Pandey J. C., Joshi A., Scaringi S., Yadava U., 2022, MNRAS, 517, 1667

Ricketts M. J., King A. R., Raine D. J., 1979, MNRAS, 186, 233

Roberts D. H., Lehar J., Dreher J. W., 1987, AJ, 93, 968

Roming P. W. A., et al., 2005, Space Sci. Rev., 120, 95

Scargle J. D., 1982, ApJ, 263, 835

Scaringi S., et al., 2010, MNRAS, 401, 2207

Schmidt G. D., Liebert J., Stockman H. S., 1995, ApJ, 441, 414

Schwarz R., Schwope A. D., Staude A., Remillard R. A., 2005, A&A, 444, 213

Schwarz R., Schwope A. D., Staude A., Rau A., Hasinger G., Urrutia T., Motch C., 2007, A&A, 473, 511

Schwope A. D., Buckley D. A. H., O'Donoghue D., Hasinger G., Truemper J., Voges W., 1997, A&A, 326, 195

Serlemitsos P. J., et al., 2007, PASJ, 59, S9

Seward F. D., Charles P. A., 2010, Exploring the X-ray Universe

Shafter A. W., 1983, PhD thesis, California Univ., Los Angeles.

Shafter A. W., 2017, ApJ, 834, 196

Shakura N. I., Sunyaev R. A., 1973, A&A, 24, 337

Shaw A. W., et al., 2020, MNRAS, 498, 3457

Singh K. P., et al., 2014, in Takahashi T., den Herder J.-W. A., Bautz M., eds, Society of Photo-Optical Instrumentation Engineers (SPIE) Conference Series Vol. 9144, Space Telescopes and Instrumentation 2014: Ultraviolet to Gamma Ray. p. 91441S, doi:10.1117/12.2062667

Sobolev A. V., Zhilkin A. G., Bisikalo D. V., Buckley D. A. H., 2021, Astronomy Reports, 65, 392

Sokoloski J. L., Luna G. J. M., Mukai K., Kenyon S. J., 2006, Nature, 442, 276

Sokolovsky K. V., et al., 2022, MNRAS, 514, 2239

Starrfield S., Truran J. W., Sparks W. M., Kutter G. S., 1972, ApJ, 176, 169

Staubert R., Friedrich S., Pottschmidt K., Benlloch S., Schuh S. L., Kroll P., Splittgerber E., Rothschild R., 2003, A&A, 407, 987

Stockman H. S., Schmidt G. D., Lamb D. Q., 1988, ApJ, 332, 282

Strüder L., et al., 2001, A&A, 365, L18

Takahashi T., et al., 2007, PASJ, 59, 35

Thorstensen J. R., Ringwald F. A., Taylor C. J., Sheets H. A., Peters C. S., Skinner J. N., Alper E. H., Weil K. E., 2017, Research Notes of the American Astronomical Society, 1, 29

Tsujimoto M., Morihana K., Hayashi T., Kitaguchi T., 2018, PASJ, 70, 109

Turner M. J. L., et al., 2001, A&A, 365, L27

Vennes S., Wickramasinghe D. T., Thorstensen J. R., Christian D. J., Bessell M. S., 1996, AJ, 112, 2254

Verbunt F., Bunk W. H., Ritter H., Pfeffermann E., 1997, A&A, 327, 602

Verner D. A., Ferland G. J., Korista K. T., Yakovlev D. G., 1996, ApJ, 465, 487

Wang Q., Qian S., Zhu L., 2021, arXiv e-prints, p. arXiv:2110.13483

Warner B., 1976, The Observatory, 96, 49

Warner B., 1995, Cataclysmic variable stars. Vol. 28

Warner B., 2002, in Hernanz M., José J., eds, American Institute of Physics Conference Series Vol. 637, Classical Nova Explosions. pp 3–15 (arXiv:astro-ph/0206452), doi:10.1063/1.1518170

Watson M. G., et al., 1995, MNRAS, 273, 681

Webbink R. F., Wickramasinghe D. T., 2002, MNRAS, 335, 1

Weisskopf M. C., Brinkman B., Canizares C., Garmire G., Murray S., Van Speybroeck L. P., 2002, PASP, 114, 1

Wheatley P. J., Mauche C. W., 2005, in Hameury J. M., Lasota J. P., eds, Astronomical Society of the Pacific Conference Series Vol. 330, The Astrophysics of Cataclysmic Variables and Related Objects. p. 257 (arXiv:astro-ph/0412166), doi:10.48550/arXiv.astro-ph/0412166

Wheatley P. J., Mauche C. W., Mattei J. A., 2003, MNRAS, 345, 49

Wilms J., Allen A., McCray R., 2000, ApJ, 542, 914

Wynn G. A., King A. R., 1992, MNRAS, 255, 83

Yu Z.-l., Xu X.-j., Li X.-D., Bao T., Li Y.-x., Xing Y.-c., Shen Y.-f., 2018, ApJ, 853, 182

de Martino D., Bernardini F., Mukai K., Falanga M., Masetti N., 2020, Advances in Space Research, 66, 1209

den Herder J. W., et al., 2001, A&A, 365, L7

van Teeseling A., Kaastra J. S., Heise J., 1996, A&A, 312, 186